WRAD core perturbation impairs DNA replication fidelity promoting immunoediting in pancreatic cancer

Francesca Citron[1,20], I-Lin Ho[1], Chiara Balestrieri[2,3], Zhaoliang Liu[1], Er-Yen Yen[1,4], Luca Cecchetto[1], Luigi Perelli[1,5], Li Zhang[1,5], Luis Castillo Montanez[6], Nicholas Blazanin[1,7], Charles A. Dyke[1], Rutvi Shah[1,4], Sergio Attanasio[1], Sanjana Srinivasan[8], Ko-Chien Chen[9], Ziheng Chen[1], Iolanda Scognamiglio[1], Nhung Pham[1], Hania Khan[1,5], Shan Jiang[1,8], Jing Pan[6], Ben Vanderkruk[10,11,12], Cecilia S. Leung[1], Mahinur Mattohti[1,13], Kunal Rai[1], Yanshuo Chu[1], Linghua Wang[1], Sisi Gao[1,8], Angela K. Deem[1,8], Alessandro Carugo[8,14], Huamin Wang[15], Wantong Yao[16], Giovanni Tonon[2,17], Yun Xiong[18], Philip L. Lorenzi[18], Chiara Bonini[3,17], M. Anna Zal[19], Brad G. Hoffman[10,11], Tim Heffernan[8], Virginia Giuliani[8], Collene R. Jeter[19], Yonathan Lissanu[1,7], Giannicola Genovese[1,2], Mauro Di Pilato[6], Andrea Viale[1,20], Giulio F. Draetta[1,20].

Affiliations:

[1] Department of Genomic Medicine, The University of Texas MD Anderson Cancer Center, Houston, TX 77030, USA.

[2] Center for Omics Sciences, IRCCS San Raffaele Scientific Institute, Milan 20132, Italy.

[3] Experimental Hematology Unit, IRCCS San Raffaele Scientific Institute, Milan 20132, Italy.

[4] MD Anderson UTHealth Graduate School of Biomedical Sciences, Houston, TX 77030, USA.

[5] Department of Genitourinary Oncology, The University of Texas MD Anderson Cancer Center, Houston, TX 77030, USA.

[6] Department of Immunology, The University of Texas MD Anderson Cancer Center, Houston, TX 77030, USA.

[7] Department of Thoracic and Cardiovascular Surgery, The University of Texas MD Anderson Cancer Center, Houston, TX 77030, USA.

[8] TRACTION, The University of Texas MD Anderson Cancer Center, Houston, TX 77030, USA.

[9] Department of Cancer Biology, The University of Texas MD Anderson Cancer Center, Houston, TX 77030, USA

[10] Department of Surgery, University of British Columbia, Vancouver, BC, V5Z 4E3, Canada

[11] Diabetes Research Group, British Columbia Children's Hospital Research Institute, 950 West 28th Avenue, Vancouver, BC, V5Z 4H4, Canada

[12] Department of Cell and Developmental Biology, University of Pennsylvania, Perelman School of Medicine, Philadelphia, PA 19194, USA

[13] Immunobiology and Transplant Science Center and Department of Surgery, Houston Methodist Hospital, Houston, TX 77030, USA
Department of Epigenetics and Molecular Carcinogenesis, Division of VP, Research
[14] Department of Oncology, IRBM Spa, Via Pontina Km 30 600, Pomezia, Rome 00071, Italy.
[15] Department of Pathology, Division of Pathology/Lab Medicine, The University of Texas MD Anderson Cancer Center, Houston, TX
[16] Department of Translational Molecular Pathology, The University of Texas MD Anderson Cancer Center, Houston, TX 77030, USA.
[17] Vita-Salute San Raffaele University, Milan 20132, Italy
[18] Proteomics Core Facility, Department of Bioinformatics and Computational Biology, The University of Texas MD Anderson Cancer Center, Houston, TX 77030, USA.
[19] Department of Epigenetics and Molecular Carcinogenesis, Division of VP, Research, The University of Texas MD Anderson Cancer Center, Houston, TX 77030, USA.
[20] Corresponding authors

Correspondence:

Francesca Citron, Pharm.D., Ph.D.
Department of Genomic Medicine
The University of Texas MD Anderson Cancer Center
1901 East Road,
Houston, Texas 77054
713-745-9338
FCitron@mdanderson.org

Andrea Viale, M.D.
Department of Genomic Medicine
The University of Texas MD Anderson Cancer Center
1901 East Road,
Houston, Texas 77054
713-792-8494
AViale@mdanderson.org

Giulio F. Draetta, M.D., Ph.D.
Department of Genomic Medicine
The University of Texas MD Anderson Cancer Center
1901 East Road
Houston, Texas 77054
713-792-6390
GDraetta@mdanderson.org

Abstract

It is unclear how cells counteract the potentially harmful effects of uncoordinated DNA replication in the context of oncogenic stress. Here, we identify the WRAD (WDR5/RBBP5/ASH2L/DPY30) core as a modulator of DNA replication in pancreatic ductal adenocarcinoma (PDAC) models. Molecular analyses demonstrated that the WRAD core interacts with the replisome complex, with disruption of DPY30 resulting in DNA re-replication, DNA damage, and chromosomal instability (CIN) without affecting cancer cell proliferation. Consequently, in immunocompetent models, DPY30 loss induced T cell infiltration and immune-mediated clearance of highly proliferating cancer cells with complex karyotypes, thus improving anti-tumor efficacy upon anti-PD-1 treatment. In PDAC patients, DPY30 expression was associated with high tumor grade, worse prognosis, and limited response to immune checkpoint blockade. Together, our findings indicate that the WRAD core sustains genome stability and suggest that low intratumor DPY30 levels may identify PDAC patients who will benefit from immune checkpoint inhibitors.

Keywords: Pancreatic cancer, WRAD core, DPY30, DNA replication, chromosomal instability, immunoediting, immunotherapy

Introduction

The occurrence of aneuploidy, a condition characterized by a deviation from the normal chromosome number, is differentially sensed in normal and tumor cells (1). In normal cells, aneuploidy triggers molecular checkpoint activation and immune cells recruitment for their own destruction (2, 3). In contrast, in transformed cells, aneuploidy modulates the expression of cancer driver genes (4), favors tumor-intrinsic heterogeneity, phenotypic plasticity (1), and induces genomic instability (5), which can fuel tumor evolution (6, 7). While cell-intrinsic mechanisms have been implicated in contributing to genomic instability in tumors (8, 9), the molecular mechanisms determining the evolutionary trajectory of genomic instability in cancer cells are poorly understood.

To ensure faithful genome maintenance, precise replication of the entire genome occurs only once per cell cycle through a highly conserved and tightly regulated process that begins with the licensing of DNA replication origins (10). Replication licensing is restricted to the G1 phase of the cell cycle and is defined by the loading of the pre-replicative complex (pre-RC), which comprises the origin of replication complex (ORC1-6 complex), Cdt1 (chromatin licensing and DNA replication factor 1), Cdc6 (cell division cycle 6), and DNA helicase (minichromosome maintenance complex; MCM), onto DNA (11-13). As cells progress through the division cycle, DNA replication origin firing is regulated by the phosphorylation of the pre-RC by CDKs and DKK (Cdc7/Dbf4 kinase), which in turn recruit Cdc45 and GINS as accessory factors to fully initiate DNA replication (10, 13-16).

Inaccurate genome duplication, including under- or over-replication of DNA in late S or G2/M phase, can trigger deleterious consequences, such as DNA damage, chromosomal instability (CIN), and aneuploidy. This ultimately leads to aberrant genome architecture (17-19), dysplasia and malignant transformation when surveillance mechanisms fail to clear the damaged cells (12, 20-22). Although the mechanisms that prevent uncoordinated DNA replication in normal cells are well characterized (10, 13, 23-25), it remains unclear how cancer cells limit unscheduled DNA replication, especially given its increased frequency in the context of aberrant oncogenic signaling (e.g. *KRAS* mutation), loss of cell cycle checkpoints (e.g. *TP53*, *CDKN2A*), and cumulative alterations in epigenetic regulators (e.g. *KMT2B*, *KMT2C*, *KMT2D*, *SETD1A*, and *SETD1B*) – all of

which are commonly observed in tumors such as pancreatic ductal adenocarcinoma (PDAC) (26-30).

Previously, we discovered that multiple members of the COMPASS complex (WDR5, ASH2L, Menin) are critical for PDAC tumorigenesis and cancer progression in *KRAS/TP53*-mutated backgrounds (31, 32). In mammals, COMPASS complexes are composed of one of six methyltransferase catalytic subunits of the SET1/MLL family (KMT2A, KMT2B, KMT2C, KMT2D, SET1A, SET1B) and the WRAD core (WDR5, RbBP5, ASH2L, DPY30). The full complement of these proteins is required for efficient histone-3-lysine-4 (H3K4) methylation as well as the regulation of transcriptional initiation and elongation of target genes (33-36).

While WDR5 has been extensively characterized as a core scaffolding component of SET1/MLL methyltransferases and demonstrated to be essential for gene transcription, DPY30 is relatively understudied compared to other WRAD components. It is known that DPY30 must bind ASH2L to enable histone H3K4 trimethylation (37), with loss of DPY30 expression leading to global reductions in H3K4 trimethylation levels in multiple model systems (38-45). Studies in yeast suggest that, within the WRAD core, DPY30 may stabilize the COMPASS complex to ensure the correct positioning of H3K4 methylation at promoters, especially for low-transcribed genes. Indeed, in human and mouse models, DPY30 expression appears to be essential for the differentiation of embryonic stem cells as well as for hematopoietic, pancreatic, and neural progenitor/stem cells (38-44).

Here, in cancer cells, we identify a role for the WRAD core in maintaining genomic stability that is independent of its role in SET/MLL activity. We demonstrate that the WRAD core interacts with members of the DNA helicase complex, and, upon loss of DPY30, tumor cells undergo DNA re-replication, resulting in genomic instability. *In vivo*, loss of DPY30 increases the tumor mutational burden (TMB) and CIN, triggering a robust CD8-dependent anti-tumor immune response. Our findings implicate the WRAD core in preserving genome stability in cancer cells and suggest that DPY30 inhibition merits further exploration as a therapeutic concept to kill tumor cells by genome destabilization and sensitization to immune-checkpoint inhibitor therapy.

Results

Loss of DPY30 is dispensable for PDAC cell proliferation and H3K4 methylation.

We first assessed the impact of silencing the expression of proteins comprising the WRAD core on PDAC cell proliferation. Consistent with our previous observations (31, 32), doxycycline-induced silencing of *WDR5* (*shWDR5*), *ASH2L* (*shASH2L*), or *RBBP5* (*shRBBP5*) strongly restrained cell proliferation *in vitro* (**Fig. 1a, Extended Data Fig. 1a-e**). Unexpectedly, shRNA-mediated silencing of *DPY30* (*shDPY30*) in human PDAC cells, as well as sgRNA-mediated *Dpy30* knockout (*Dpy30*-KO) in mouse PDAC cells from KPC (*Ptf1a*^{Cre};*KRas*$^{lsl\text{-}G12D/wt}$;*Trp53*$^{R172H/wt}$) (46) and KP$^{-/-}$C (*Ptf1a*^{Cre};*KRas*$^{lsl\text{-}fl}$;*Trp53*$^{fl/fl}$) (47)mouse models did not affect cell proliferation (**Fig. 1b-c, Extended Data Fig. 1f-n**). We confirmed the lack of any effect of DPY30 loss on cell proliferation *in vivo*, showing that human *DPY30*-KO PDAC cells injected into immunodeficient NSG mice did not grow differently compared to controls (**Fig. 1d-g**, **Extended Data Fig. 1o-p**). Hence, our data show that PDAC cells are vulnerable to the loss of the WRA (WDR5, RBBP5, ASH2L) core, but not to DPY30 depletion.

Because the three-component WRA core has been shown to be the minimal required cofactor for supporting SET/MLL methyltransferase activity on histone H3K4, while the presence of DPY30 is only needed to enhance the specificity of the enzymatic activity (33), we explored whether inhibiting *DPY30* or *WDR5* expression in PDAC cells could differentially affect H3K4 methylation. To this end, we compared the acute effects of *DPY30* or *WDR5* loss on chromatin profiles in patient-derived PDAC cell lines transduced with doxycycline-inducible *shDPY30* or *shWDR5* by performing transposase-accessible chromatin using sequencing (ATAC-seq) and H3K4 tri-methylation (H3K4me3) and H3K27 acetylation (H3K27ac) chromatin immunoprecipitation sequencing (ChIP-seq), the latter of which provides readouts of COMPASS activity at gene regulatory regions (31, 48). Because WDR5 loss has a detrimental impact on the cell cycle (31, 39) (**Fig. 1a**), we excluded any confounding effects of WDR5 loss on proliferation by collecting cells at 48 hours after shRNA induction *via* doxycycline treatment, a timepoint sufficient for protein downregulation (**Extended Data Fig. 2a-b**). Cluster analysis of open genomic regions, as well as genomic regions marked by H3K4me3 and H3K27ac, revealed that *WDR5*-silenced cells exhibited chromatin states

125 that were distinct from *DPY30*-silenced cells, which clustered with control cells. This
126 suggests that, unlike the effects observed upon WDR5 loss, the acute and short depletion
127 of *DPY30* is not sufficient to alter chromatin accessibility and states (**Fig. 1h-j**).
128 Consistently, WDR5, but not DPY30, downregulation affected the total levels of H3K4me3
129 and H3K4me1 histone marks (**Extended Data Fig. 2b, f**).

130 Although genome-wide analysis of chromatin at regulatory regions proximal to
131 gene transcriptional start sites (TSS) did not reveal significant differences between
132 *DPY30* and *WDR5* silenced cells (**Extended Data Fig. 2c-e**), the H3K4me3 profiles of
133 these two groups appear markedly different. Specifically, *DPY30* silencing did not affect
134 the pattern of H3K4me3, indicating that DPY30 loss likely does not broadly alter the
135 transcriptome of these cancer cells (**Fig. 1k**). In contrast, *WDR5* silencing significantly
136 altered H3K4me3 patterns, resulting in the repression of thousands of genomic regions
137 (**Fig. 1k, Extended Data Table S1**). To determine the functional annotations for the
138 regions affected by WDR5 depletion, we conducted pathway analysis of genes located in
139 these genomic regions and identified pathways involved in interferon alpha and gamma
140 response, inflammatory response, and DNA damage (**Extended Data Fig. 2g, Extended
141 Data Table S1**).

142 To dissect the biological role of the WRAD core in PDAC cells, we next performed
143 bulk RNA-sequencing (RNAseq) analysis of patient-derived PDAC cells stably expressing
144 *shDPY30*, *shWDR5*, or shCTR and treated with doxycycline for 48 hrs as described
145 above (**Extended Data Fig. 2a**). *WDR5*, but not *DPY30*, silencing profoundly modulated
146 the transcriptome of PDAC cells (**Extended Data Fig. 3a**), which is consistent with the
147 essential role of WDR5 in regulating gene transcription (31, 36, 39, 49). Specifically, and
148 in line with our epigenomics analysis (**Fig. 1k, Extended Data Table 1**), *WDR5* silencing
149 induced a remarkable downmodulation of genes involved in the interferon alpha and
150 gamma response as well as a dysregulation of pathways involved in mRNA translation
151 and RNA processing (**Extended Data Fig. 3b, Extended Data Table S2**). Although
152 *DPY30* silencing did not deregulate the transcriptome of PDAC cells as strongly as *WDR5*
153 silencing, it induced a positive regulation of pathways involved in interferon signaling,
154 inflammatory response, and DNA damage (**Extended Data Fig. 3e-g, Extended Data
155 Table 2**). Overall, our data indicate that *DPY30* or *WDR5* silencing leads to distinct

156 epigenomic and transcriptomic changes in PDAC, thus demonstrating that the WRAD
157 core has non-redundant roles in maintaining cell proliferation and transcriptional activity
158 in PDAC.
159
160 **WRAD core directly interacts with the MCM complex.**
161 To further investigate the discrepancies in the proliferative, epigenetic, and
162 transcriptional phenotypes that emerged upon depletion of different WRAD core members
163 in PDAC cells, we expanded our investigation into the biological function of DPY30 in
164 PDAC. To this end, we immunoprecipitated endogenous DPY30 protein in two human
165 (PATC53 and PATC66) and one mouse (KPC) PDAC-derived cell models, all of which
166 carry *TP53* and *KRAS* mutations (31, 32). Unbiased proteomic analysis showed that
167 multiple top-scoring interactors of DPY30 are involved in chromatin remodeling, RNA
168 metabolism, splicing, and gene transcription (**Extended Data Fig. 4a-d, Extended Data**
169 **Table S3**), consistent with the role of DPY30 as a cofactor supporting histone methylation
170 and gene transcription regulation by COMPASS complexes (38-44). Proteins involved in
171 DNA replication, DNA damage, and cell cycle regulation were also identified as DPY30
172 interactors (**Extended Data Fig. 4a-d, Extended Data Table S3**). These included
173 proteins previously unknown to interact with DPY30, such as multiple members of the
174 DNA replisome, including the MCM complex and WDHD1 (**Fig. 2a, Extended Data Fig.**
175 **4d**). We validated these findings by expressing either mouse or human HA-tagged DPY30
176 with mouse or human MCM subunits and found that DPY30 bound most strongly to MCM6
177 compared to others (**Fig. 2b, Extended Data Fig. 4e**). Notably, proximity ligation analysis
178 (PLA) revealed that endogenous DPY30 lies in proximity (<40nm) of both MCM6 and
179 WDHD1, strongly suggesting that DPY30 may be a core component of the DNA replisome
180 (**Fig. 2c)**. To explore whether the interaction of DPY30 with the replisome was cell cycle-
181 dependent, we expressed the fluorescent ubiquitination-based cell cycle indicator
182 (FUCCI) system in human PDAC cells (50). By enabling the real-time tracking of cell cycle
183 progression in live cells (54), this approach allowed us to sort PDAC cells by cell cycle
184 phase and then perform immunoprecipitation (IP) assays for endogenous DPY30
185 (**Extended Data Fig. 4f-g)**. Unbiased proteomic analysis of affinity-purified samples
186 showed that members of the COMPASS complex were, as expected, enriched in DPY30

187 pull-downs and that these interactions were independent of cell cycle phase (**Extended**
188 **Data Fig. 4h).** Furthermore, this analysis confirmed that WDHD1 and all MCM complex
189 members, including MCM10, MCM3AP, and MCMBP, interacted with DPY30, with all
190 replisome components except for MCM2, MCM4, and MCM10 interacting with DPY30 in
191 a cell cycle-independent fashion **(Extended Data Fig. 4i).** Additionally, we found that
192 WDR5 also interacted with MCM complex members (**Fig. 2d)**. In cell nuclei, WDR5 was
193 shown to reside topographically close to MCM6 and WDHD1 (**Fig. 2e-f, Extended Data**
194 **Fig. 4j)**, similar to what was seen for DPY30 (**Fig 2c**). Importantly, endogenous WDR5,
195 ASH2L, and RBBP5 could be precipitated with MCM6, suggesting that the whole WRAD
196 participates in this interaction (**Extended Data Fig. 4k-m)**. Interestingly, destabilization
197 of the WRAD core through silencing of either *WDR5* or *DPY30* impeded the endogenous
198 binding of DPY30 to MCM6 (**Fig. 2g-h).**
199 To explore whether WRAD core integrity is necessary for MCM6 binding, we
200 overexpressed a mutant isoform of DPY30 (L69D) known to hinder the DPY30:ASH2L
201 interaction and the proper assembly of the WRAD core (51). Remarkably, $DPY30^{L69D}$
202 expression prevented the DPY30:MCM6 interaction as well as the assembly of the WRAD
203 core **(Fig. 2i, Extended Data Fig. 4n)**. We employed a similar approach by
204 overexpressing two WDR5 mutant isoforms (L240K and V268E) that have altered WDR5-
205 binding motif (WBM) domain and are known to disrupt the interaction of WDR5 with
206 RBBP5 and cMyc (31). We consistently found that disrupting the WRAD core assembly
207 strongly reduced the interaction between WDR5 and MCM6 **(Fig. 2j, Extended Data Fig.**
208 **4o)**. Altogether these observations suggest that the stability of the WRAD core is
209 necessary for the interaction between the WRAD core and the MCM6 subunit of the MCM
210 complex.
211
212 **The WRAD core participates in replication fork dynamics**
213 Because the MCM complex represents the DNA helicase activated at the start of
214 DNA replication (10, 12-15, 23), we tested whether WRAD contributes to replication fork
215 progression. Using an iPOND assay to recover proteins bound to newly synthesized DNA,
216 we found that WRAD core members localized at DNA replication fork initiation sites (2
217 min of EdU pulse), persisted during DNA elongation (5-10 min of EdU pulse), but

218 disappeared at later time points (chase) **(Fig. 3a, Extended Data Fig. 5a)**. Notably,
219 histone H3, a marker for nucleosome incorporation and an indicator of SET/MLL
220 canonical activity, was barely detectable at 2 min of EdU pulse, gradually incorporated at
221 5 and 10 minutes, and strongly detected during the chase (**Fig. 3a, Extended Data Fig.**
222 **5a)**. This contrasting behavior between WRAD and H3 serves as an internal control,
223 confirming that WRAD members detected at DNA replication forks are not associated
224 with chromatin-bound proteins (**Fig. 3a, Extended Data Fig. 5a)**. These data strongly
225 indicate that, in the context under study, the WRAD core directly interacts with the DNA
226 replication fork in a nucleosome-independent manner. Importantly, analysis of the
227 interactions between proteins and the nascent DNA using a single cell-based method
228 (SIRF assay) (52, 53) showed that WDR5, but not DPY30, directly interacts with nascent
229 DNA, further supporting a pivotal role for the WRAD core in DNA replication dynamics
230 (**Fig. 3b**).

231 Because WDR5 deregulation affects distinct biochemical pathways and results in
232 rapid induction of cell death (**Fig. 1**) (31), we sought to avoid any confounding effects by
233 focusing further mechanistic studies on DPY30. First, iPOND analysis found that *Dpy30*-
234 KO did not destabilize MCM6 nor WDR5 binding at replication forks, suggesting that
235 DPY30 is not directly involved in regulating fork assembly (**Fig. 3c, Extended Data Fig.**
236 **5b**). Second, to examine the effect of DPY30 on replication fork efficiency, we performed
237 a DNA fiber assay in *Dpy30*-KO and control cells. *Dpy30*-KO resulted in slower fork
238 progression rates and reduced symmetry between incorporation of the two different
239 nucleotide analogues, suggesting that *Dpy30* loss may promote replication stress (**Fig.**
240 **3d-e**). Additionally, we observed increased frequency of overlap between the two
241 incorporated nucleotide analogues in *Dpy30*-KO cells compared to controls, indicating
242 DNA re-replication in these cells, and further supporting the hypothesis that *Dpy30* loss
243 may contribute to replication stress (**Fig. 3f-g**).

244 To corroborate our findings, we next developed an unbiased DNA re-replication
245 sequencing assay ("Re-repli-seq", see methods section) (**Extended Data Fig. 5c**).
246 Specifically, S phase synchronized KPC controls or Dpy30-KO cells were released in
247 presence of CldU (45 min) followed by a second pulse of IdU (45 min) (**Extended Data**
248 **Fig. 5c**). The cells were then split, and a ChIP assay was performed using antibodies

249 against the incorporated CldU and IdU separately, followed by next generation
250 sequencing. After, sequence alignment to reference genome, we represented the data as
251 a ratio of incorporated CldU:IdU (38). In case of DNA re-replication, sequencing of double-
252 labelled immunoprecipitated genomic regions should result in an increased overlap
253 between CldU and IdU sequencing reads. Data analysis showed that, compared to
254 controls, the Dpy30-depleted KPC cells showed broader genomic domains with CldU:IdU
255 ratio close to zero, which means the nucleotide analogues are incorporated equally and
256 overlap in the same genomic regions (**Figure 3h-i**). As an example, regions of different
257 chromosomes (Chr1, Chr2, Chr4, Chr6, Chr10 and Chr16) displayed domains of
258 replicated DNA with an overlapped pattern of CldU:IdU ratio more prominently distributed
259 in Dpy30-depleted cells compared to control cells, that instead, showed a more
260 coordinated replication profile (**Extended Data Fig 5d-e**). Our genome-wide analysis of
261 CldU:IdU incorporation strongly supports that Dpy30 and the WRAD core are required to
262 sustain a coordinated DNA replication during the S phase in tumor cells.
263 Because excessive DNA replication can trigger DNA damage, we found that during
264 unperturbed growth condition, *Dpy30*-KO KPC cells showed stronger γH2AX (pS139) and
265 pRPA (pS4-8) staining compared to control cells (**Fig. 3j, Extended Data Fig. 5f-h**).
266 Consistently, γH2AX levels *in vivo* were dramatically increased in both *Dpy30*-KO KPC
267 and human-derived *DPY30*-KO or knockdown (KD) tumors compared to controls
268 (**Extended Data Fig. 6a-b**). Further, bulk RNAseq analyses performed in mouse-derived
269 Dpy30-KO and control PDAC cells revealed a deregulation of pathways involved in DNA
270 damage and G2/M checkpoint (**Extended Data Fig. 6c-d, Extended Data Table S4**),
271 Interestingly, Dpy30-depleted cells showed an extensive upregulation of inflammatory
272 pathways (**Extended Data Fig. 6c-d, Extended Data Table S4)**, which might have been
273 activated as a consequence of persistent DNA damage (2, 55, 56). These data align with
274 our previous work (31) showing that the WDR5 silencing strongly increased DNA damage
275 and induced a sustained G2/M accumulation in PDAC cells. Further, these observations
276 suggest that PDAC cells can tolerate the incremental DNA damage caused by *DPY30*
277 loss, but cannot survive the extensive DNA injuries and transcriptomic rewiring upon
278 WDR5 depletion. This suggests that the intact WRAD core sustains genomic stability by
279 counteracting excessive DNA replication.

280

281 **DPY30 maintains genome integrity by limiting excessive DNA replication and**
282 **stabilizing the S-to-G2/M transition**

283 The risk of DNA re-replication increases at the S-to-G2/M boundary, during which
284 Cdc6 and Cdt1 are in their active forms and the expression of geminin, an inhibitor of
285 DNA replication, has not yet peaked (10, 13, 23). To investigate whether *DPY30* loss
286 disrupts cell cycle dynamics in these phases specifically, we synchronized PDAC cells in
287 S phase using a double-thymidine block and collected cells at different time points after
288 release (**Extended Data Fig. 6e-f**). In line with our observations in proliferation assays
289 (**Fig. 1a-d, Extended Data Fig. 1a-n**), we observed that *Dpy30* KO did not grossly affect
290 cell cycle distribution in non-synchronized cells (**Extended Data Fig. 6e-f**). However, in
291 synchronized cells, a larger proportion of *Dpy30*-KO cells compared to control cells
292 advanced towards the G2/M boundary by 2 hours after release from S phase (**Extended**
293 **Data Fig. 6e-f**). Additionally, at this time point, we detected an increased percentage of
294 aneuploid cells (DNA content >4N), higher DNA damage, increased BrdU incorporation,
295 as well as higher phosphorylation of pS139 MCM2, pS54 Cdc6, and pS10 histone H3 in
296 Dpy30-KO cells compared to controls, all of which support an uncoupling of DNA
297 replication and cell cycle progression upon *Dpy30* loss (**Extended Data Fig. 6e-h**). We
298 further observed that, while there were no significant differences in the expression of
299 geminin in the arrested cells (**Extended Data Fig. 6h-i**), geminin expression was strongly
300 downmodulated upon release in *Dpy30*-KO cells. We next synchronized *Dpy30*-KO or
301 control PDAC cells in S phase using a double thymidine block, and in G2/M phase using
302 a thymidine-nocodazole block (**Extended Data Fig. 6j)**. Strikingly, Western blot analysis
303 showed that the dysregulation of Cdc6 and geminin expression was restricted to the G2/M
304 phase rather than the early S phase (**Extended Data Fig. 6j**). Overall, our data indicate
305 that, upon DPY30 depletion, the risk of DNA re-replication increases at the S-to-G2/M
306 boundary due to the uncoupled regulation of the Cdc6/Geminin axis (20, 24, 57-59).

307 During the G2/M and G1 phases, Geminin stability is tightly regulated by the
308 anaphase promoting complex/cyclosome (APC/C), leading to its proteasome-dependent
309 degradation (60). As a member of the E3 ubiquitin ligase family, APC/C requires the
310 modification of the cullin ring with NEDD8, an-ubiquitin-like protein, for its activity (61).

311 Chemical inhibition of NEDD8 promotes DNA re-replication through the stabilization of
312 Cdt1 and Cdc6 protein expression (24, 61-63). Hence, we hypothesized that NEDD8
313 inhibitors, such as MLN4924, may exacerbate the uncoupling between DNA replication
314 and G2/M transition in Dpy30-depleted cells by. As expected, human nearly diploid RPE-
315 1 cells treated with MLN4924 showed increased expression of Cdc6 in both control and
316 *DPY30*-KO cells compared to untreated ones (**Extended Data Fig. 7a**). Further, when
317 compared to control RPE-1 cells, geminin expression was remarkably lower upon DPY30
318 depletion and MLN4924 treatment, and the spontaneous activation of γH2AX was
319 observed upon DPY30 depletion and then boosted by MLN4924 treatment (**Extended**
320 **Data Fig. 7a**). Finally, we observed increased BrdU incorporation in cells treated with
321 MLN4924, with the highest incorporation in *DPY30*-KO cells (**Extended Data Fig. 7b**).
322 These data were confirmed in KPC cells, showing dysregulated geminin and γH2AX
323 expression, as well as increased percentage of aneuploid cells, in *Dpy30*-KO compared
324 to control cells (**Extended Data Fig. 7c-d**). Overall, our data suggested that *Dpy30* loss
325 leads to DNA re-replication through a potent perturbation of the Cdc6/geminin balance
326 during the G2/M phase.
327 Finally, because uncoordinated replication can contribute to chromosomal
328 instability (CIN), we investigated whether DPY30 may induce this phenomenon (16, 22,
329 25, 64). Indeed, *DPY30*-KO in both human and mouse PDAC-derived models increased
330 the percentage of cells with chromosome mis-segregation and micronuclei *in vitro* and *in*
331 *vivo (***Fig. 3k, Extended Data Fig. 7e-g***)*. Consistently, metaphase spreads showed an
332 increased in the number of chromosomal breaks and fusions *in vitro* (**Fig. 3l, Extended**
333 **Data Fig. 7h-i**). Collectively, these data support a critical role for DPY30 in maintaining
334 genome stability and suppressing DNA re-replication at the G2/M transition.
335
336 ***DPY30*-KO cells display complex karyotypes and elicit a T cell-mediated**
337 **immune response.**

338 To assess whether the genome instability induced by DPY30 loss may impact
339 tumor immunogenicity *in vivo*, we injected control or *Dpy30*-KO KPC and $KP^{-/-}C$ cells into
340 cohorts of NSG, nude, and C57BL/6 mice. Strikingly, *Dpy30*-KO strongly impaired tumor

341 growth compared to controls in immune-competent C57BL/6 mice but had no effect on
342 tumor growth in immunodeficient mice (**Fig. 4a-d, Extended Data Fig. 8a-d**). Moreover,
343 histological analysis revealed that *Dpy30*-KO tumors grown in C57BL/6 mice appeared
344 more differentiated and characterized by an increased number of mucin-positive ductal-
345 like structures compared to their respective controls (**Fig. 4e-f**). Of note, in models of
346 orthotopic transplantation, we observed that Dpy30 depletion significantly prolonged
347 animal lifespan (**Fig. 4g, Extended Data Fig. 8e**).

348 To eliminate potential confounding effects due to CRISPR/Cas9-related
349 immunogenicity (65), we injected mouse cells derived from $KP^{-/-}C$ tumors stably
350 expressing doxycycline-inducible shDpy30 or shCTR into NSG or C57BL/6 mouse
351 backgrounds. Also in this setting, we confirmed that Dpy30-depleted tumors grown in
352 immunocompetent mice were smaller and more differentiated compared to controls, while
353 in NSG mice no major differences were detected (**Extended Data Fig. 8f-i**). Further, we
354 confirmed that *Dpy30* silencing strongly prolonged animal lifespan (**Extended Data Fig.**
355 **8j**).

356 Intriguingly, the cell proliferative index, evaluated as Ki67- and pS10-H3-positive
357 staining, was remarkably reduced in *Dpy30*-KO cells compared to controls in immune-
358 competent, but not NSG, backgrounds (**Figure 4h, Extended Data Fig. 5g and 8k-l**).
359 This suggests that, in the absence of DPY30, the immune system may inhibit growth of
360 or preferentially clear proliferating tumor cells. Interestingly, gene set enrichment analysis
361 (GSEA) from bulk RNAseq data of *Dpy30*-KO and control $KP^{-/-}C$ tumors showed a positive
362 enrichment score for pathways involved in DNA damage and repair process in
363 immunodeficient mice, while the same cancer cells showed upregulation of gene
364 pathways involved in inflammation, including interferon signaling, the complement
365 cascade, and PD-1 signaling, in an immunocompetent background (**Extended Data Fig.**
366 **8m-n, Extended Data Table S5**). Because CIN can enhance the activity of the
367 cGAS/STING pathway, which in turn regulates the expression of the type I interferons
368 and related gene products (56), we sought to evaluate the expression of STING upon
369 Dpy30 depletion. Immunostaining analysis of KPC showed a potent activation of STING
370 in *Dpy30*-KO cells compared to controls both *in vitro* and *in vivo* **(Fig. 4i, Extended Data**
371 **Fig. 8o).** Altogether, these data suggest that *Dpy30* loss can trigger a T cell-mediated

372 immune response *in vivo* through DNA damage and CIN-dependent activation of the type
373 I interferons, the latter of which occurs through the cGAS/STING pathway.
374 Next, we performed single-cell RNAseq (scRNAseq) on *Dpy30*-KO and control
375 KPC tumors (n=3 per condition) grown in immunocompetent mice. Dimensionality
376 reduction analysis of sub-clusters of tumor cells revealed only a partial overlap between
377 the transcriptomes of *Dpy30*-KO and control tumor cells (**Fig. 4j)**. Specifically, we
378 identified a population of highly proliferative tumor cells that was expanded in control
379 tumors but minimally represented in *Dpy30*-KO tumors (**Fig. 4j-k**). Expression analysis of
380 cell cycle regulators corroborated our observation, showing a reduced expression of
381 proliferative genes (*Ccnb2, Cdc20, Top2a, Aurka, Aurkb, Wee1*) (**Fig. 4k)** and,
382 consequently, supporting the hypothesis that highly proliferative tumor cells are
383 selectively cleared by the immune response in the absence of Dpy30. Further, GSEA
384 confirmed an upregulation of genes involved in interferon signaling and inflammatory
385 response pathways (Il6/Stat3, allograft rejection, and complement) upon Dpy30 depletion
386 (**Fig. 4l**). Remarkably, *B2m*, *Cd74*, *H2-K1*, and *H2-D1*, genes involved in antigen
387 presentation, were among the top-scoring genes in *Dpy30*-KO cells (**Fig. 4m**). Indeed,
388 when comparing *Dpy30*-KO tumors to controls, immunostaining analysis confirmed an
389 increased infiltration of CD3+ tumor-infiltrating lymphocytes (TILs) as well as an increase
390 of cancer associated-fibroblasts (CAFs) (αSMA+), the latter likely the result of the
391 depletion of the epithelial compartment (**Fig. 4n, Extended Data Fig. 8p**). Accordingly,
392 examination of the tumor microenvironment (TME) at the single cell level revealed an
393 increased number of CAFs, B cells, NK cells, and T cells in *Dpy30*-KO tumors grown in
394 an immunocompetent background when compared to controls (**Fig. 5a-c, Extended Data**
395 **Fig. 9a-b**). These findings were corroborated by flow cytometry-based
396 immunophenotyping, which demonstrated a significant increase in the number of all
397 infiltrating T cell subsets and NK cells in *Dpy30*-KO tumors. Among the immune cells, the
398 CD8+ T cells were the predominant population, suggesting that they may be the primary
399 contributor to the anti-tumor response (**Fig. 5d, Extended Data Fig. 9c-e**). Importantly,
400 compared to control tumors, CD8+ T cells in *Dpy30*-KO tumors displayed lower
401 expression of exhaustion marker *Tox* as well as higher expression of cytotoxic markers
402 such as interferon gamma (*Ifng*), granzyme B (*Gzmb*), and natural killer cell granule

403 protein 7 (*Nkg7*) (**Fig. 5e, Extended Data Fig. 9f-h**). Altogether, these findings suggest
404 that CD8+ T cells are activated and may selectively clear *Dpy30*-KO tumor cells with
405 increased immunogenicity due to genomic instability.

406 To test this hypothesis, whole-exome sequencing (WES) was performed on
407 *Dpy30*-KO or control tumors grown in NSG or C57BL/6 mice. We found that, in a
408 permissive immune-deficient environment, *Dpy30*-KO tumors grew without restraint and
409 tolerated a higher mutational burden (TMB) compared to *Dpy30*-proficient controls
410 (**Extended Data Fig. 9i**). However, the same cells transplanted in a selective immune-
411 competent background displayed lower TMB (**Extended Data Fig. 9i**), thus suggesting
412 that cancer cells undergoing uncoordinated DNA replication and CIN were being cleared
413 from tumors. To corroborate our findings and quantify the extent of this depletion, we
414 generated barcoded KPC cells using our established platform (66, 67). We then
415 transiently infected barcoded KPC cells with sgRNAs targeting *Dpy30* or a scramble
416 control and injected them into NSG or C57BL/6 mice. Explanted tumors were subjected
417 to next-generation sequencing (NGS) for barcode detection. Pairwise comparison of
418 subclonal composition of *Dpy30*-depleted versus control KPC cells grown in
419 immunodeficient or immunocompetent mice showed a dramatic depletion of barcodes in
420 the *Dpy30*-KO cells transplanted in C57BL/6 mice compared to an immunodeficient
421 counterpart (**Fig. 5f**). Further, we injected *Dpy30*-KO or control KPC cells into
422 immunocompetent C57BL/6 mice and collected tumors at different time points (day 10,
423 day 15 and day 25). Multiplexed immunostaining analysis showed that, over time, the
424 number of TILs strongly increased exclusively in *Dpy30*-KO tumors compared to controls
425 (**Fig. 5g-h**). This immune infiltration, in the *Dpy30*-KO tumors, was paralleled by a net
426 increase in the cleaved caspase 3 (CC3) staining, a *bone fide* marker of apoptotic cell
427 death, as well as a pronounced reduction in the number of Ki67+ tumor cells (**Fig. 5i-j**).
428 Altogether these data indicate that, in a mutated *TP53/KRAS* genetic background,
429 increases in CIN and TMB due to DPY30 loss enhance the immunogenicity of PDAC cells
430 and a consequent T cell-mediated response.
431

432 **DPY30 expression correlates with poor response to immune checkpoint**
433 **blockade and tumor staging.**

434 To determine whether CD8+ T cells are responsible for clearing cells harboring a
435 high TMB (high-TMB) due to DPY30 depletion, we injected *Dpy30*-KO or control KPC
436 cells into C57BL/6 mice and depleted the CD8+ T cell population using an anti-CD8
437 monoclonal antibody (**Fig. 6a**). We found that CD8+ T cell depletion was sufficient to
438 rescue the phenotype induced by *Dpy30* loss, considerably accelerating tumor growth,
439 and reducing lifespan when compared to that of control mice (**Fig. 6b-c**). To explore
440 whether the activation of cytotoxic T cells upon *Dpy30* loss may synergize with
441 immunotherapy, we randomized transplanted mice to receive either 8 mg/kg of anti-PD-
442 1 monoclonal antibody or isotype control intraperitoneally three times a week for two
443 consecutive weeks. Anti-PD-1 treatment dramatically reduced tumor growth and greatly
444 extended the median survival of mice bearing *Dpy30*-KO tumors, with 60% of these
445 animals showing complete tumor regression (**Fig. 6a-c**).
446 To explore the translational relevance of our findings, we next evaluated *DPY30*
447 expression in PDACs by performing immunohistochemical (IHC) analysis on a tissue
448 microarray (TMA) comprising of human PDAC (n = 128) and matched tumor-adjacent
449 normal pancreas tissue samples (n = 128) collected at the University of Texas MD
450 Anderson Cancer Center. We found that *DPY30* expression was low in normal pancreatic
451 tissues but high in PDAC, particularly in poorly differentiated tumors (**Fig. 6d**). Moreover,
452 we showed that low *DPY30* expression was associated with better survival in the cohort
453 of patients included in the TMA (**Fig. 6e**). To further investigate this association, we
454 interrogated The Cancer Genome Atlas (TCGA) PDAC database and found that,
455 compared to other WRAD core members, high *DPY30* expression was significantly
456 associated with shorter overall patient survival (**Fig. 6f, Extended Data Fig. 10a-c**).
457 Based on these clinical findings, we hypothesized that DPY30 expression in PDAC may
458 be modulated over tumor progression. To test this, we collected pancreas tissues from
459 the KPC mouse model at different time points (46, 68, 69). In support of our hypothesis,
460 IHC analysis showed low DPY30 expression in normal pancreas and metaplastic lesions
461 but a striking increase in expression in transformed cells that became increasingly higher
462 as the lesions progressed from pancreatic intraepithelial neoplasia (PanIN) to high-grade
463 PDAC (**Extended Data Fig. 10d**). We also noticed that, in normal pancreas, DPY30 was
464 mostly expressed in the endocrine compartment, in line with its role in endocrine cell

465 functional maturation (38, 39), while being weakly detectable in pancreatic ductal and
466 acinar cells (**Extended Data Fig. 10d**). These data provide evidence that DPY30
467 expression is associated with PDAC progression in both human and mouse.

468 To examine whether DPY30 may similarly affect genome integrity and the immune
469 response in human tumors, we queried the transcriptomic data of the TCGA PDAC patient
470 cohort. GSEA analysis of 70 samples with at least 50% purity distributed according to
471 high or low *DPY30* expression showed that low *DPY30* expression was associated with
472 increased expression of genes involved in the complement response as well as in
473 interferon and IL6/STAT3 signaling pathways (**Fig. 6g**). We corroborated our data by
474 querying the transcriptomic data of 47 PDAC patient-derived xenografts (PDXs)
475 established at UT MD Anderson Cancer Center PDACs. GSEA analysis showed that
476 PDAC PDXs expressing low levels of *DPY30* are enriched in genes belonging to the
477 interferon alpha and gamma response pathways (**Extended Data Fig. 10e**). Finally, we
478 interrogated the dataset of the phase 2 PRINCE trial, in which the efficacy of the PD-1
479 inhibition (nivolumab) was assessed in patients with metastatic PDAC (70). Strikingly,
480 PDAC patients expressing low DPY30 levels showed a prolonged progression-free and
481 overall survival compared to PDAC patients with high DPY30 expression (**Fig. 6h,**
482 **Extended Data Fig. 10f-g**). Taken together, our data strongly suggest that DPY30 has a
483 role in regulating DNA replication in PDAC cells, and that low levels of DPY30 favor
484 aberrant DNA replication events that activate an interferon-dependent response that
485 recruits effectors of the adaptive immune response.
486

487 **Discussion**

488 While many studies have focused on the genetics and transcriptional fingerprint of
489 PDAC to designate subtype classification schemes for this highly heterogeneous disease,
490 these molecular subtypes have not yet consistently translated to clinical implications (28,
491 71-73). Cumulative evidence sheds light on the intricate mechanisms underpinning PDAC
492 tumorigenesis and disease progression, which involve context- and time-dependent
493 interactions between genomic and epigenomic scars (74, 75). Recently, a study of the
494 epigenome of PDAC PDXs demonstrated that epigenetic fingerprints are associated with

495 discrete transcriptional signatures and clinical features, suggesting a convergence
496 between genetics, epigenetics, tumor-intrinsic, and tumor-extrinsic features (76).
497 The disruption of evolutionarily conserved epigenetic complexes, including
498 COMPASS, has been implicated in developmental disorders and cancer, as strict
499 regulation of the activity of these complexes are critical for developmental and
500 physiological processes (37, 48). For instance, in PDAC, the cumulative incidence of
501 mutations in epigenetic regulators is approximately 35%, including recurrent mutations in
502 *KMT2B*, *KMT2C*, *KMT2D*, *SETD1A*, and *SETD1B* (26-30). Interestingly, *DPY30*
503 mutations have not been observed in any cancer.
504 While the WRAD core of COMPASS complexes is known to regulate the
505 maintenance of epigenetic information in normal and cancer cells, numerous studies have
506 demonstrated non-canonical functions of the WRAD subunits that include transcriptional
507 regulation-independent functions that regulate cell cycle progression (33-35, 49, 77-81).
508 Here, we demonstrate a novel function for the WRAD core as an effector in DNA
509 replication and fork stability, and we show that this function is independent of the core's
510 function as an MLL/Set methyltransferase (38-40, 42-44). Although loss of DPY30 did not
511 affect the proliferative ability of PDAC cells compared to the inactivation of other WRAD
512 core members, we show that DPY30 integrity is required to prevent excessive DNA
513 replication and maintain genome integrity. Specifically, molecular analyses revealed that
514 DPY30 loss leads to uncoordinated DNA replication, resulting in increased replication
515 stress and, ultimately, promoting genome instability. Moreover, *DPY30*-depleted cells
516 displayed a rapid and unchecked transition from S phase to G2/M and were observed to
517 progress through the cell cycle with mis-segregated chromosomes and persistent DNA
518 damage.
519 The S-to-G2 cell cycle checkpoint is enforced by the ATR kinase, which governs
520 the coupling of DNA replication with mitotic progression by repressing the activity of CDK1
521 and ensuring proper timing of G2-specific events (82-84). DNA re-replication can itself
522 activate ATR, which in turn arrests DNA replication and recruits DNA repair effectors (13,
523 15, 25). However, the biological mechanisms by which this ATR-mediated checkpoint can
524 sense the completion of DNA replication and distinguish this event from DNA over-
525 replication remain unknown. Our findings shed light on how tumor cells with oncogenic

526 signaling and deficient cell cycle checkpoints employ independent, novel pathways to
527 restrain DNA replication to evade cell death mechanisms. Clarifying the interplay between
528 DNA re-replication control, checkpoint activation, and repair of re-replication-associated
529 DNA lesions is fundamental for expanding our knowledge of the biology driving cancer
530 cells.

531 Whole-genome duplication and CIN frequently occur during the progression of
532 PDAC, and especially at late and metastatic stages. In particular, chromothripsis, a
533 catastrophic mitotic event driving multiple concurrent chromosome structural alterations,
534 is frequently observed in advanced PDAC (30). Interestingly, *DPY30* expression is
535 upregulated during tumorigenesis, and poorly differentiated PDACs displayed the highest
536 *DPY30* expression. This suggests that DPY30 may somehow buffer PDAC cells from
537 oncogene-driven uncontrolled replication and the detrimental effects of CIN. All models
538 evaluated in our study were *P53* deficient, thus warranting additional investigations to
539 determine whether *P53* inactivation represents a specific genetic context in which DPY30
540 function is essential for regulating DNA homeostasis. Further, because aneuploid cells
541 are characterized by deregulated metabolic programs and protein networks, future
542 studies should assess whether DPY30 loss, through induction of aneuploidy, can evoke
543 cellular adaptive responses, which may ultimately be exploited as co-lethality and
544 druggable targets (1, 6, 85).

545 Overall, our study demonstrates that DPY30 loss leads to the accumulation of
546 PDAC cells with complex karyotypes and increased TMB, which, in turn, results in the
547 selective clearance of damaged proliferating cells by CD8+ T cells. Considering the
548 paucity of treatment options for patients with PDAC, our work provides evidence that
549 PDAC with low *DPY30* expression may respond to combined therapy of immune-
550 checkpoint inhibitors and conventional chemotherapy.

551

552 **Methods**

553 **Patient-derived samples.** Patient-derived samples were obtained from
554 consented patients under an Institutional Review Board (IRB)-approved protocol LAB00-
555 0396 chaired by Dr. Michael Kim. (UTMDACC).

556 **Cell Biology Experiments**

557 *Cell culture.* Human 293T and RPE-1 (ATCC), PDX-derived PATC53 (PDX1),
558 PATC66 (PDX2), and mouse-derived PDAC cells KP$^{-/-}$C (internally registered as WY5549
559 and derived from *Ptf1aCre;LSL-Kras*$^{G12D/+}$*;LSL-Trp53*$^{L/L}$ mouse model) and KPC
560 (internally registered as N150F and derived from *Ptf1aCre;LSL-Kras*$^{G12D/+}$*;LSL-*
561 *Trp53*$^{R172H/R172H}$ mouse model, and named as N150F, see below "mouse strains were
562 cultured in Dulbecco modified Eagle medium (DMEM, Sigma) supplemented with 10%
563 fetal bovine serum (FBS, Gibco), 100IU/mL Penicillin (Gibco) and 100µg/mL
564 Streptomycin (Gibco).
565 *Lentiviral production.* Viral particles were produced using packaging plasmids
566 psPAX2 and pMD2.G. Briefly, 293T cells (ATCC) were seeded in 15cm diameter plate in
567 DMEM supplemented with 10% FBS (Gibco), 100IU/mL Penicillin (Gibco), 100µg/mL
568 Streptomycin (Gibco), 2 mM Glutamine (Gibco) and allowed to adhere. Transfection mix
569 was prepared by adding the vectors of interest in Opti-MEM (Gibco) in presence of
570 Polyethyleneimine (PEI). Supernatant was collected 72 hours after transfection, filtered
571 through 0.45µm low-protein binding filters (Corning) and concentrated in sterile PBS
572 (Sigma Aldrich) after ultracentrifugation at 25,000 rpm for 2 hours. Concentrated virus
573 was freshly used to transduce target cells.
574 *Cell transduction with lentiviral particles.* Human and mouse cells were transduced
575 overnight with concentrated lentiviral particles (see Virus preparation) in the presence of
576 8 µg/mL polybrene. After 72 hrs from infection, the culture medium was replaced with a
577 fresh medium supplemented with antibiotic selection (G418 50 µg/mL or puromycin 1-5
578 µg/mL). Overexpression, down-regulation, or knockout of the targets were evaluated by
579 western blot after one week of antibiotic selection. For doxycycline-inducible shRNAs,
580 after one week of antibiotic selection, cells were pulsed with doxycycline hyclate
581 (Millipore-Sigma, D5207) 1 µg/mL at different time points, as indicated in figures and gene
582 expression was evaluated by western blot.
583 *Cell transfection.* Cells were seeded at 50% confluency in 10 cm diameter plate in
584 complete medium and allow to adhere overnight. Transfection mix was prepared by
585 adding the 10 µg of the indicated plasmids in 600 µL Opti-MEM (Gibco) in presence of 40
586 µL polyethyleneimine (PEI). Cells were then transfected for 8-12 hrs and protein
587 expression was evaluated using Western Blot.

588 *Generation of barcoded KPC (N150F) cell line.* KPC cells were infected
589 overnight with CloneTracker™ XP Lentiviral Expressed Barcode Library (Cellecta)
590 in presence of polybrene (8μg/ml) (MOI < 0.1). After infection and puromycin
591 selection, cells were passaged for 10 generations before injection into NSG or
592 C57BL/6 mice.
593 *Cell proliferation and clonogenic assay.* Human and mouse cells were
594 seeded in a 96-well plate (500-1000 cells per well) in medium supplemented with
595 doxycycline 1 μg/mL or vehicle. After cell adhesion, cells were incubated at at 37°C
596 5%CO_2 in the IncuCyte (Essenbioscience) incubator. Cell confluency was
597 measured and analyzed over a period of 5-8 days using and medium was changed
598 every 48 hrs.
599 For clonogenic assay, 100-500 cells were seeded in a 6-well plate in
600 medium supplemented with doxycycline 1 μg/mL or vehicle and maintained at
601 37°C 5%CO_2 (medium was changed every 48 hrs). After 8-15 days, clones were
602 fixed and stained with crystal violet (0.25% crystal violet in methanol 20%).
603 Colonies with more than approximately 50 cells were counted manually and
604 clonogenic survival fraction was expressed as the relative plating efficiencies of
605 the irradiated cells to the control cells.
606 **Molecular Biology Experiments:**
607 *Short-hairpin RNAs (shRNAs) cloning.* For gene silencing, shRNAs from
608 Millipore-Sigma were cloned into the constitutive pLKO.1-TRC cloning vector
609 according to the manufacturer's protocol. These same shRNA sequences were
610 cloned into pENTR-THT and integrated into the inducible Tet-Puro backbones.
611 *Single-guide RNAs (sgRNAs) design and cloning.* sgRNAs were designed
612 with "GenScript CRISPR sgRNA Design Tool" (https://www.genscript.com/gRNA-
613 design-tool.html?a=post). First, 5`-phosphorilated oligos were annealed and
614 diluted 1:20. Then 1 μL of each annealed and diluted sgRNA was cloned in
615 digested lentiCRISPR-V2 according to Dr. Feng Zhang's protocol
616 (https://media.addgene.org/cms/files/Zhang_lab_LentiCRISPR_library_protocol.p
617 df). NEB® Stable Competent E. coli (C3040I) colonies resistant to ampicillin
618 antibiotic selection were amplified, and presence of sgRNA was confirmed by

619 Sanger sequencing. Positive clones were transfected individually in 293T cells along with
620 vectors for lentiviral packaging production. Human or mouse cells were infected by
621 lentiviral particles carrying a specific sgRNA and selected for puromycin resistance. Cut
622 efficiency of sgRNA was tested by T7 Endonuclease I (NEB #M0302L) assay on the DNA
623 of infected cells, according to the manufacturer's protocol
624 (https://www.neb.com/protocols/2014/08/11/determining-genome-targeting-efficiency-
625 using-t7-endonuclease-i). The sgRNA sequences for knocking out DPY30 are the
626 following: GAGCCAGAGCAGATGCTGGA (sgDPY30#1),
627 GGGACTTGCTGTGCTTGCAA (sgDPY30#2) for human and
628 GAGTCGGAGCAGATGCTGGA (sgDpy30) for mouse.
629 *Plasmids*. The following vectors were purchased from Addgene: psPAX2
630 (#12260), pMG2.D (#12259), lentiCRISPR-V2 (#52961), pLKO.1-TRC (#8453), pENTR-
631 THT (#55790), Tet-Puro (#21915), pLenti-PGK-Neo-PIP-FUCCI (#118616), emEGFP-
632 Mcm2 (mouse, #54163), emEGFP-Mcm3 (mouse, #54165), emEGFP-Mcm4 (mouse,
633 #54167), emEGFP-Mcm5 (mouse, #54169), emEGFP-Mcm6 (mouse, #54171),
634 emEGFP-Mcm7 (mouse, #54173), pcDNA3 Flag-hDPY30 (#15554), pcDNA3 Flag
635 WDR5 (#15552), pCMV-8xHis-Ub (#107392). The following vectors were purchased from
636 Genscript: pcDNA3.1 WDR5_L240K(+)-N-HA (L240K WDR5_OHu17370C), pcDNA3.1
637 WDR5_V268E(+)-N-HA (V268E WDR5_OHu17370C), pcDNA3.1 WDR5-(+)-N-HA
638 (WDR5_OHu17370C), pcDNA3.1(+)-C-HA-L69D-hDPY30 (L69D DPY30_OHu17211C),
639 pcDNA3.1(+)-C-HA-hDPY30 (DPY30_OHu17211C), pcDNA3.1(+)-C-HA-mdpy30
640 (Dpy30_OMu07274C), pcDNA3.1(+)-N-6His-hMCM2 (MCM2_OHu09867C),
641 pcDNA3.1(+)-N-6His-hMCM3 (MCM3_OHu107378C), pcDNA3.1(+)-N-6His-hMCM4
642 (MCM4_OHu11591C), pcDNA3.1(+)-N-6His-hMCM5 (MCM5_OHu02170C),
643 pcDNA3.1(+)-N-6His-hMCM6 (MCM6_OHu20108C), pcDNA3.1(+)-N-6His-hMCM7
644 (MCM7_OHu28012C). The following vectors were purchased from Sigma-Millipore:
645 shCTR (SHC002), shDPY30#1 (TRCN0000297810), shDPY30#2 (TRCN0000280267),
646 shWDR5#1 (TRCN0000118047), shWDR5#2 (TRCN0000118049), shRBBP5#1
647 (TRCN0000165777), shRBBP5#2 (TRCN0000165100), shASH2L#1
648 (TRCN0000019274), shASH2L#2 (TRCN0000019276), shDpy30#1
649 (TRCN0000034420), shDpy30#2 (TRCN0000034419).

650 *Protein extraction, Immunoprecipitation and Western Blot Analyses.* For
651 cellular protein lysates, cells were scraped on ice using cold Ripa lysis buffer (150
652 nM NaCl, 50 mM Tris HCl pH 8, 1% Igepal, 0.5% sodium deoxycholate, 0.1% SDS
653 - Boston BioProducts, BP-115) supplemented with a HALT protease and
654 phosphatase inhibitor cocktail (ThermoFisher). Cell lysates centrifuged at 13,200
655 rpm for 20 min at 4°C and supernatants were collected.
656 For immunoprecipitates (IPs), cells were scraped using NP40 buffer (10 mM
657 NaCl, 10 mM Tris HCl pH 7.5, 0.5% Nonidet P-40 - Boston BioProducts, BP-119)
658 supplemented with a HALT protease and phosphatase inhibitor cocktail (#78440,
659 ThermoFisher Scientific). Cell lysates were sonicated twice at 30% amplitude for
660 15 sec on ice and centrifuged at 13,200 rpm for 20 min at 4°C and supernatants
661 were collected. Immunoprecipitation was performed by binding the primary
662 antibody to protein G magnetic beads (Dynabeads, ThermoFisher Scientific,
663 10004D) for 30-60 min at RT. Bs3 (A39266, ThermoFisher Scientific) was used to
664 crosslink primary antibodies to protein G. Cell lysates were diluted with PBS-T
665 buffer (PBS-0.1% Tween20) supplemented with protease/phosphatase inhibitor,
666 added to antibody-bead complexes and incubated overnight at 4°C. IPs were then
667 washed in PBS-T buffer, resuspended in 4X NuPage Sample Buffer
668 (Invitrogen) supplemented with 1% β-mercaptoethanol.
669 IPs and proteins were separated in 4-20% SDS-PAGE (Criterion Precast
670 Midi Gel, Bio-Rad) and transferred to nitrocellulose membranes (Trans-Blot Turbo
671 Midi 0.2 µm nitrocellulose transfer pack, Bio-Rad). Membranes were blocked with
672 5% non-fat dried milk in PBS-T and incubated at 4°C overnight with primary
673 antibodies.
674 Membranes were washed in PBS-T and incubated 1 hour at RT with the
675 appropriate horseradish peroxidase-conjugated secondary antibodies (Cell
676 Signaling Technology) for ECL detection (SuperSignal™ WEST Pico PLUS
677 Chemiluminescent Substrate, ThermoFisher) or with the appropriate IRDye
678 800CW or IRDye 680RD Dye-Labeled secondary antibodies (LICORbio). Band
679 quantification was performed using the QuantiONE software (Bio-Rad

680 Laboratories). The Re-Blot Plus Strong Solution (#2404, EMD Millipore) was used to strip
681 the membranes, when reblotting was needed.

682 *Purification of proteins on newly synthesized DNA (iPOND)*. iPOND was performed
683 essentially as described previously (86). Briefly, 293T or KPC cells were seeded in a
684 square at 70% confluency (one square per each iPOND sample). Cells were pulsed with
685 10 μM EdU (5-Ethynyl-2'-deoxyuridine, Millipore-Sigma, #900584), for 5 and 10 min to
686 enable the detection of protein bound to active DNA replication forks. For each
687 experiment, two negative controls were included: one sample was not pulsed with EdU
688 and one sample was pulsed with EdU followed by 60 min thymidine chase. All samples
689 were fixed with 1% formaldehyde (ThermoFisher Scientific) for 20 min at RT, and
690 quenched using 125 mM Glycine (Millipore-Sigma) solution for 5 min at RT. After fixation,
691 samples were collected in 50-ml tube and washed (once with PBS+1% BSA and once
692 with PBS). Samples were permeabilized using PBS+0.1% Tryton-X100 for 10 min in
693 gentle shaking at RT and transferred in a 15-ml tube. Copper(ii) Sulfate (Millipore, Sigma
694 #451657), (+)-sodium L-ascorbate (Millipore, Sigma #A7631) and Biotin Azide (Click
695 chemistry tools, Fisher) were used to perform the Click-reaction for biotin-conjugate the
696 incorporated EdU. After washing steps, cell pellets were resuspended in SDS 1% for
697 protein extraction and sonicated 3 times at 30% amplitude for 30 sec on ice. After
698 centrifugation, cleared lysates were diluted 1:2 with PBS and % 1% of protein lysate was
699 kept as input control. Cleared lysates were then incubated with Pierce™ Streptavidin
700 Magnetic Beads (ThermoFisher Scientific, 88817) for 2 hr at RT in gentle shaking. Protein
701 complexes were washed three time with PBS-T and purified proteins were resuspended
702 in 4X NuPage Sample Buffer (Invitrogen) supplemented with 1% β-mercaptoethanol.

703 *In vitro immunofluorescent staining.* Cells were plated at 50% of confluency over
704 a round glass coverslip (Chemglass Life Sciences, cat. n. CLS1763012), allowed to
705 adhere overnight, treated with doxycycline as appropriate to induce gene silencing and
706 fixed using 4% paraformaldehyde for 15 min at RT. Cells were then washed twice in PBS
707 and permeabilized (0.1% triton X100 in PBS) for 15 min at RT. After a second round of
708 washes in PBS, cells were blocked using blocking buffer (3% BSA, 3% goat serum, 0.01%
709 triton X100 in PBS) 1h at RT. Primary antibodies were diluted in blocking buffer and
710 incubated overnight at 4°C. After washes, secondary antibodies (conjugated with Alexa-

711 488, Alexa-594, Alexa-647 or Alexa-750) were diluted in blocking buffer and
712 incubated 1h at RT. DAPI was used to counterstain nuclei. Images were captured
713 with a Hamamatsu C11440 digital camera, using a wide-field Nikon Ni-E
714 fluorescent microscope.

715 *Proximity Ligation Assay (PLA) and SIRF assay.* For PLA, Duolink® In Situ
716 Detection Reagents Red (Millipore-Sigma) were used and cells were stained
717 according to the manufacturer protocol. Briefly, cells were plated, fixed and
718 blocked as described above. After primary antibody incubation, cells were washed
719 with Buffer A and then the Duolink® In Situ PLA® probe anti-rabbit or anti-mouse
720 were added as appropriate. After ligation and amplification reactions, cells were
721 imaged using Zeiss LSM880 Airyscan confocal microscope (63X objective) at the
722 Advanced Microscopy Core (MD Anderson Cancer Center). SIRF assay was
723 performed essentially as described in (52, 53) with minor modifications. Cells were
724 plated on coverslips as described above and were pulsed with 20 μM BrdU for 5
725 min. The primary antibodies used were anti-WDR5 (rabbit), anti-DPY30 (rabbit,
726 Bethyl), anti-PCNA (rabbit) and anti-BrdU (mouse). Click-IT reaction was not
727 performed.

728 *DNA Fiber Assay.* Fiber stretching was performed essentially as described
729 in (87). Briefly, cells were double-pulsed precisely for 20 min with 25 μM CldU
730 (Chloro-2'-deoxyuridine (Millipore-Sigma, C6891) followed by 250 μM IdU (5-Iodio-
731 2'-deoxyuridine, Millipore-Sigma, I7125). Cells were harvested and diluted at
732 $2x10^5$cells/ml. A 3-μL drop of cell suspension was allowed to air-dry in a glass slide
733 and fiber spreading was carried out by adding 10 μL spreading buffer (0.5% SDS
734 in Tris-HCl EDTA). Fibers were fixed in Methanol/Acetic Acid 3:1 10 min, allowed
735 to completely dried and rinsed with deionized water. DNA was denatured with HCl
736 2N for 1.5 hr ar RT. After washing steps, slides were blocked in blocking buffer
737 (PBS 2% BSA, 2% goat serum, 0.1% Tween20) 1 hr at RT. CldU and IdU were
738 recognized by using the following primary antibodies: rat monoclonal anti-BrdU
739 clone BU1/75 and mouse monoclonal anti-BrdU clone B44. The antibodies were
740 diluted in blocking buffer and incubated 4 hr at RT, followed by secondary antibody
741 (goat anti-rat IgG (H+L) Alexa Fluor® 488, goat anti-mouse IgG (H+L) Alexa

742 Fluor® 594, ThermoFisher Scientific). Imaging was performed on the Leica SP8 laser
743 scanning confocal microscope at the Advanced Microscopy Core (MD Anderson Cancer
744 Center).

745 *Chromosome mis-segregation.* For the *in vitro* analysis, cells were plated at 50%
746 of confluency over a round glass coverslip (Chemglass Life Sciences, cat. n.
747 CLS1763012), allowed to adhere overnight and fixed using 4% paraformaldehyde for 10
748 min at RT. DNA was stained using DAPI 10 min at RT. Chromosome mis-segregation
749 were evaluated using a wide-field Nikon Ni-E fluorescent microscope (40X objective). For
750 *in vivo* analysis, H&E samples from human or mouse-derived tumors grown in recipient
751 mice were evaluated for anaphases with chromosome mis-segregation events using a
752 wide-field Nikon Ci-L plus light microscope (100X objective). Analyses was performed by
753 evaluating chromosome mis-segregation in H&E samples (5 mice per group, one section
754 per mouse), and for each mouse at least 20 anaphases were counted.

755 *Preparation of Metaphase Spreads.* Analysis of chromosomal aberrations was
756 performed at the Molecular Cytogenetics Facility (MD Anderson Cancer Center) as
757 previously described (32). Cells were incubated with Colcemid (KaryoMAX™,
758 ThermoFisher Scientific, #15212012) at 0.04 µg/mL for 3 hours, trypsinized, washed, and
759 spun down. Cells were incubated at RT for 15 minutes in hypotonic solution (0.075M KCl).
760 Cells were fixed by adding three times 2 mL of fixative solution (glacial MeOH + acetic
761 acid 3:1), followed by centrifugation. Cell suspension was dropped on glass slide. Slides
762 were allowed to air-dry, stained with 4% Giemsa staining solution (KaryoMAX™,
763 ThermoFisher Scientific, #10092013) for 5 min and mounted. At least 35 metaphases
764 were analyzed from each sample for chromosomal aberrations. Images were captured
765 using a Nikon 80i microscope equipped with karyotyping software from Applied Spectral
766 Imaging, Inc.

767 *Cell cycle synchronization and analysis by flowcytometry.* Human and mouse cells
768 were seeded in a 6-cm diameter plate ($1x10^5$ cells per plate) in complete medium and
769 allowed to adhere to plate for 16 hr. To synchronize cells in early S phase, a double
770 thymidine (Millipore-Sigma, T9250) pulse was used. Briefly, cells were cultured in
771 presence of 2 mM thymidine for 18 hrs, released in complete medium for 8 hrs and
772 arrested in S phase with a second thymidine-pulse for 18 hrs. Cells were then released

773 at different time point as indicated in figure using complete medium. To
774 synchronize cells in G2/M phase, cells were cultured in presence of 2 mM
775 thymidine for 18 hrs, released in complete medium for 8 hrs and arrested in G2/M
776 phase with 100 ng/ml Nocodazole (Millipore-Sigma, M1404) for 16 hrs. For DNA
777 content analyses cells were harvested at specific time point, resuspended in 250
778 µL of ice-cold PBS and fixed by adding 750 µL of absolute ethanol dropwise while
779 vortexing. Cells were kept an overnight in fixative solution, washed twice with PBS
780 and DNA stained using DAPI. Data were acquired using BD Celesta analyzer and
781 analyzed by FlowJo.

782 *BrdU incorporation assay and Re-replication analyses using flow cytometry.*
783 Human and mouse cells were seeded in a 6-cm diameter plate ($1x10^5$ cells per
784 plate) in complete medium and allowed to adhere to the plate for 16 hr. Cells were
785 pulsed with 15 µM BrdU for 2 hrs, harvested and fixed using APC or FITC BrdU kit
786 (#552598 or #559619 BD bioscienses) following manufacturer protocol.
787 Alternatively, human PDAC cells were fixed with ethanol as described above and
788 DNA was denaturated using 2N HCl solution for 20 min. Cells were then washed
789 three time with PBS, blocked in PBS 5% BSA and PE-conjugated anti-BrdU
790 antibody was incubated 1 hr at RT. After washing with PBS, nuclei were
791 counterstained using DAPI. Data were acquired using BD Celesta analyzer and
792 analyzed by FlowJo.

793 *Cell sorting.* Human cells were seeded in a 15-cm diameter plate at 70%
794 confluency in complete medium and allowed to adhere to the plate for 24 hr. Cells
795 were harvested and resuspended in FACS buffer (3% FBS, 1mM EDTA) and DAPI
796 was used as live/dead reagent. Cells were sorted using Influx Silver sorter and
797 data were analyzed by FlowJo.

798 *Immunophenotyping using flow cytometry.* After tumor dissociation and
799 single cells extraction (see Cell isolation from tumors), staining was performed
800 essentially as described in (88). Briefly, cell surface antigens were stained with the
801 appropriate primary antibodies for 20 minutes at 4°. For the staining of intracellular
802 proteins, samples were washed, fixed, permeabilized for 30 min at RT and
803 subsequently incubated with the appropriate primary antibodies for 1 hr at RT.

804 Dead cells were stained using the fixable viability violet dye Zombie Red (Invitrogen) for
805 10 min at RT followed by the blocking of Fc receptors with TruStain fcX (Biolegend) for
806 15 min at 4°C. Cells were analyzed on LSRFortessa X-20 flow cytometers (BD
807 Biosciences) and data were analyzed with FlowJo software version 10.8.2.

808 *Ex vivo stimulated cytokine secretion.* Single-cell suspensions from tumors were
809 resuspended in RPMI 1640 with 10% FCS, were added to anti-CD3 (clone 145-
810 2C11)/anti-CD28 (clone 37.51) antibody-coated (overnight at 10 µg/ml antibody) culture
811 plates for 4hr at 37°C in the presence of 1 µg/ml Golgiplug (BD Bioscience) and Monensin
812 (Biolegend) and processed for TNF and IFNγ intracellular cytokine staining.

813 *Histopathology, immunohistochemistry, and immunofluorescence.* Tumor
814 specimens were fixed overnight in 4% buffered paraformaldehyde, transferred to 70%
815 ethanol, and then embedded in paraffin using Leica ASP300S processor. For
816 histopathological analysis, tumors were sectioned (Leica RM2235, 5µm thickness) and
817 serial slides were collected. For every series one section was stained with hematoxylin
818 and eosin and remaining sections were kept for either immunofluorescence or
819 immunohistochemical analysis. For Alcian Blue (Vector Laboratories, H3501) and
820 Masson's Trichrome staining (VitroView™ Masson's Trichrome Stain Kit, VB-3016),
821 samples were processed according to the manufacturers' protocols.

822 Histological samples were processed as previously described (74). Briefly, after
823 cutting, baking, and deparaffinization, sections underwent antigen retrieval using Citra-
824 Plus Solution (BioGenex) according to specifications.

825 *For immunohistochemistry (IHC) staining*, endogenous peroxidases were
826 inactivated by 3% hydrogen peroxide and non-specific signals were blocked using 5%
827 BSA, 5% goat serum, and 0.1% Triton X-100. Primary antibodies were applied and
828 incubated overnight at 4°C. ImmPRESS HRP IgGs were used as secondary antibodies
829 and ImmPACT NovaRED® (Vector Laboratories, # SK-4805) was used for detection.
830 Images were captured with a Nikon DS-Fi1 digital camera using a wide-field Nikon Ci-L
831 plus light microscope.

832 Tissue Microarray slides of PDAC samples with available survival data (n=128)
833 collected at MD Anderson Cancer Center were stained for DPY30 as described above.
834 DPY30 nuclear expression was evaluate and categorized in blind as follow: Low (score

835 0=negative or score 1=weak), medium (score 2=moderate) and high (score
836 3=strong) expression. Kaplan-Meier survival curve was generated by clustering
837 PDAC patients according to DPY30 expression and log-rank test was used to
838 compare the survival difference among different groups.

839 *For immunofluorescence staining*, secondary antibodies conjugated with
840 Alexa-488, Alexa-594, Alexa-647 or Alexa-750 were used. DAPI nuclear staining
841 (#40043, Biotium) was used to counterstain nuclei. Images were captured with a
842 Hamamatsu C11440 digital camera, using a wide-field Nikon Ni-E fluorescent
843 microscope or Vectra Polaris (Akoya Biosciences).

844 *Cyclic immunofluorescence.* After the first staining and image acquisition
845 using PE Vectra polaris, coverslips were removed by incubating slides with 37°C
846 PBS for 20 min. Slides were then incubated with stripping buffer (62.5 mM Tris
847 Base / Tris-HCl, 2% Sodium Dodecyl Sulfate, 0.8% Beta ME, 55°C, 30 min), and
848 then stained with another round of antibodies. Slides were washed with PBS 0.1%
849 Triton-X100 between each step. DAPI nuclear staining (#40043, Biotium) was
850 used every cycle.

851 *Antibodies.* Primary antibodies purchased from Cell Signaling Technology:
852 anti-WDR5 (clone D9E1I, #13105), anti-Cleaved Caspase-3 (Asp175, #9661),
853 anti-STING (clone D2P2F, #13647), anti-STING (S365) (clone D1C4T, #62912),
854 anti-ASH2L (clone D93F6, #5019), anti-RbBP5 (#8037), anti-MCM2 (S139) (clone
855 D1Z8X, #12958), anti-MCM2 (clone D7G11, #3619), anti-MCM3 (#4012), anti-
856 MCM4 (clone D3H6N, #12973), Rabbit monoclonal anti-MCM7 (clone D10A11,
857 #3735), anti-Histone H3 (pS10) (#9701), anti-Cdc6 (clone C42F7, #3387), anti-
858 H3K4Me3 (clone C42D8, #9751), anti-His Tag (clone 27E8, #2366). Primary
859 antibodies purchased from Millipore-Sigma: anti-DPY30 (#HPA043761), anti-
860 γH2AX (pS139) (clone JBW301, #05-636), anti-beta-Actin (clone AC-74, #A5316).
861 Primary antibodies purchased from Bethyl Laboratories: anti-DPY30 (#A304-
862 296A), anti-MCM5 (#A300-195A), anti-MCM6 (#A300-194A), anti-WDHD1
863 (#A301-140A), anti-RPA2 (pS4-8) (#A300-245A). Primary antibodies purchased
864 from Santa Cruz Biotechnology: anti-WDR5 (clone G-9, #sc-393080), anti-Cyclin
865 E (clone HE12, #sc-247), anti-Histone H3 (clone 1G1, #sc-517576), anti-Geminin

866 (clone FL-209, #sc-13015), anti-Luciferase (clone C-12, #sc-74548). Primary antibodies
867 purchased from Abcam: anti-BrdU (clone BU1/75 – ICR1, #ab6326), anti-H3K4Me1
868 (#ab8895), anti-H3K4Me3 (#ab8580), anti-H3K4Ac (#ab4729), Alexa Fluor® 594 anti-
869 αSMA (clone 1A4, #ab202368), Alexa Fluor® 488 anti-αSMA (clone 1A4, #ab184675).
870 Primary antibodies purchased from ThermoFisher Scientific: anti-PCNA (#PA5-16797),
871 anti-Cyclin A2 (clone E23.1, #MA1-154), anti-GFP (clone GF28R, #MA5-15256), anti-
872 Ki67 (#MA5-14520), anti-HA tag (clone 2-2.2.14, #26183), anti-CD8a (clone 4SM15, #14-
873 0808-82), PE-conjugated anti-BrdU (clone BU20A, #12-5071-42). Other primary
874 antibodies: anti-BrdU (clone B44, #347580, BD Laboratories), anti-Cdc6 (pS54) (#102-
875 15286, RayBiotech), anti-Ki67 (#14965-1-AP, Proteintech), anti-Flag tag (clone OTI4C5,
876 #TA50011-100, OriGene Technologies), anti-CD3 (#A045201-2, Agilent Technology),
877 Rabbit gamma globulin (#31887, Invitrogen). Antibodies purchased from Biolegend: anti-
878 mouse Ki67 (clone 16A8, #652402), BV 510 anti-mouse CD8a (clone 53-6.7, #100751),
879 PE anti-CD279 (PD-1) (clone RMP1-30, #109104), PB anti-Granzyme B (clone GB11,
880 #515408), PE-Cy5 anti-CD3 (clone 17A2, #100274), Pe-Cy-7 anti-Foxp3 (clone FJK-16S,
881 #25-5773-82), APC-Cy7 anti-CD4 (clone GK1.5, #100414), Alexa Fluor® 700 anti-CD45
882 (clone 30-F11, #103128), PerCP-Cy5.5 anti-Thy1.2 30-H12 (clone 30.H12, #105338),
883 BV785 anti-NK1.1 (clone PK136, #108749), Alexa Fluor® 647 anti-Tnf (clone MP6-XT22,
884 #506314), Alexa Fluor® 700 anti-Infγ (clone XMGG1.2, #505824). Secondary antibodies
885 purchased from Vector Laboratories: ImmPRESS® HRP goat anti-rabbit IgG (#MP-
886 7451), ImmPRESS® HRP goat anti-mouse IgG (#MP-7451). Secondary antibodies
887 purchased from ThermoFisher Scientific: Goat anti-rabbit IgG (H+L) Alexa Fluor® 488
888 (#A-11008), Goat anti-rabbit IgG (H+L) Alexa Fluor® 594 (#A-11012), Goat anti-rabbit
889 IgG (H+L) Alexa Fluor® 647 (#A-21244), Goat anti-rabbit IgG (H+L) Alexa Fluor® 750
890 (#A-21039), Goat anti-mouse IgG (H+L) Alexa Fluor® 488 (#A-11001), Goat anti-mouse
891 IgG (H+L) Alexa Fluor® 594 (#A-11005), Goat anti-mouse IgG (H+L) Alexa Fluor®
892 647(#A-21235), Goat anti-rat IgG (H+L) Alexa Fluor® 488 (#A-11006), Goat anti-rat IgG
893 (H+L) Alexa Fluor® 647 (#-21247).

894 *RNA extraction.* RNA extraction was achieved using Qiagen RNeasy Micro kit
895 following manufacturer's instruction. Briefly, RNA extraction was performed from KPC and
896 $KP^{-/-}C$ cells or tumors stably knocked out for Dpy30 or control and from PATC53 stably

897 expressing doxycycline-inducible scramble control (shCTR) or shRNAs targeting
898 WDR5 or DPY30 pulsed for 48 hrs with doxycycline. Cells grown *in vitro* were
899 scraped using 350 µL of RLT buffer supplemented with β-mercaptoethanol. For
900 RNA extraction from tumors, tissue specimens (approximately 2x2mm) were snap-
901 frozen and kept at -80°C until further processing. Tumors were then weighted and
902 dissociated in RLT buffer supplemented with β-mercaptoethanol using
903 gentleMAX™ M tubes (Miltenyi Biotec) and RNA_02 program. DNA digestion was
904 performed by adding recombinant DNAse I (Millipore-Sigma, #4536282001). to
905 purification column. Total RNA was eluted in RNAse-free water, quantified, and
906 submitted for sequencing.

907 *Genomic DNA extraction.* DNA extraction was achieved using Qiagen
908 DNaeasy Blood and Tissue kit following manufacturer's instruction. Briefly, cells
909 grown *in vitro* were harvested and cell pellets were snap-frozen and kept at -80°C.
910 For DNA extraction from tumors, tissue specimens (approximately 2x2mm) were
911 weighted and dissociated by mechanical digestion in 180 µL Buffer ATL
912 supplemented with 20 µL proteinase K stock solution. Total DNA was eluted in
913 DNAse-free water, quantified, and submitted for sequencing.

914 *Chromatin immunoprecipitation (ChIP).* ChIP was performed essentially as
915 described in (89) with optimized DNA shearing condition and few modifications.
916 Briefly, $9x10^6$ PATC53 cells stably expressing doxycycline-inducible shRNAs
917 against DPY30, WDR5 or scramble control were seeded in a 15-cm diameter plate
918 in complete medium in the presence or not of 1 µg/ml doxycycline for 48 hrs. Cells
919 were then harvested, resuspended in 3 mL of complete medium, cross-linked with
920 200µL of 16% formaldehyde for 10 min at 37°C in gentle stirring and quenched
921 with 200 µL Glycine 2M for 5 min at 37°C in gentle stirring. Tissue lysis, sonication
922 and chromatin immunoprecipitation were performed as described in (31, 74).

923 *ATAC-seq.* Cells were processed as described in (74). Briefly, 100,000
924 human PATC53 cells were lysed in lysis buffer for 5 minutes on ice. Tn5
925 tagmentation was carried out for 30 minutes at 37 °C. After indexing and PCR
926 amplification, DNA libraries were multiplexed and sequenced on HiSeq X with
927 150nt PE configuration.

928 *Immuno-precipitate mass spectrometry.* KPC, PATC53 and PATC66 cells were
929 seeded in 15cm diameter plate at 50% confluency in complete medium. Cells were
930 scraped in RIPA buffer as described above after 24 hr from cell seeding. For each sample,
931 2 mg of lysate were immunoprecipitated for DPY30 or control IgG and immunocomplexes
932 were resuspend in 100μL of NuPage sample buffer, and 20μL were resolved using SDS-
933 PAGE for quality control. For proteomics, 40μL of each sample were processed by SDS-
934 PAGE using 10% Bis-Tris NuPage Mini-gel (Invitrogen) with the MES buffer system. The
935 gel was run 1cm and the mobility region excised into 10 equally sized bands. Each band
936 was processed by in-gel digestion with trypsin using a robot (ProGest, DigiLab) with the
937 following protocol: i) washed with 25mM ammonium bicarbonate followed by acetonitrile,
938 ii) reduced with 10mM dithiothreitol at 60°C followed by alkylation with 50mM
939 iodoacetamide at RT, iii) digested with sequencing grade trypsin (Promega) at 37°C for
940 4h, iv) quenched with formic acid and the supernatant was analyzed directly without
941 further processing. For mass spectrometry, half of each digested sample was analyzed
942 by nano LC-MS/MS with a Waters M-Class HPLC system interfaced to a ThermoFisher
943 Fusion Lumos mass spectrometer. Peptides were loaded on a trapping column and eluted
944 over a 75μm analytical column at 350nL/min; both columns were packed with Luna C18
945 resin (Phenomenex). The mass spectrometer was operated in data-dependent mode,
946 with the Orbitrap operating at 60,000 FWHM and 15,000 FWHM for MS and MS/MS
947 respectively. The instrument was run with a 3s cycle for MS and MS/MS. 5hrs of
948 instrument time was used for the analysis of each sample.
949 Quantitative real time PCR. RNA from cells was extracted using RNeasy Mini kit
950 (Qiagen, #74104). Total RNA was quantified using the Nanodrop Spectrophotometer
951 (ThermoFisher). The synthesis of cDNA was performed using the SuperScript VILO
952 Master Mix (ThermoFisher) in an PCR Thermocycler (Bio-Rad). cDNAs were amplified
953 using PowerUp™ SYBR™ Green Master Mix (Invitrogen, A25742) and Real-time PCR
954 Detection System (Applied Biosystems). Normalization of the data was performed using
955 housekeeping genes (*ACTB, GAPDH, 18S*). The following primers (Sigma) were used (5'
956 – 3'): RFC3 Forward TTCGTGGAAGGCTGTATGAGC, RFC3 Reverse
957 CCTCCCCTTTCAGTTGTCCAT; *GINS2* Forward CAATGCCCAGCCCTTACTACA,
958 *GINS2* Reverse GCCTTCGGGATGTTGTCTGA; *FEN1* Forward

959 GTTCCTGATTGCTGTTCGCC, *FEN1* Reverse ATGCGAATGGTGCGGTAGAA;
960 *IFNL1* Forward GGAGGCATCTGTCACCTTCAA, *IFNL1* Reverse
961 GGACTCAGGGTGGGTTGAC; *IRF-AS1* Forward CACCGCGTCTGTGTCTGTA,
962 *IRF-AS1* Reverse GCCACCTACGATATACCACCC; *TRIM10* Forward
963 TGGCTAACGTGGTGGAGAAC, *TRIM10 Reverse*
964 *TGCTCTTGGCAGACATCCTC; ACTB* Forward CCAGAGGCGTACAGGGATAG,
965 *ACTB* Reverse CCAACCGCGAGAAGATGA; *18S* Forward
966 CTCAACACGGGAAACCTCAC, *18S* Reverse CGCTCCACCAACTAAGAACG;
967 *GAPDH* Forward GAAGGTGAAGGTCGGAGTC, *GAPDH* Reverse
968 GAAGATGGTGATGGGATTTC.

969 *NGS library production for barcode detection in bulk tumors.* Frozen tumors
970 were minced and suspended in Buffer P1 (Qiagen, 1 mL buffer per 100 mg tumor)
971 and a scale for cell number quantification was added. This mixture was
972 homogenized in a gentleMACS homogenzier (Miltenyi Biotec). After
973 homogenization, the samples were transferred into 15 mL polypropylene tubes
974 (Falcon) and RNase A (100 µg/mL) was added (10 µL per 100 mg tumor). After 10
975 minutes, 10% SDS (Promega) and Proteinase K (Qiagen) were added (both 50 µL
976 per 100 mg tumor) and incubated at 56°C for 20 minutes. The DNA was then
977 sheared by passing the lysate through a 23G syringe needle 10 times. The lysates
978 were transferred into 1 mL polypropylene tubes and DNA was purified using
979 Phenol:Chloroform:Isoamyl alcohol (25:14:1 pH 8.0, Sigma Aldrich) and
980 Chloroform:Isoamyl alcohol (24:1, Sigma Aldrich). The aqueous DNA was
981 precipitated by adding 3M sodium acetate (Sigma Aldrich, 90uL per 1 mL sample)
982 and isopropanol (Fisher Scientific, 720 µL per 1 mL sample). DNA was centrifuged
983 at 14,000 rpm for 20 minutes at 4°C and washed with 70% ethanol (Fisher
984 Scientific). Once dried, the DNA pellets were dissolved in Ultrapure distilled water
985 (Thermo Fisher Scientific) and DNA concentration was quantified using NanoDrop
986 2000 (Thermo Fisher Scientific).

987 Barcodes were amplified through 2 rounds of PCR on the DNA samples
988 using Titanium Taq DNA polymerase (Clontech, Takara). The first PCR was
989 performed using the following protocol: 3 minutes at 94°C followed by 16 cycles of

990 30 seconds 94°C, 10 seconds 60°C, and 20 seconds 68°C, followed by final extension at
991 72°C for 2 minutes then hold at 4°C. The sequences of the primers used are:
992 XPg_1stF (5'-ACCGAACGCAACGCACGCA-3')

993 XPg_1stR (5'-ACGACCACGACCGACCCGAACCACGA-3').
994 A second PCR was performed on the PCR product using the following protocol: 3
995 minutes at 94°C followed by 12 cycles of 30 seconds 94°C, 10 seconds 66°C, and 10
996 seconds 72°C, followed by final extension at 72°C for 2 minutes then hold at 4°C. The
997 sequences of the primers used are:
998 P7_XPg_2ndF (5'-
999 AGCAGAAGACGGCATACGAGATAGCACCGAACGCAACGCACGCA -3')
1000 unique index reverse primer P5_XPg_2ndR (5'-
1001 AGATACGGCGACCACCGAGATCTACACGCACGACGAGACGCAGACGAAXXXXXXA
1002 CGACGACCGACCCGAACCACGA-3', X bases refers to index barcode sequence).
1003 Second PCR products were then identified through agarose gel electrophoresis
1004 (2.5%, Lonza) at expected size of 227 bp and extracted using PureLink Quick Gel
1005 Extraction Kit (Thermo Fisher Scientific). The purified PCR product was quantified using
1006 High Sensitivity D1000 ScreenTape and Agilent 4200 TapeStation System (Agilent
1007 Technologies). Barcode representation was measured by NGS using Illumina HiSeq2000
1008 with Seq_XPg_BC30 (5'- AGACGACCTGCTCCAGCTGCACCA-3') as read 1
1009 sequencing primer and RSeq-IND-XP NGS (5'- ACACGCACGACGAGACGCAGACGAA
1010 -3') as i5 index primer.
1011 *Quantitative Scale.* A known quantity of barcoded cells was used as normalization
1012 scale as previously described (67). In brief, the barcoded cells are infected with the same
1013 lentivirus that carries a unique barcode that are not shared in the lineage tracing library
1014 with a low Multiplicity of Infection (MOI < 0.1). Resulting infected cells are then selected
1015 by puromycin and expanded for preparing the spike-in mixture with following cells:
1016 50 cells carrying the bc14-001.bc30-100002 barcode
1017 (CCAAAGATAGATCATGGTACACCATGACACGTCACATGTGTGCAGTCA);
1018 500 cells carrying the bc14-001.bc30-100003 barcode
1019 (CCAAAGATAGATCATGGTACTGACACTGCAGTACCACATGCACACAAC);

1020 5,000 cells carrying the bc14-001.bc30-100001 barcode
1021 (CCAAAGATAGATCATGGTCATGGTACACACGTGTCAACTGACCACAAC);
1022 50,000 cells carrying the bc14-001.bc30-100004 barcode
1023 (CCAAAGATAGATCATGGTTGACACACACTGACTGACTGACTGACACCA);
1024 500,000 cells carrying the bc14-001.bc30-100005 barcode
1025 (CCAAAGATAGATCATGGTGTACACGTACGTACTGACCAACTGACGTCA).
1026 During the tissue and cell dissociation step of barcode library preparation,
1027 the cell mixtures were added and served as a reference for spike-in normalization
1028 of the sequencing reads. After normalizing read counts of each library by the size
1029 factor (DNA content) and library size, a high correlation coefficient (r=0.96) was
1030 observed between normalized read counts and cell number in log scale. This
1031 calibration curve was then used to predict cell count of each barcode in tumors.
1032 ***In vivo* Experiments**
1033 *Mouse strains.* Conditional *Ptf1a*Cre;*LSL-Trp53*$^{fl/+}$ and *LSL-Kras*$^{G12D/+}$
1034 strains were interbred to obtain *Ptf1a*Cre;*LSL-Kras*$^{G12D/+}$;*LSL-Trp53*$^{fl/fl}$;double
1035 mutant animals (hereafter KP$^{-/-}$C mouse model) and kept in a C57BL/6 background
1036 (47). Conditional *Ptf1a*Cre; *LSL-Kras*$^{G12D/+}$ (obtained from Dr. Haoquang Ying,
1037 UTMDACC) and (46) *LSL-Trp53*$^{R172H/+}$ (obtained by Dr. Guillermina Lozano,
1038 UTMDACC) strains were interbred to obtain *Ptf1a*Cre;*LSL-Kras*$^{G12D/+}$;*LSL-*
1039 *Trp53*$^{R172H/+}$;double mutant animals (hereafter KPC mouse model) and kept in pure
1040 C57BL/6 background. Nude, NSG and C57BL/6 female mice (6 weeks old) were
1041 purchased from Experimental Radiation Oncology at MD Anderson Cancer
1042 Center. For treatment with anti-CD8 and anti-PD1 monoclonal antibodies,
1043 C57BL/6J female mice (6 weeks old) were purchased from Jackson Laboratory.
1044 All animal studies and procedures were approved by the UTMDACC Institutional
1045 Animal Care and Use Committee. All experiments conformed to the relevant
1046 regulatory standards and were overseen by the institutional review board. No sex
1047 bias was introduced during the generation of experimental cohorts. Littermates of
1048 the same sex were assigned randomly to experimental arms.
1049 *Pancreas orthotopic injections and surgical procedures.* C57BL/6 female
1050 mice (8 weeks old) were shaved and anesthetized using isoflurane (Henry Schein

1051 Animal Health). Analgesia was achieved with buprenorphine SR (0.1 mg/Kg BID) (Par
1052 Parmaceutical) *via* subcutaneous injection, and shaved skin was disinfected with
1053 Chlorhexidine and 70% ethanol. A 0.5-cm incision was performed on the left flank through
1054 the skin/subcutaneous and muscular/peritoneal layers. Pancreas was exposed, and 20
1055 μL of cell resuspension (total $1x10^5$ KPC or $KP^{-/-}C$ cells per mouse) were injected using a
1056 27 Gauge Hamilton syringe. Hemostasis was controlled with a bipolar cautery (Bioseb) if
1057 needed. The pancreas was carefully repositioned into the abdominal cavity, and
1058 muscular/peritoneal planes were sutured individually by absorbable sutures. The
1059 skin/subcutaneous planes were closed using metal clips. Mice were monitored daily for
1060 the first three days, and twice/week thereafter for signs of tumor growth by manual
1061 palpation or MRI when appropriate.

1062 *Subcutaneous transplantation, tumor volume measurement and survival study*.
1063 Tumor single cell suspension was resuspended in DMEM without phenol Red (Sigma)
1064 and Matrigel (BD Biosciences, 356231) (1:1 dilution) at a density of $1x10^5$ cells/100μL for
1065 KPC and KP-/-C cells and $1x10^6$ cells/100μL for PATC53 and PATC66 cells. Cell
1066 suspensions were injected subcutaneously into the flank of 8-week-old NSG, nude or
1067 C57BL/6 female mice as indicated in figures. Mice were monitored every 5 days, and
1068 tumor measurements was calculated according to the formula: Tumor volume (mm^3) =
1069 (W^2xL)/2, where W is Width and L is length.

1070 Mice that underwent orthotopic cell transplantation were monitored over time for
1071 tumor development by magnetic resonance imaging and survival annotated.

1072 *Treatments*. The following antibodies were purchased from Bio X cell: InVivoMab
1073 anti-mouse PD-1 (CD279) (clone 29F.1A12, # BE0273), InVivoMab anti-mouse CD8
1074 (clone YTS 169.2, # BP0117) and InVivoMab rat IgG2a isotype control (clone 2A3, #
1075 BE0089). Treatments with monoclonal antibody against PD-1 or CD8 or control were
1076 started 7 days after KPC cell subcutaneous injection in C57BL/6 mice. Monoclonal
1077 antibodies were diluted in PBS to a final concentration of 200μg/100μL and 50μg/100μL
1078 respectively for anti-PD-1 and anti-CD8. The treatments were performed by
1079 intraperitoneal injection of 100μL of antibody per 25g mouse, three times a week for two
1080 consecutive weeks.

1081 *Euthanasia, necropsy, and tissues collection*. Mice were euthanized by
1082 exposure to CO_2 followed by cervical dislocation. A necropsy form was filled in with
1083 mouse information, tumor size and weight, infiltrated organ annotations, and
1084 metastasis number and location.

1085 *Non-invasive MRI imaging.* A 7T Bruker Biospec (BrukerBioSpin), equipped
1086 with 35mm inner diameter volume coil and 12cm inner-diameter gradients, was
1087 used for MRI imaging. A fast acquisition with relaxation enhancement sequence
1088 with 2,000/39 ms TR/TE, 256x192 matrix size, r156uM resolution, 0.75mm slice
1089 thickness, 0.25mm slice gap, 40x30cm FOV, 101kHz bandwidth, and 4 NEX was
1090 used for acquired in coronal and axial geometries a multi-slice T2-weighted
1091 images. To reduce respiratory motion, the axial scan sequences were respiratory
1092 gated. All animal imaging, preparation, and maintenance was carried out in
1093 accordance with MD Anderson's Institutional Animal Care and Use Committee
1094 policies and procedures.

1095 *Cell Isolation from tumors.* Tumors from mouse xenografts were harvested
1096 in HBSS (Gibco) and kept on ice. Isolation of pancreatic tumor cells was performed
1097 by mechanical dissociation (mincing the tumor tissue with sterile scissors) and
1098 enzymatic digestion 1 hr at 37°C in in gentle rotation (Dispase II 1 mg/ml,
1099 Collagenase IV 2 mg/ml in DMEM high glucose supplemented with 1% FBS). The
1100 single-cell populations were seeded at in DMEM high glucose (Gibco)
1101 supplemented with 10% FBS (Gibco), 100 IU/ml penicillin (Gibco), and 100 µg/ml
1102 streptomycin (Gibco). In order to get rid of the murine fibroblasts in the culture, we
1103 performed brief trypsinization cycle (0.25% Trypsin-EDTA, Gibco). For single-cell
1104 RNA and flow-cytometry analyses, tumors from KPC cells were minced into small
1105 fragments and digested with 1.5 mg/mL collagenase IV and 50 U/mL DNase I for
1106 30min at 37°C under agitation. For flow cytometry analysis, the lymph nodes were
1107 collected and passed through 40 µm cell strainers and used for compensation.

1108 ***In Silico* Analyses**

1109 *Analysis of the TCGA dataset.* For TCGA GSEA analysis, the TCGA
1110 pancreatic adenocarcinoma mRNA dataset is downloaded from Broad GDAC
1111 website (http://firebrowse.org/?cohort=PAAD&download_dialog=true). The mRNA

1112 data from the Illumina Genome Analyzer platform in the website was used here
1113 (PAAD.rnaseqv2__illuminahiseq_rnaseqv2__unc_edu__Level_3__RSEM_genes
1114 _normalized__data.data.txt). There was a total of 179 tumor samples and 4 normal
1115 adjacent tissues with their mRNA available. The clinical survival profile of 179 samples
1116 was downloaded from cbio-portal website (http://www.cbioportal.org). The tumor purity
1117 of 179 TCGA RNA samples was computed by the ABSOLUTE developed by Broad
1118 Institute. Only those sample with purity above 50 percent were selected. These 70 high-
1119 purity tumor samples were classified into high and low abundant groups for survival
1120 analysis through applying median value as the cut off. Survival was analyzed according
1121 to the Kaplan-Meier method, and differences in their distribution were evaluated by
1122 means of the log-rank test.

1123 *Analysis of the PRINCE dataset (70).* Median DPY30 mRNA expression from
1124 metastatic sites was used to segregate patient into high- or low-DPY30 expression and
1125 generate progression-free and overall survival Kaplan-Meier plots.

1126 *Automatic image segmentation and quantification.* Fluorescence quantification
1127 was done using MATLAB (The MathWorks, Inc.). Specifically, Otsu's thresholding method
1128 and marker-controlled watershed algorithm was used to segment and specify nuclear
1129 regions of individual cells. Expression of each marker in the individual segmented area
1130 was then quantified by pixel intensity.

1131 *ChIP-Seq data analysis.* Samples were sequenced using NextSeq500 at
1132 UTMDACC Advanced Technology Genomics Core. Raw reads for each ChIP-seq were
1133 processed using Trimmomatic (v.0.39) (90) to trim off adaptor sequences incorporated in
1134 the read and to remove low quality bases, using the following parameters 'TRAILING:3
1135 LEADING:3 ILLUMINACLIP:adapters.fasta:2:30:10; SLIDINGWINDOW:4:15
1136 MINLEN:50'. Then, the resulting reads were mapped to the to human genome build
1137 GRCh38/hg38 using Bowtie2 v.2 (91) with the '–very-sensitive' preset of parameters.
1138 Reads that did not align to the nuclear genome or aligned to the mitochondrial genome
1139 were removed and duplicate reads were marked and removed using SAMtools (v.1.12)
1140 (92). Peak calling versus the corresponding input genomic DNA was performed using
1141 MACS2 (v.2.2.7.1) (93), for each sample separatly, with the '–nomodel', '–extsize 200', '–
1142 keep-dup all' and '–qvalue 0.05' flags and arguments. Peaks blacklisted by the ENCODE

1143 consortium analysis of artifactual signals in human cells (https://sites.
1144 google.com/site/anshulkundaje/projects/blacklists) were removed using bedtools (v.2.30)
1145 (94). To obtain a confidence peak set, only intersections between biological
1146 replicates were retained and shown as a heat map (generated using deepTools
1147 v.2.5.3) (95). Finally, differential binding analysis was performed using DiffBind
1148 (v.3.0) (96) with settings to use DESeq2 method, full library size and with
1149 subtraction of control input read counts. Binding events with an FDR cutoff of 0.05
1150 were defined as significantly different among experimental conditions. Mean
1151 normalized reads across the three replicates obtained from DiffBind analysis were
1152 used for scatter plot representation using the ggplot2 R package (97).

1153 *Proteomic data analysis.* Mass spectrometry data were searched using a
1154 local copy of Mascot (Matrix Science) with the following parameters: *enzyme:*
1155 Trypsin/P, *database:* SwissProt Human or Mouse (concatenated forward and
1156 reverse plus common contaminants), *fixed modifications:* Carbamidomethyl (C),
1157 *variable modifications:* Oxidation (M), Acetyl (N-term), Pyro-Glu (N-term Q),
1158 Deamidation (N,Q), *mass values:* Monoisotopic, *peptide Mass Tolerance:* 10 ppm,
1159 *fragment mass tolerance:* 0.02 Da, *Max Missed Cleavages:* 2. Mascot DAT files
1160 were parsed into Scaffold (Proteome Software) for validation, filtering and to create
1161 a non-redundant list per sample. Data were filtered using 1% protein and peptide
1162 FDR and requiring at least two unique peptides per protein.

1163 *ATAC-seq data analysis.* Paired-end ATAC-seq fragments of human cells
1164 were aligned to mouse reference build GRCh38/hg38 using Bowtie2 v.2. (91).
1165 Reads that did not align to the nuclear genome or aligned to the mitochondrial
1166 genome were removed and duplicate reads were marked and removed using
1167 SAMtools (92). Read positions were corrected for transposon insertion offset as
1168 described (98), then only uniquely mapped paired-end reads were kept for further
1169 analysis. All ATAC-seq peaks that were no more than 3 kb away from annotated
1170 gene TSS (GENCODE v19) were selected as promoter (proximal) regions, using
1171 annotatePeaks script from HOMER package (99).

1172 *Whole exome sequencing data analysis.* DNA sequencing of samples was
1173 performed on the Illumina HiSeq2000 sequencing platform at the UTMDACC

1174 Advanced Technology and Genomics Core. Sequencing fasta files were applied to
1175 FastQC (100) for quality control, adapters were trimmed by trimmomatic (90), and the
1176 genomic fragments were aligned to mm10 using bwa mem (101), then sorted and indexed
1177 by samtools (92). Following Base Quality Score Recalibration (BQSR) by GATK(102).
1178 Somatic mutations were called by Mutect2 and copy number segments were called by
1179 CNVkit (103).

1180 *RNA-Seq data analysis.* RNA sequencing of samples was performed on the
1181 Illumina NovaSeq6000 sequencing platform at the UTMDACC Advanced Technology and
1182 Genomics Core. FastQC v0.11.9 (https://github.com/s-andrews/FastQC) was used to
1183 perform quality control. Raw reads were first aligned to the human genome GRCh38.p14
1184 or mouse genome GRCm38.p6 using STAR2.7.10b v3.0.0 (104) and sorted using
1185 samtools v1.16 (92). Gene expression was quantified using Rsubread v2.14.2 (105).
1186 Differential expression analysis was performed using edgeR v3.42.4 (106) and limma
1187 v3.56.2 (107). Pathway enrichment analysis was performed using R package fgsea
1188 v1.26.0, clusterProfiler v4.8.2, msigdbr v7.5.1, ReactomePA v1.44.0 (108).

1189 *Single-cell RNA-Seq analysis.* Tumors deriving from KPC cells were digested and
1190 single cell suspension was diluted in 2% FBS in PBS for further processing. Chromium
1191 single-cell sequencing technology from 10x Genomics was used to perform single-cell
1192 separation, complementary DNA amplification and library construction following the
1193 manufacturer's guidelines. Briefly, the cellular suspensions were loaded on a 10x
1194 Chromium Single Cell Controller to generate single-cell gel bead-in-emulsions. The
1195 scRNA-seq libraries were constructed using the Chromium Single Cell 3' Library & Gel
1196 Bead Kit v.2 (PN-120237, 10x Genomics). The HS dsDNA Qubit Kit was used to
1197 determine the concentrations of both the cDNA and the libraries. The HS DNA
1198 Bioanalyzer was used for quality-tracking purposes and size determination for cDNA and
1199 lower-concentrated libraries. Sample libraries were normalized to 7.5 nM and equal
1200 volumes were added of each library for pooling. The concentration of the library pool was
1201 determined using the Library Quantification qPCR Kit (KAPA Biosystems) before
1202 sequencing. The barcoded library at the concentration of 275 pM was sequenced on the
1203 NovaSeq6000 (Illumina) S2 flow cell (100 cycle kit) using a 26 × 91 run format with 8 bp
1204 index (read 1). To minimize batch effects, the libraries were constructed using the same

1205 versions of reagent kits and following the same protocols, and the libraries were
1206 sequenced on the same NovaSeq6000 flow cell and analyzed together.
1207 The raw scRNA-seq data were pre-processed (demultiplex cellular
1208 barcodes, read alignment, and generation of gene count matrix) using Cell Ranger
1209 Single Cell Software Suite (v7.1.0,10x Genomics). Scrublet v0.2.3 (109), an
1210 algorithm to predict doublets in scRNA-seq data, was used to further clean
1211 doublets. Seurat (version 5.0.2) (110) was applied to the normalized gene-cell
1212 matrix to identify highly variable genes (HVGs) for unsupervised cell clustering.
1213 Principal component analysis (PCA) was performed on the top 2000 HVGs. The
1214 FindNeighbors function of Seurat was used to construct the Shared Nearest
1215 Neighbor (SNN) Graph, based on unsupervised clustering performed with Seurat
1216 function FindClusters and top 60 PCs. Different resolution parameters for
1217 unsupervised clustering were then examined, and cluster marker genes were
1218 checked to determine the optimal number of clusters with distinct transcriptional
1219 profiles. For visualization, the dimensionality was further reduced using Uniform
1220 Manifold Approximation and Projection (UMAP) method (111) with Seurat function
1221 RunUMAP. The PCs used to calculate the embedding were the same as those
1222 used for clustering. Differentially expressed genes (DEGs) were identified for each
1223 cluster using the FindMarkers function in Seurat (110). The top-ranked DEGs and
1224 the enrichment of canonical marker genes were integrated, together with global
1225 cluster distribution and prior knowledge to infer major cell types and cellular states.
1226 *Re-replication sequencing.* Briefly, $30x10^6$ control or Dpy30-KO KPC cells
1227 were seeded in a square bioassay dish (Corning®) and were synchronized in S
1228 phase using a double thymidine block ad described above. After synchronization,
1229 cells were released in complete medium supplemented with 25 μM CldU for 45
1230 minutes. Cells were then washed twice with PBS and a second pulse in complete
1231 medium supplemented with 250 μM IdU was added and incubated for 45 minutes.
1232 Cells were then collected, and cell pellets were lysed in 350 μL of lyses buffer
1233 (12mM Trish-HCl, 0.1x PBS, 6 mM EDTA, 0.5% SDS) supplemented with 40 μL
1234 Proteinase k (20mg/ml) and 10 μL RNAse A (10mg/ml) for 10 minutes at RT and
1235 then 15 minutes at 56°C. Samples were sonicated to obtain chromatin fragments

1236 of ~200 - 600 base pairs (bp). After collecting the 10% of the sample as input control,
1237 samples were diluted using 1.6 mL of ChIP dilution buffer (10 mM Tris-HCl, 140 mM NaCl,
1238 0.1% DOC, 1% Triton-X, 1 mM EDTA). Diluted DNA samples were then denatured for 10
1239 min at 95°C and cool down at 4°C to preserve ssDNA. Next, ssDNA samples were
1240 immunoprecipitated as described above using Dynabeads Protein G (Invitrogen) pre-
1241 conjugated with antibodies against CldU (rat monoclonal anti-BrdU clone BU1/75) and
1242 IdU (mouse monoclonal anti-BrdU clone B44). Eluted ssDNA samples and inputs were
1243 purified with PCR Clean UP kit and eluted in water. ChIP DNA was prepared with xGen
1244 ssDNA & low input DNA library preparation kit and sequenced using NovaSeq X Plus 10
1245 Billion 2x150 PE (142M PE reads per sample).
1246 The raw fastq files were processed using a pipeline of Nextflow. In short, the raw
1247 reads were trimmed to remove adapter sequences, aligned to mouse mm10 genome,
1248 and filtered as described (54). The filtered alignments were then merged, and the
1249 CldU/IdU ratios were calculated with deepTools and normalized with the default window
1250 size of 5000 and loess span of 300000. The coverage tracts of individual and merged
1251 bam files were generated with deepTools (v3.5.4).
1252 **Statistical Analysis.** *In vitro* and *in vivo* data are presented as the median values
1253 or mean ± S.D. (standard deviation). Statistical analyses were performed using Student's
1254 t-test, one-way or two-way ANOVA test as specified in figure legends. Results from
1255 survival experiments were analyzed with a Log-rank test and expressed as Kaplan–Meier
1256 survival curves.
1257
1258 **References**
1259 1. Beach RR, Ricci-Tam C, Brennan CM, Moomau CA, Hsu P-h, Hua B, et al.
1260 Aneuploidy causes non-genetic individuality. Cell. 2017;169(2):229-42. e21.
1261 2. Bakhoum SF, Ngo B, Laughney AM, Cavallo J-A, Murphy CJ, Ly P, et al.
1262 Chromosomal instability drives metastasis through a cytosolic DNA response. Nature.
1263 2018;553(7689):467-72.
1264 3. Santaguida S, Richardson A, Iyer DR, M'Saad O, Zasadil L, Knouse KA, et al.
1265 Chromosome Mis-segregation Generates Cell-Cycle-Arrested Cells with Complex Karyotypes
1266 that Are Eliminated by the Immune System. Developmental Cell. 2017;41(6):638-51.e5.

1267 4. Davoli T, Xu AW, Mengwasser KE, Sack LM, Yoon JC, Park PJ, et al. Cumulative
1268 haploinsufficiency and triplosensitivity drive aneuploidy patterns and shape the cancer genome.
1269 Cell. 2013;155(4):948-62.
1270 5. Passerini V, Ozeri-Galai E, De Pagter MS, Donnelly N, Schmalbrock S,
1271 Kloosterman WP, et al. The presence of extra chromosomes leads to genomic instability. Nature
1272 communications. 2016;7(1):1-12.
1273 6. Gordon DJ, Resio B, Pellman D. Causes and consequences of aneuploidy in cancer.
1274 Nature Reviews Genetics. 2012;13(3):189-203.
1275 7. Holland AJ, Cleveland DW. Boveri revisited: chromosomal instability, aneuploidy
1276 and tumorigenesis. Nature reviews Molecular cell biology. 2009;10(7):478-87.
1277 8. Sack LM, Davoli T, Li MZ, Li Y, Xu Q, Naxerova K, et al. Profound Tissue
1278 Specificity in Proliferation Control Underlies Cancer Drivers and Aneuploidy Patterns. Cell.
1279 2018;173(2):499-514.e23.
1280 9. Beroukhim R, Mermel CH, Porter D, Wei G, Raychaudhuri S, Donovan J, et al.
1281 The landscape of somatic copy-number alteration across human cancers. Nature.
1282 2010;463(7283):899-905.
1283 10. Fragkos M, Ganier O, Coulombe P, Méchali M. DNA replication origin activation
1284 in space and time. Nature Reviews Molecular Cell Biology. 2015;16(6):360-74.
1285 11. Arias EE, Walter JC. Strength in numbers: preventing rereplication via multiple
1286 mechanisms in eukaryotic cells. Genes & development. 2007;21(5):497-518.
1287 12. Petropoulos M, Tsaniras SC, Taraviras S, Lygerou Z. Replication licensing
1288 aberrations, replication stress, and genomic instability. Trends in biochemical sciences.
1289 2019;44(9):752-64.
1290 13. Zhou Y, Pozo PN, Oh S, Stone HM, Cook JG. Distinct and sequential re-replication
1291 barriers ensure precise genome duplication. PLOS Genetics. 2020;16(8):e1008988.
1292 14. Berti M, Cortez D, Lopes M. The plasticity of DNA replication forks in response
1293 to clinically relevant genotoxic stress. Nature Reviews Molecular Cell Biology. 2020;21(10):633-
1294 51.
1295 15. Frouin I, Montecucco A, Spadari S, Maga G. DNA replication: a complex matter.
1296 EMBO reports. 2003;4(7):666-70.

1297 16. Iyer DR, Rhind N. Replication fork slowing and stalling are distinct, checkpoint-
1298 independent consequences of replicating damaged DNA. PLOS Genetics. 2017;13(8):e1006958.
1299 17. Mulla WA, Seidel CW, Zhu J, Tsai HJ, Smith SE, Singh P, et al. Aneuploidy as a
1300 cause of impaired chromatin silencing and mating-type specification in budding yeast. Elife.
1301 2017;6.
1302 18. Giunta S, Hervé S, White RR, Wilhelm T, Dumont M, Scelfo A, et al. CENP-A
1303 chromatin prevents replication stress at centromeres to avoid structural aneuploidy. Proceedings
1304 of the National Academy of Sciences. 2021;118(10):e2015634118.
1305 19. Lambuta RA, Nanni L, Liu Y, Diaz-Miyar J, Iyer A, Tavernari D, et al. Whole-
1306 genome doubling drives oncogenic loss of chromatin segregation. Nature. 2023.
1307 20. Muñoz S, Búa S, Rodríguez-Acebes S, Megías D, Ortega S, de Martino A, et al.
1308 In Vivo DNA Re-replication Elicits Lethal Tissue Dysplasias. Cell Reports. 2017;19(5):928-38.
1309 21. Técher H, Koundrioukoff S, Nicolas A, Debatisse M. The impact of replication
1310 stress on replication dynamics and DNA damage in vertebrate cells. Nat Rev Genet.
1311 2017;18(9):535-50.
1312 22. Flach J, Bakker ST, Mohrin M, Conroy PC, Pietras EM, Reynaud D, et al.
1313 Replication stress is a potent driver of functional decline in ageing haematopoietic stem cells.
1314 Nature. 2014;512(7513):198-202.
1315 23. Tsunematsu T, Takihara Y, Ishimaru N, Pagano M, Takata T, Kudo Y. Aurora-A
1316 controls pre-replicative complex assembly and DNA replication by stabilizing geminin in mitosis.
1317 Nature Communications. 2013;4(1):1885.
1318 24. Liontos M, Koutsami M, Sideridou M, Evangelou K, Kletsas D, Levy B, et al.
1319 Deregulated overexpression of hCdt1 and hCdc6 promotes malignant behavior. Cancer research.
1320 2007;67(22):10899-909.
1321 25. Fu H, Redon CE, Thakur BL, Utani K, Sebastian R, Jang S-M, et al. Dynamics of
1322 replication origin over-activation. Nature Communications. 2021;12(1):3448.
1323 26. Connor AA, Gallinger S. Pancreatic cancer evolution and heterogeneity:
1324 integrating omics and clinical data. Nature Reviews Cancer. 2022;22(3):131-42.
1325 27. Ryan DP, Hong TS, Bardeesy N. Pancreatic Adenocarcinoma. New England
1326 Journal of Medicine. 2014;371(11):1039-49.

1327 28. Bailey P, Chang DK, Nones K, Johns AL, Patch A-M, Gingras M-C, et al. Genomic
1328 analyses identify molecular subtypes of pancreatic cancer. Nature. 2016;531(7592):47-52.
1329 29. Cao L, Huang C, Cui Zhou D, Hu Y, Lih TM, Savage SR, et al. Proteogenomic
1330 characterization of pancreatic ductal adenocarcinoma. Cell. 2021;184(19):5031-52.e26.
1331 30. Hayashi A, Hong J, Iacobuzio-Donahue CA. The pancreatic cancer genome
1332 revisited. Nature Reviews Gastroenterology & Hepatology. 2021;18(7):469-81.
1333 31. Carugo A, Genovese G, Seth S, Nezi L, Rose JL, Bossi D, et al. In Vivo
1334 Functional Platform Targeting Patient-Derived Xenografts Identifies WDR5-Myc Association as
1335 a Critical Determinant of Pancreatic Cancer. Cell Reports. 2016;16(1):133-47.
1336 32. Giuliani V, Miller MA, Liu C-Y, Hartono SR, Class CA, Bristow CA, et al.
1337 PRMT1-dependent regulation of RNA metabolism and DNA damage response sustains pancreatic
1338 ductal adenocarcinoma. Nature Communications. 2021;12(1):4626.
1339 33. Ali A, Tyagi S. Diverse roles of WDR5-RbBP5-ASH2L-DPY30 (WRAD) complex
1340 in the functions of the SET1 histone methyltransferase family. Journal of biosciences.
1341 2017;42(1):155-9.
1342 34. Ali A, Veeranki SN, Tyagi S. A SET-domain-independent role of WRAD complex
1343 in cell-cycle regulatory function of mixed lineage leukemia. Nucleic acids research.
1344 2014;42(12):7611-24.
1345 35. Ernst P, Vakoc CR. WRAD: enabler of the SET1-family of H3K4
1346 methyltransferases. Briefings in functional genomics. 2012;11(3):217-26.
1347 36. Wang H, Fan Z, Shliaha PV, Miele M, Hendrickson RC, Jiang X, et al. H3K4me3
1348 regulates RNA polymerase II promoter-proximal pause-release. Nature. 2023;615(7951):339-48.
1349 37. Cenik BK, Shilatifard A. COMPASS and SWI/SNF complexes in development and
1350 disease. Nature Reviews Genetics. 2021;22(1):38-58.
1351 38. Campbell SA, Bégin J, McDonald CL, Vanderkruk B, Stephan TL, Hoffman BG.
1352 H3K4 trimethylation is required for postnatal pancreatic endocrine cell functional maturation.
1353 bioRxiv. 2020:2020.11.29.402990.
1354 39. Campbell SA, McDonald CL, Krentz NAJ, Lynn FC, Hoffman BG. TrxG Complex
1355 Catalytic and Non-catalytic Activity Play Distinct Roles in Pancreas Progenitor Specification and
1356 Differentiation. Cell Reports. 2019;28(7):1830-44.e6.

1357 40. Dixit D, Prager BC, Gimple RC, Miller TE, Wu Q, Yomtoubian S, et al.
1358 Glioblastoma stem cells reprogram chromatin in vivo to generate selective therapeutic
1359 dependencies on DPY30 and phosphodiesterases. Science Translational Medicine.
1360 2022;14(626):eabf3917.
1361 41. Simboeck E, Gutierrez A, Cozzuto L, Beringer M, Caizzi L, M Keyes W, et al.
1362 DPY30 regulates pathways in cellular senescence through ID protein expression. The EMBO
1363 journal. 2013;32(16):2217-30.
1364 42. Yang Z, Shah K, Khodadadi-Jamayran A, Jiang H. Control of Hematopoietic Stem
1365 and Progenitor Cell Function through Epigenetic Regulation of Energy Metabolism and Genome
1366 Integrity. Stem Cell Reports. 2019;13(1):61-75.
1367 43. Zhao T, Hong Y, Ming G-l, Song H. Loss of chromatin modulator Dpy30
1368 compromises proliferation and differentiation of postnatal neural stem cells. Journal of Molecular
1369 Cell Biology. 2019;12(1):2-3.
1370 44. Zhao Y, Hao X, Li Z, Feng X, Katz J, Michalek SM, et al. Role of chromatin
1371 modulator Dpy30 in osteoclast differentiation and function. Bone. 2022;159:116379.
1372 45. Pferdehirt RR, Kruesi WS, Meyer BJ. An MLL/COMPASS subunit functions in
1373 the C. elegans dosage compensation complex to target X chromosomes for transcriptional
1374 regulation of gene expression. Genes & development. 2011;25(5):499-515.
1375 46. Hingorani SR, Wang L, Multani AS, Combs C, Deramaudt TB, Hruban RH, et al.
1376 Trp53R172H and KrasG12D cooperate to promote chromosomal instability and widely metastatic
1377 pancreatic ductal adenocarcinoma in mice. Cancer Cell. 2005;7(5):469-83.
1378 47. Yan L, Tu B, Yao J, Gong J, Carugo A, Bristow CA, et al. Targeting Glucose
1379 Metabolism Sensitizes Pancreatic Cancer to MEK Inhibition. Cancer Research. 2021;81(15):4054-
1380 65.
1381 48. Dou Y, Milne TA, Ruthenburg AJ, Lee S, Lee JW, Verdine GL, et al. Regulation
1382 of MLL1 H3K4 methyltransferase activity by its core components. Nature Structural & Molecular
1383 Biology. 2006;13(8):713-9.
1384 49. Bryan AF, Wang J, Howard GC, Guarnaccia AD, Woodley CM, Aho ER, et al.
1385 WDR5 is a conserved regulator of protein synthesis gene expression. Nucleic Acids Research.
1386 2020;48(6):2924-41.

1387 50. Grant GD, Kedziora KM, Limas JC, Cook JG, Purvis JE. Accurate delineation of
1388 cell cycle phase transitions in living cells with PIP-FUCCI. Cell Cycle. 2018;17(21-22):2496-516.
1389 51. Tremblay V, Zhang P, Chaturvedi C-P, Thornton J, Brunzelle Joseph S, Skiniotis
1390 G, et al. Molecular Basis for DPY-30 Association to COMPASS-like and NURF Complexes.
1391 Structure. 2014;22(12):1821-30.
1392 52. Roy S, Luzwick JW, Schlacher K. SIRF: Quantitative in situ analysis of protein
1393 interactions at DNA replication forks. J Cell Biol. 2018;217(4):1521-36.
1394 53. Roy S, Schlacher K. SIRF: A Single-cell Assay for in situ Protein Interaction with
1395 Nascent DNA Replication Forks. Bio Protoc. 2019;9(18):e3377.
1396 54. Marchal C, Sasaki T, Vera D, Wilson K, Sima J, Rivera-Mulia JC, et al. Genome-
1397 wide analysis of replication timing by next-generation sequencing with E/L Repli-seq. Nature
1398 Protocols. 2018;13(5):819-39.
1399 55. Bakhoum SF, Cantley LC. The Multifaceted Role of Chromosomal Instability in
1400 Cancer and Its Microenvironment. Cell. 2018;174(6):1347-60.
1401 56. Decout A, Katz JD, Venkatraman S, Ablasser A. The cGAS–STING pathway as a
1402 therapeutic target in inflammatory diseases. Nature Reviews Immunology. 2021;21(9):548-69.
1403 57. Chuang L-C, Teixeira LK, Wohlschlegel JA, Henze M, Yates JR, Méndez J, et al.
1404 Phosphorylation of Mcm2 by Cdc7 Promotes Pre-replication Complex Assembly during Cell-
1405 Cycle Re-entry. Molecular Cell. 2009;35(2):206-16.
1406 58. Vaziri C, Saxena S, Jeon Y, Lee C, Murata K, Machida Y, et al. A p53-Dependent
1407 Checkpoint Pathway Prevents Rereplication. Molecular Cell. 2003;11(4):997-1008.
1408 59. Kalfalah FM, Berg E, Christensen MO, Linka RM, Dirks WG, Boege F, et al.
1409 Spatio-temporal regulation of the human licensing factor Cdc6 in replication and mitosis. Cell
1410 Cycle. 2015;14(11):1704-15.
1411 60. McGarry TJ, Kirschner MW. Geminin, an Inhibitor of DNA Replication, Is
1412 Degraded during Mitosis. Cell. 1998;93(6):1043-53.
1413 61. Blank JL, Liu XJ, Cosmopoulos K, Bouck DC, Garcia K, Bernard H, et al. Novel
1414 DNA Damage Checkpoints Mediating Cell Death Induced by the NEDD8-Activating Enzyme
1415 Inhibitor MLN4924. Cancer Research. 2013;73(1):225-34.
1416 62. Li A, Blow JJ. Cdt1 downregulation by proteolysis and geminin inhibition prevents
1417 DNA re-replication in Xenopus. Embo j. 2005;24(2):395-404.

1418 63. Walter D, Hoffmann S, Komseli E-S, Rappsilber J, Gorgoulis V, Sørensen CS.
1419 SCFCyclin F-dependent degradation of CDC6 suppresses DNA re-replication. Nature
1420 Communications. 2016;7(1):10530.
1421 64. Neelsen KJ, Zanini IM, Mijic S, Herrador R, Zellweger R, Chaudhuri AR, et al.
1422 Deregulated origin licensing leads to chromosomal breaks by rereplication of a gapped DNA
1423 template. Genes & development. 2013;27(23):2537-42.
1424 65. Mehta A, Merkel OM. Immunogenicity of Cas9 Protein. Journal of Pharmaceutical
1425 Sciences. 2020;109(1):62-7.
1426 66. Seth S, Li CY, Ho IL, Corti D, Loponte S, Sapio L, et al. Pre-existing Functional
1427 Heterogeneity of Tumorigenic Compartment as the Origin of Chemoresistance in Pancreatic
1428 Tumors. Cell Rep. 2019;26(6):1518-32.e9.
1429 67. Ho I-L, Li C-Y, Wang F, Zhao L, Liu J, Yen E-Y, et al. Clonal dominance defines
1430 metastatic dissemination in pancreatic cancer. Science Advances. 2024;10(11):eadd9342.
1431 68. Ying H, Kimmelman Alec C, Lyssiotis Costas A, Hua S, Chu Gerald C, Fletcher-
1432 Sananikone E, et al. Oncogenic Kras Maintains Pancreatic Tumors through Regulation of Anabolic
1433 Glucose Metabolism. Cell. 2012;149(3):656-70.
1434 69. Yao W, Rose JL, Wang W, Seth S, Jiang H, Taguchi A, et al. Syndecan 1 is a
1435 critical mediator of macropinocytosis in pancreatic cancer. Nature. 2019;568(7752):410-4.
1436 70. Padrón LJ, Maurer DM, O'Hara MH, O'Reilly EM, Wolff RA, Wainberg ZA, et
1437 al. Sotigalimab and/or nivolumab with chemotherapy in first-line metastatic pancreatic cancer:
1438 clinical and immunologic analyses from the randomized phase 2 PRINCE trial. Nature Medicine.
1439 2022;28(6):1167-77.
1440 71. Moffitt RA, Marayati R, Flate EL, Volmar KE, Loeza SGH, Hoadley KA, et al.
1441 Virtual microdissection identifies distinct tumor- and stroma-specific subtypes of pancreatic ductal
1442 adenocarcinoma. Nature Genetics. 2015;47(10):1168-78.
1443 72. Puleo F, Nicolle R, Blum Y, Cros J, Marisa L, Demetter P, et al. Stratification of
1444 Pancreatic Ductal Adenocarcinomas Based on Tumor and Microenvironment Features.
1445 Gastroenterology. 2018;155(6):1999-2013.e3.
1446 73. Collisson EA, Sadanandam A, Olson P, Gibb WJ, Truitt M, Gu S, et al. Subtypes
1447 of pancreatic ductal adenocarcinoma and their differing responses to therapy. Nature Medicine.
1448 2011;17(4):500-3.

1449 74. Del Poggetto E, Ho I-L, Balestrieri C, Yen E-Y, Zhang S, Citron F, et al. Epithelial
1450 memory of inflammation limits tissue damage while promoting pancreatic tumorigenesis. Science.
1451 2021;373(6561):eabj0486.
1452 75. Alonso-Curbelo D, Ho Y-J, Burdziak C, Maag JLV, Morris JP, Chandwani R, et
1453 al. A gene–environment-induced epigenetic program initiates tumorigenesis. Nature.
1454 2021;590(7847):642-8.
1455 76. Lomberk G, Blum Y, Nicolle R, Nair A, Gaonkar KS, Marisa L, et al. Distinct
1456 epigenetic landscapes underlie the pathobiology of pancreatic cancer subtypes. Nature
1457 Communications. 2018;9(1):1978.
1458 77. Dias J, Van Nguyen N, Georgiev P, Gaub A, Brettschneider J, Cusack S, et al.
1459 Structural analysis of the KANSL1/WDR5/KANSL2 complex reveals that WDR5 is required for
1460 efficient assembly and chromatin targeting of the NSL complex. Genes & development.
1461 2014;28(9):929-42.
1462 78. Li Q, Mao F, Zhou B, Huang Y, Zou Z, denDekker AD, et al. p53 Integrates
1463 Temporal WDR5 Inputs during Neuroectoderm and Mesoderm Differentiation of Mouse
1464 Embryonic Stem Cells. Cell Rep. 2020;30(2):465-80.e6.
1465 79. Siladi AJ, Wang J, Florian AC, Thomas LR, Creighton JH, Matlock BK, et al. WIN
1466 site inhibition disrupts a subset of WDR5 function. Scientific Reports. 2022;12(1):1848.
1467 80. Zhao J, Chen W, Pan Y, Zhang Y, Sun H, Wang H, et al. Structural insights into
1468 the recognition of histone H3Q5 serotonylation by WDR5. Science Advances.
1469 2021;7(25):eabf4291.
1470 81. Morgan MAJ, Shilatifard A. Epigenetic moonlighting: Catalytic-independent
1471 functions of histone modifiers in regulating transcription. Science Advances.
1472 2023;9(16):eadg6593.
1473 82. Saldivar JC, Hamperl S, Bocek MJ, Chung M, Bass TE, Cisneros-Soberanis F, et
1474 al. An intrinsic S/G₂ checkpoint enforced by ATR. Science. 2018;361(6404):806-10.
1475 83. Saldivar JC, Cortez D, Cimprich KA. The essential kinase ATR: ensuring faithful
1476 duplication of a challenging genome. Nature reviews Molecular cell biology. 2017;18(10):622-36.
1477 84. Zeng J, Hills SA, Ozono E, Diffley JFX. Cyclin E-induced replicative stress drives
1478 p53-dependent whole-genome duplication. Cell. 2023;186(3):528-42.e14.

1479 85. Donnelly N, Storchová Z. Dynamic karyotype, dynamic proteome: buffering the
1480 effects of aneuploidy. Biochimica et Biophysica Acta (BBA) - Molecular Cell Research.
1481 2014;1843(2):473-81.
1482 86. Dungrawala H, Cortez D. Purification of proteins on newly synthesized DNA using
1483 iPOND. Methods Mol Biol. 2015;1228:123-31.
1484 87. Halliwell JA, Gravells P, Bryant HE. DNA Fiber Assay for the Analysis of DNA
1485 Replication Progression in Human Pluripotent Stem Cells. Current Protocols in Stem Cell Biology.
1486 2020;54(1):e115.
1487 88. Di Pilato M, Kfuri-Rubens R, Pruessmann JN, Ozga AJ, Messemaker M, Cadilha
1488 BL, et al. CXCR6 positions cytotoxic T cells to receive critical survival signals in the tumor
1489 microenvironment. Cell. 2021;184(17):4512-30.e22.
1490 89. Terranova C, Tang M, Orouji E, Maitituoheti M, Raman A, Amin S, et al. An
1491 Integrated Platform for Genome-wide Mapping of Chromatin States Using High-throughput ChIP-
1492 sequencing in Tumor Tissues. J Vis Exp. 2018(134).
1493 90. Bolger AM, Lohse M, Usadel B. Trimmomatic: a flexible trimmer for Illumina
1494 sequence data. Bioinformatics. 2014;30(15):2114-20.
1495 91. Langmead B, Salzberg SL. Fast gapped-read alignment with Bowtie 2. Nature
1496 Methods. 2012;9(4):357-9.
1497 92. Li H, Handsaker B, Wysoker A, Fennell T, Ruan J, Homer N, et al. The Sequence
1498 Alignment/Map format and SAMtools. Bioinformatics. 2009;25(16):2078-9.
1499 93. Zhang Y, Liu T, Meyer CA, Eeckhoute J, Johnson DS, Bernstein BE, et al. Model-
1500 based Analysis of ChIP-Seq (MACS). Genome Biology. 2008;9(9):R137.
1501 94. Quinlan AR, Hall IM. BEDTools: a flexible suite of utilities for comparing genomic
1502 features. Bioinformatics. 2010;26(6):841-2.
1503 95. Ramírez F, Dündar F, Diehl S, Grüning BA, Manke T. deepTools: a flexible
1504 platform for exploring deep-sequencing data. Nucleic Acids Res. 2014;42(Web Server
1505 issue):W187-91.
1506 96. Ross-Innes CS, Stark R, Teschendorff AE, Holmes KA, Ali HR, Dunning MJ, et
1507 al. Differential oestrogen receptor binding is associated with clinical outcome in breast cancer.
1508 Nature. 2012;481(7381):389-93.

1509 97. Wickham H. ggplot2: elegant graphics for data analysis. New York: Springer New
1510 York, NY; 2016. Available from: https://link.springer.com/book/10.1007/978-0-387-98141-3.
1511 98. Buenrostro JD, Giresi PG, Zaba LC, Chang HY, Greenleaf WJ. Transposition of
1512 native chromatin for fast and sensitive epigenomic profiling of open chromatin, DNA-binding
1513 proteins and nucleosome position. Nature Methods. 2013;10(12):1213-8.
1514 99. Heinz S, Benner C, Spann N, Bertolino E, Lin YC, Laslo P, et al. Simple
1515 Combinations of Lineage-Determining Transcription Factors Prime cis-Regulatory Elements
1516 Required for Macrophage and B Cell Identities. Molecular Cell. 2010;38(4):576-89.
1517 100. Andrews S. FastQC. A quality control tool for high throughput sequence data 2010.
1518 Available from: http://www.bioinformatics.babraham.ac.uk/projects/fastqc/.
1519 101. Li H, Durbin R. Fast and accurate short read alignment with Burrows-Wheeler
1520 transform. Bioinformatics. 2009;25(14):1754-60.
1521 102. Geraldine A. Van der Auwera BDOC. Genomics in the Cloud: O'Reilly Media,
1522 Inc.; 2020.
1523 103. Talevich E, Shain AH, Botton T, Bastian BC. CNVkit: Genome-Wide Copy
1524 Number Detection and Visualization from Targeted DNA Sequencing. PLOS Computational
1525 Biology. 2016;12(4):e1004873.
1526 104. Dobin A, Davis CA, Schlesinger F, Drenkow J, Zaleski C, Jha S, et al. STAR:
1527 ultrafast universal RNA-seq aligner. Bioinformatics. 2013;29(1):15-21.
1528 105. Liao Y, Smyth GK, Shi W. The R package Rsubread is easier, faster, cheaper and
1529 better for alignment and quantification of RNA sequencing reads. Nucleic Acids Research.
1530 2019;47(8):e47-e.
1531 106. McCarthy DJ, Chen Y, Smyth GK. Differential expression analysis of multifactor
1532 RNA-Seq experiments with respect to biological variation. Nucleic Acids Research.
1533 2012;40(10):4288-97.
1534 107. Ritchie ME, Phipson B, Wu D, Hu Y, Law CW, Shi W, et al. limma powers
1535 differential expression analyses for RNA-sequencing and microarray studies. Nucleic Acids
1536 Research. 2015;43(7):e47-e.
1537 108. Korotkevich G, Sukhov V, Budin N, Shpak B, Artyomov MN, Sergushichev A.
1538 Fast gene set enrichment analysis. bioRxiv. 2021:060012.

1539 109. Wolock SL, Lopez R, Klein AM. Scrublet: Computational Identification of Cell
1540 Doublets in Single-Cell Transcriptomic Data. Cell Syst. 2019;8(4):281-91.e9.
1541 110. Hao Y, Hao S, Andersen-Nissen E, Mauck WM, 3rd, Zheng S, Butler A, et al.
1542 Integrated analysis of multimodal single-cell data. Cell. 2021;184(13):3573-87.e29.
1543 111. Leland McInnes JHaJM. UMAP: Uniform Manifold Approximation and Projection
1544 for Dimension Reduction: arXiv; 2018. Available from: https://arxiv.org/abs/1802.03426.
1545

1546 **Acknowledgments:** We thank Michael Kim for PDX-derived PDAC cell lines; all
1547 Draetta lab members and Guoxin Feng for scientific discussion; R. Nguyen and J.
1548 Martinez in the Department of Genomic Medicine at MD Anderson for lab management;
1549 Michael Peoples and Vandhana Ramamoorthy with the MD Anderson TRACTION
1550 platform for valuable support with cloning; Alejandro Hernandez Martinez, Edward Q.
1551 Chang and Ningping Feng with the MD Anderson TRACTION platform for support with
1552 tissue imaging acquisition and drug formulation; and Vivien Van, Charles Kingsley and
1553 Jorge Delacerda at the MD Anderson Small Animals Imaging Facility; The Animal Support
1554 Facility (RASF), which was partially funded by the MD Anderson Support Grant
1555 CA016672; the MD Anderson Department of Veterinary Medicine; the MD Anderson
1556 Advanced Microscopy Core, which was funded by NIH S10 RR029552; Asha Multani and
1557 the MD Anderson Cytogenetics and Cell Authentication Core; Erika Thompson, Hongli
1558 Tang, David Pollock and the MD Anderson Advanced Technology Genomics Core
1559 (ATGC), which was funded by the CA016672 Core Grant; Karen Ramirez, David Dwyer,
1560 Veena Papanna, and the MD Anderson Advanced Cytometry and Sorting Facility, which
1561 was funded by the NCI Cancer Center Support Grant P30CA16672; and Genscript for
1562 support and service. The mEmerald-MCM vectors were a gift from Michael Davidson, the
1563 lentiCRISPR v2 vector was a gift from Feng Zhang. The pcDNA3.1 Flag-hDPY30 vector
1564 was a gift from Kai Ge. The psPAX2 and pMD2G vectors were a gift from Didier Trono.
1565 Schematics were created using BioRender.com. This research was supported by the
1566 2022 AACR–AstraZeneca START Grant, Grant Number 22-40-12-CITR to F.C.; AIRC
1567 and the European Union's Horizon 2020 research and innovation program under the
1568 Marie Skłodowska-Curie grant agreement no. 800924 to F.C.; CPRIT Training Award
1569 (RP210028) to E.Y.; Cancer Research and Prevention Institute of Texas (CPRIT) grant

RP190599, NIH/NCI R01 CA258917, the Andrew Sabin Family Foundation grant, and the V Foundation grant (V2020-018) to A.V.; NIH/NCI SPORE in gastrointestinal cancer grant P50CA221707 to G.F.D and A.V.; UT MD Anderson Cancer Center Start-Up Funds to A.V.; UT MD Anderson Cancer Center Pancreatic Cancer Moon Shot and Pancreatic Cancer Action Network (PanCAN) to G.F.D.; NIH/NCI P01 CA117969-12 to A.V. and G.F.D. G.F.D. was also supported by the Sewell Family Distinguished University Chair in Genomic Medicine.

Author contributions: Conceptualization: F.C., A.V., G.F.D.; Methodology: F.C., L.P., I.H., C.B., E.Y., Z.L., L.Z., L.C.M, P.J., S.A., M.D.P., W.Y., A.Z., C.J.; Software: Y.C., C.B., L.Z., Z.L., E.Y., S.S., L.W., G.T., C.Bo.; Validation: F.C., L.P, I.H, E.Y., L.C, H.K., R.S., Z.C., I.S., N.P., S.A., K.C.C, C.A.D., C.L., M.M., K.R., C.J.; Formal Analysis: F.C., L.P., Z.L., C.B., L.Z., E.Y., S.S., M.D.P.; Investigation: F.C., L.P, I.H, E.Y., K.C.C., L.C.M., M.D.P.; Resources: F.C., L.P., I.H., C.B., Z.L., L.Z., E.Y., R.S., L.C.M., S.A., S.J., B.G.H., B.V., C.L., M.M., K.R., H.W., W.Y., V.G., T.H., G.T., L.W., M.D.P.; Data curation: F.C., L.P., I.H., Z.L., C.B., L.Z., E.Y.; Writing – Original draft: F.C., A.V., G.F.D.; Writing – Review and Editing: F.C., A.V., G.F.D., S.G.; Visualization: F.C., C.B., Z.L., E.Y.; Supervision: F.C., A.V., G.F.D; Project Administration: F.C., A.V., G.F.D; Funding Acquisition: F.C., A.V., G.F.D;

Competing interest declaration

The authors declare that they have no conflict of interest.

Figure legends

Figure 1

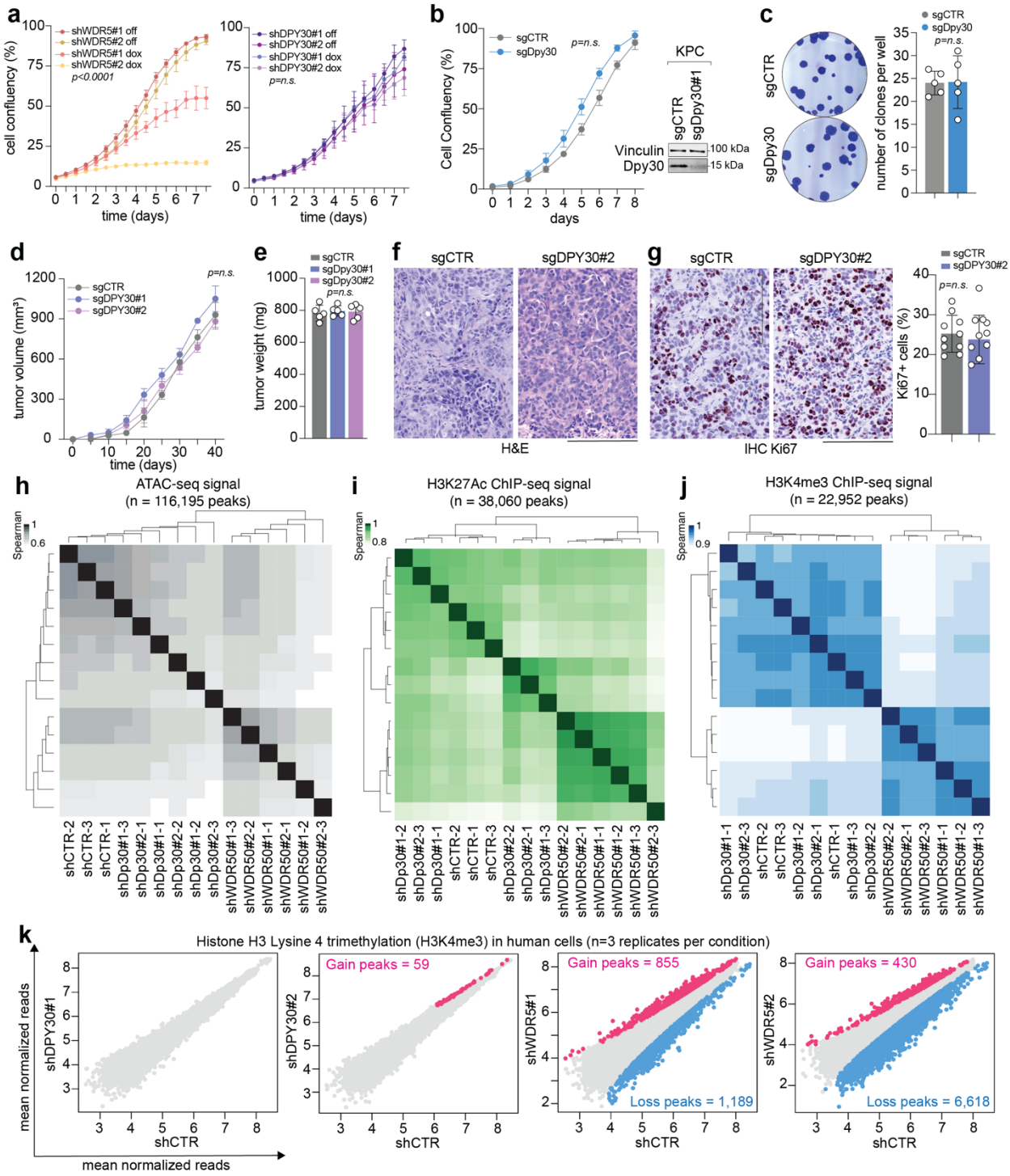

Figure 1. *DPY30* is dispensable for cancer cell proliferation and H3K4 trimethylation.

a. Growth curve analysis of PATC53 cells carrying shRNAs targeting WDR5 (shWDR5), DPY30 (shDPY30) or control (shCTR) and treated with vehicle (off) or

1599 doxycycline (dox) to induce the gene silencing. **b.** Growth curve (left) and western blot
1600 (right) of control (sgCTR) or *Dpy30*-KO (sgDPY30) KPC cells. **c.** Clonogenic assay of
1601 KPC cells, as described in b, is shown (left) and quantified (right). **d-e.** Volume (d) and
1602 weight (e) of tumors from control (sgCTR) or DPY30-KO (sgDPY30) PATC53 cells grown
1603 in NSG mice. **f-g**. Micrographs showing the histology and Ki67 labeling in tumors
1604 described in (d). Hematoxylin and eosin (H&E) (f) staining, Ki67 IHC staining (g, left) and
1605 quantification (g, right) are shown. **h-j.** Heatmap showing Spearman correlations between
1606 samples and biological replicates of ATACseq (h), and H3K27ac (i) or H3K4me3 (j) Chip-
1607 seq in shCTR, shDPY30 or shWDR5 PATC53 cells. Samples are clustered by Euclidean
1608 distance and single-linkage clustering. **k.** Scatter plot showing mean normalized signals
1609 of H3K4me3 from samples described in j. Regions that significantly (FDR < 0.05) gained
1610 or lost H3K4me3 peaks in shDPY30 or shWDR5 versus shCTR are depicted in pink and
1611 blue, respectively. Not significant peaks are indicated as gray dots. In (a-e, g), data are
1612 expressed as mean ± SD, and dots represent biological replicates. Statistical significance
1613 was calculated using one-way ANOVA and Tukey's multiple comparison tests (a, d, e),
1614 or Student t test (b, c, g). In panels f-g, scale bar = 200 μm.

Figure 2

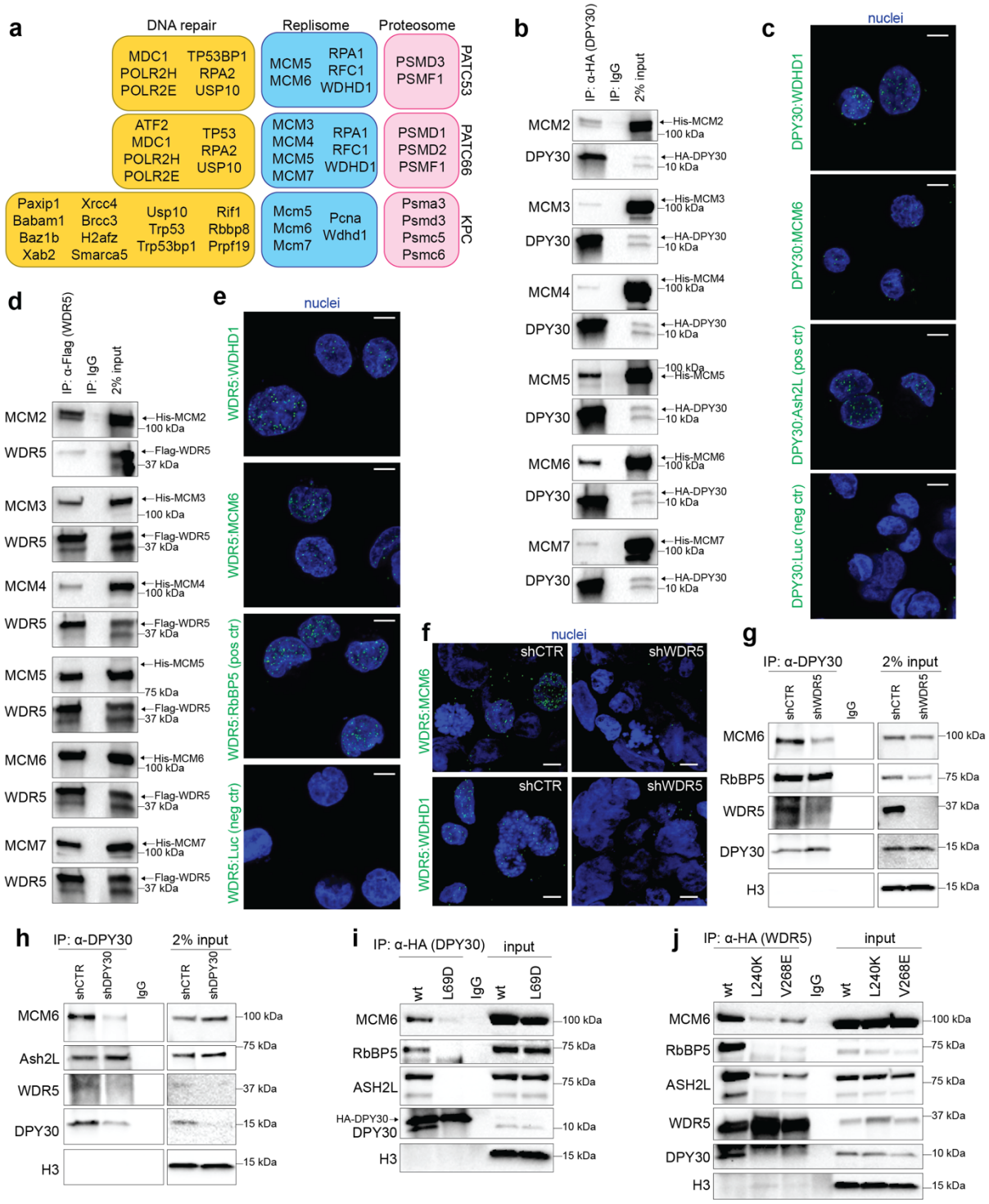

Figure 2. The WRAD core interacts with WDHD1 and the MCM complex.

a. Schematic representation of DPY30 interactors involved in DNA repair, replisome, and proteosome signaling pathways in PATC53, PATC66, and KPC cells. **b.**

1619 Western blot analysis of the indicated proteins in 293T cells co-overexpressing HA-
1620 tagged human *DPY30* and His-tagged human MCM complex subunits. Control IgG and
1621 input are shown. **c.** Proximity Ligation Assay (PLA) staining detecting DPY30 interaction
1622 with WDHD1, MCM6, Ash2L (positive control) or Luciferase (negative control). **d.** Western
1623 blot analysis of the indicated proteins in 293T cells co-overexpressing Flag-tagged human
1624 *WDR5* and His-tagged human MCM complex subunits. Control IgG and input are shown.
1625 **e.** PLA staining detecting WDR5 interaction with WDHD1, MCM6, RbBP5 (positive
1626 control) or Luciferase (negative control). **f.** PLA staining detecting WDR5 interaction with
1627 WDHD1 and MCM6 in PATC53 control (shCTR) or silenced for WDR5 (shWDR5). **g-h.**
1628 Western blot analysis of the indicated proteins in PATC53 cells control (shCTR) or
1629 silenced for WDR5 (shWDR5, g) or DPY30 (shDPy30, h). Control IgG and input are
1630 shown, and H3 was used as a loading control. **i-j.** Western blot analyses of the indicated
1631 proteins in KPC cells control or overexpressing DPY30 wild type (WT) or mutant (L69D)
1632 isoforms (i), and in KPC cells control or overexpressing WDR5 wild type (WT) or mutant
1633 (L240K, V268E) isoforms (j). Control IgG and input are shown, and H3 was used as a
1634 loading control. In figure, scale bar = 5 μm.

Figure 3

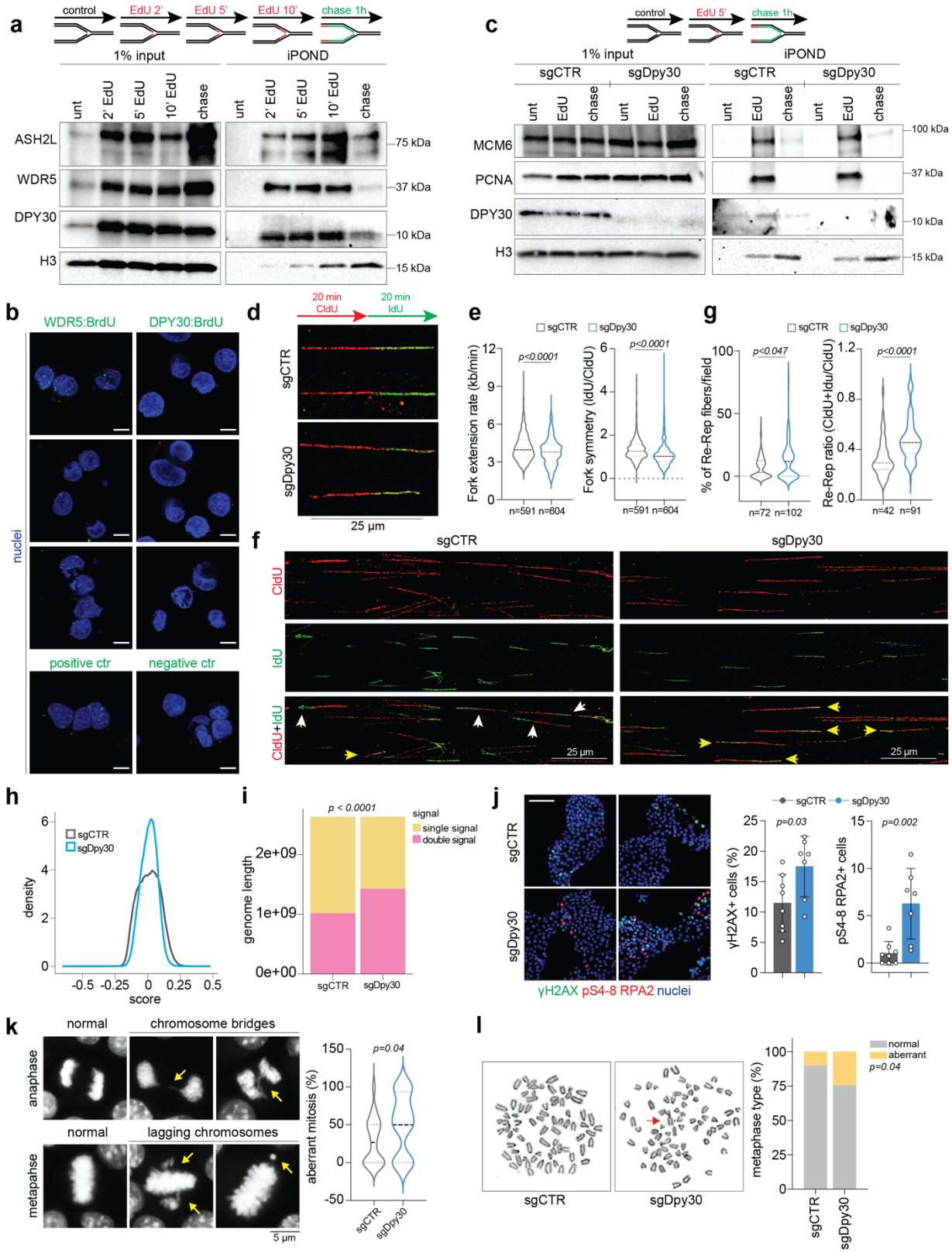

1635

1636 **Figure 3. DPY30 loss leads to DNA re-replication and CIN.**

1637 **a.** Western blot analysis of proteins bound to nascent DNA retrieved using iPOND
1638 or input control in KPC cells. Cells were treated as follows: control (negative control, no
1639 biotin in the click reaction), EdU pulse (EdU treatment for 2, 5 or 10 min), chase (EdU
1640 treatment for 10 min, followed by a 60 min thymidine chase). Histone H3 was used as a
1641 loading control. **b.** Modified PLA (SIRF) assay detecting the interaction between the
1642 incorporated BrdU (5 min pulse) and WDR5 (left) or DPY30 (right). BrdU:PCNA and
1643 BrdU:luciferase were used as positive and negative control, respectively. Scale bar = 5
1644 μm. **c.** Western blot analysis of iPOND or input control in control (sgCTR) or *Dpy30*-KO
1645 (sgDpy30) KPC cells. Cells were treated as described in a. Histone H3 was used as a
1646 loading control. **d.** Schematic illustration and confocal images of DNA fiber assay in
1647 sgCTR and sgDpy30 KPC cells. **e.** Violin plots reporting mean fork progression rate (left)
1648 and fork symmetry (right) in cells as in d. **f.** Confocal images of DNA fiber assay in sgCTR
1649 or sgDpy30 KPC cells. White arrows indicate a fiber with non-aberrant DNA replication,
1650 yellow arrows indicate overlapped CldU and IdU incorporation (DNA re-replication). **g.**
1651 Violin plots reporting the frequency of DNA re-replication (left) and the fiber re-replication
1652 ratio (right) in cells as in f. **h.** Trend curves showing the dual CldU:IdU incorporation
1653 (score) calculated from the density of ChIPseq reads of IdU and CldU IP in sgCTR and
1654 sgDpy30 KPC cells. **h.** Bar plot showing genome length of single (IdU or CldU) and double
1655 nucleotide (CldU+IdU) incorporation in sgCTR and sgDpy30. **j.** immunofluorescence
1656 images of sgCTR or sgDpy30 KPC cells stained for pS4-8 RPA (red), pS139 H2AX
1657 (γH2AX, green), and nuclei (blue). Right, graphs reporting the percentage of γH2AX-
1658 positive or pS4-8 RPA-positive sgCTR or sgDpy30 KPC cells. Each dot represents a
1659 different analyzed field, scale bar = 100 μm. **k.** Left, immunofluorescence images of
1660 mitotic KPC cells stained with DAPI (DNA, white). Yellow arrows indicate lagging
1661 chromosomes and chromosome bridges. Right, violin plot reporting the mean percentage
1662 of sgCTR or sgDpy30 KPC cells with aberrant mitotic outcomes *in vitro*. **k.** Left panel,
1663 images of metaphase spreads in sgCTR or sgDpy30 KPC cells stained with Giemsa
1664 (chromosome). Red arrow indicates chromosome fusion and fragmentation. Right panel,
1665 percentage of KPC cells with normal (gray) or aberrant (yellow) mitotic outcomes. In the
1666 figure, n indicates the number of analyzed events. Data are expressed as mean values ±

SD. Statistical significance was calculated using the Mann-Whitney test (e, g), Student's *t* test (j, k) or Fisher's exact Chi square test (i, l).

Figure 4

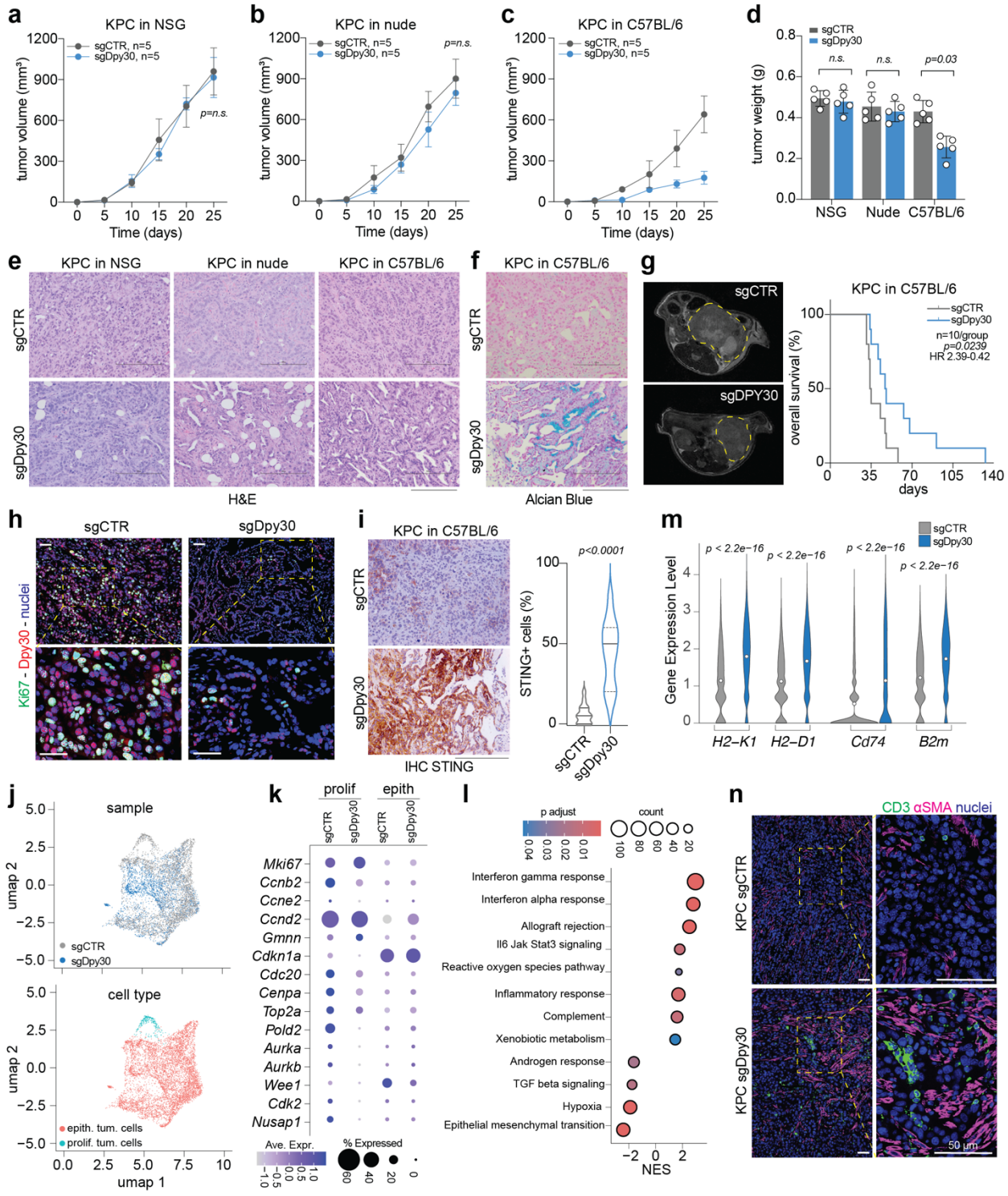

1670 **Figure 4. DPY30 loss results in a distinct immune context-dependent**
1671 **phenotype**

1672 **a–c.** Volume of control (sgCTR) and *Dpy30*-KO (sgDpy30) KPC tumors grown in
1673 the flank of immune-deficient NSG (a), nude (b), or in immune-competent C57BL/6 mice
1674 (c). **d.** Weight (mg) of tumors described in (a–c). **e.** Hematoxylin and eosin (H&E) staining
1675 of tumors from experiments described in (a–d). **f.** Alcian blue staining of tumors from
1676 sgCTR and sgDpy30 KPC cells grown in C57BL/6 mice. **g.** Left, T2 Magnetic Resonance
1677 Imaging (MRI) scans of tumors from sgCTR and sgDpy30 KPC cells grown orthotopically
1678 in the pancreas of C57BL/6 mice. Right, Kaplan-Meier survival curve of tumor-bearing
1679 mice. Statistical significance and Hazard Ratio (HR) were calculated using the Log-rank
1680 test. **h.** Immunofluorescence staining of Ki67 and DPY30 in sgCTR and sgDpy30 KPC
1681 cells grown in C57BL/6 mice. **i.** Left, STING immunohistochemical (IHC) staining of
1682 tumors from sgCTR and sgDpy30 KPC cells grown in C57BL/6 mice Right, violin plot
1683 showing the percentage of STING positive cells per field. **j.** UMAP plots showing bi-
1684 dimensional cluster distribution of sgCTR (n=3) or sgDpy30 (n=3) KPC tumor epithelial
1685 cells after filtering and quality control. **k.** Bubble plot showing expression levels of the
1686 genes involved in cell cycle analyzed from the single-cell RNA sequencing data as
1687 described in j. Size of dots represents the percentage of cells expressing the gene; color
1688 scale shows the average expression level **l.** Bubble plot showing the over-representation
1689 analysis of genes enriched in sgDpy30 KPC cells. Gene expression was calculated using
1690 Seurat. **m.** Violin plot showing the expression of *B2m, H2-K1, H2-D1 and Cd74* per cell
1691 calculated using Seurat in sgCTR and sgDpy30 KPC cells. **n.** Immunofluorescence
1692 staining of CD3 and αSMA in sgCTR or sgDpy30 KPC cells grown in C57BL/6 mice. In
1693 the figure, n indicates the number of mice analyzed. In (a–d), data are expressed as mean
1694 ± SD and statistical significance was calculated using an unpaired One-way ANOVA (a-
1695 c) or Student's *t* test (d). In (l, m), data are expressed as median values and statistical
1696 significance was calculated using the Mann Whitney test. In (e–f, i), scale bar = 200 μm.
1697 In (h, n), scale bar = 50 μm.

Figure 5

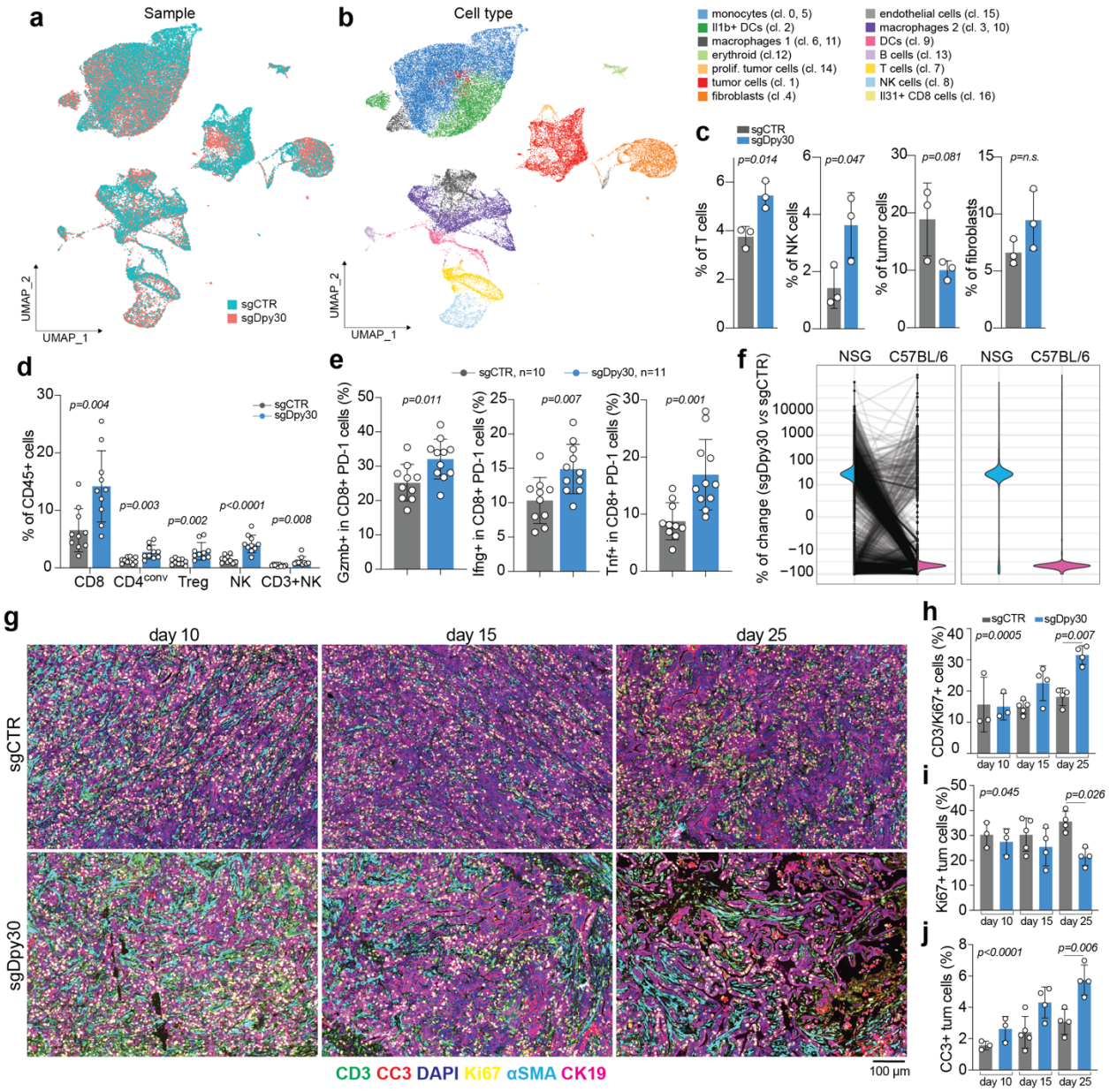

Figure 5. *Dpy30*-KO tumors display higher T cell infiltration, activation, and heterogeneity.

a-b. UMAP plot shows bi-dimensional sample (a) and cell type (b) distribution of control (sgCTR) or *Dpy30*-KO (sgDpy30) KPC tumors after filtering and quality control calculated using Seurat. **c.** Cell fraction of T cells, NK cells, tumor cells and fibroblasts calculated using Seurat in sgCTR and sgDpy30 KPC tumors. **d.** Percentage of CD8+ T cells, CD4+ conventional T cells, CD4+/Foxp3+ T regulatory cells, CD3+ NK, and NK

1706 cells in sgCTR or sgDpy30 KPC tumors grown in immune-competent C57BL/6 mice. Data
1707 were analyzed using flow cytometry. **e.** Percentage of CD8+/PD-1+ T cells in sgCTR or
1708 sgDpy30 KPC tumors grown in C57BL/6 mice and expressing the cytotoxic markers
1709 *Gzmb, Ifng, Tnf* as analyzed by flow cytometry. **f.** Violin plots showing the percentage of
1710 barcode changes in sgCTR and sgDpy30 KPC injected in NSG (blue) or C57/BL6 (pink)
1711 background. **g.** Multiplexed immunofluorescence staining of CD3 (green), cleaved
1712 caspase 3 (CC3, red), Ki67 (yellow), αSMA (cyan), cytokeratin 19 (CK19, magenta) and
1713 DAPI (blue) in sgCTR or sgDpy30 KPC cells grown in C57BL/6 mice and collected after
1714 10, 15 or 25 days after cell injection. **h-j.** Bar plot showing the percentage of CD3/Ki67+
1715 cells (h), CC3+ cells (i) or Ki67+ cells (j) in the samples described in g. In (c-e, h-j) each
1716 dot represents a biological replicate and data are presented as mean ± SD and statistical
1717 significance was calculated using Student's *t* test (c-e) or one-way ANOVA (h-j).

Figure 6

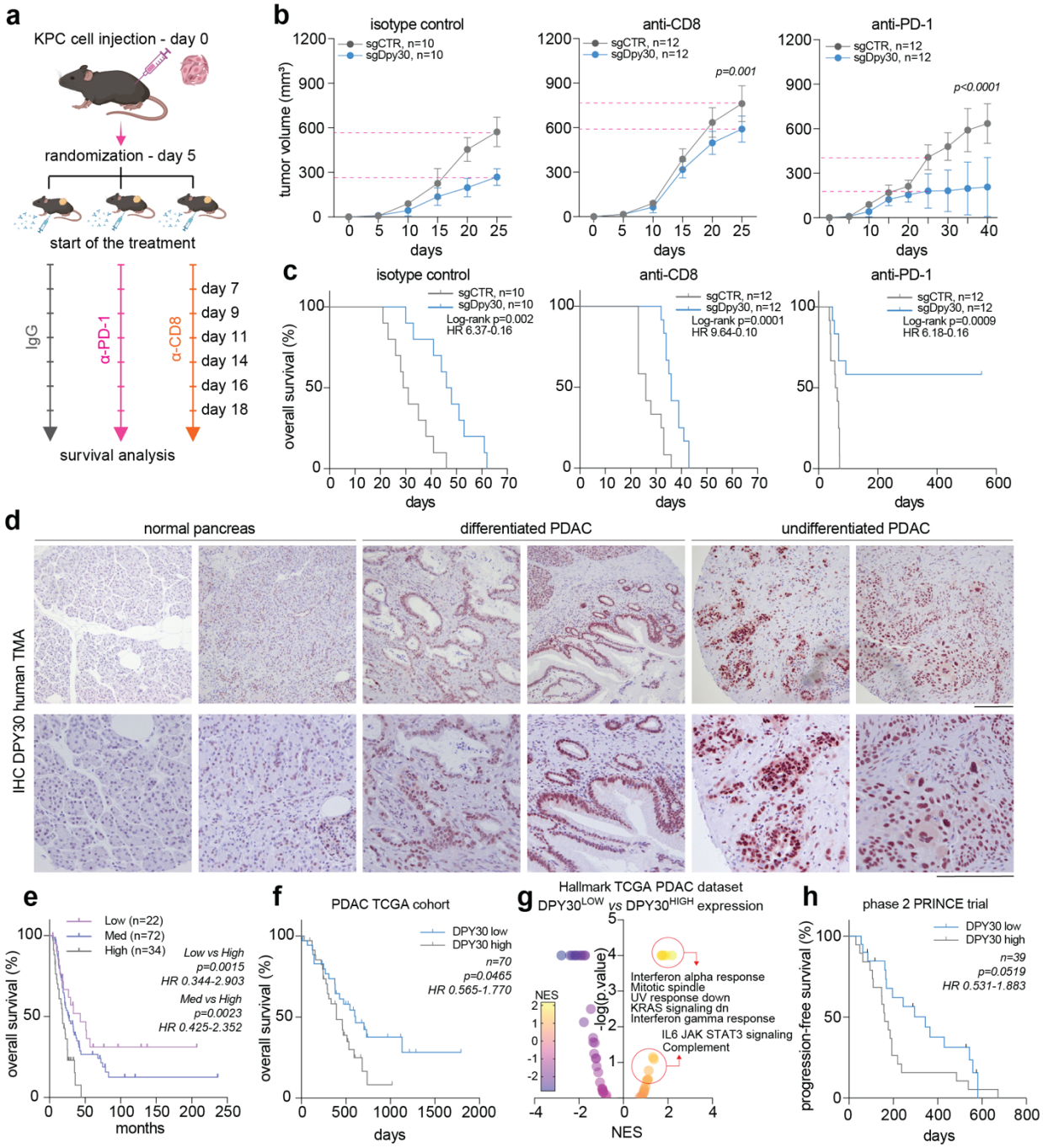

Figure 6. DPY30 expression correlates with tumor stage, poor outcome, and resistance to ICB.

a. Schematic representation of the in vivo experiment: control (sgCTR) or *Dpy30*-KO (sgDpy30) KPC cells were injected subcutaneously into C57BL/6 mice. After 5 days mice were randomized and treated starting from day 7 with monoclonal antibodies against

1724 CD8 (α-CD8) or PD-1 (α-PD-1) or isotype control three times per week, for two weeks.
1725 **b-c.** Graphs reporting the tumor volumes (b) or Kaplan-Meier survival curves (c) of sgCTR
1726 or sgDpy30 KPC tumors as described in a. **d.** DPY30 immunohistochemical (IHC) staining
1727 in normal pancreas and PDAC samples included in the tissue microarray (TMA). **e.**
1728 Kaplan–Meier survival curve of patients with PDAC included in the TMA described in (d)
1729 and divided according to low (IHC score 0 or 1), medium (IHC score 2), or high (IHC score
1730 3) DPY30 expression. **f.** Kaplan–Meier survival curve of patients in the TCGA PDAC
1731 cohort and divided according to low or high *DPY30* expression. **g.** Volcano plot
1732 representing GSEA in high-purity TCGA PDAC samples and divided according to high--
1733 or low *DPY30* expression. **h.** Kaplan–Meier progression-free survival curve of patients
1734 included in the phase 2 PRINCE PDAC trial and divided according to low or high *DPY30*
1735 expression. In (c, e, f, h) statistical significance and Hazard Ratio (HR) were calculated
1736 using the Log-rank test. In (b) data are presented as mean ± SD and statistical
1737 significance was calculated using one-way ANOVA.

Extended Data Figure 1

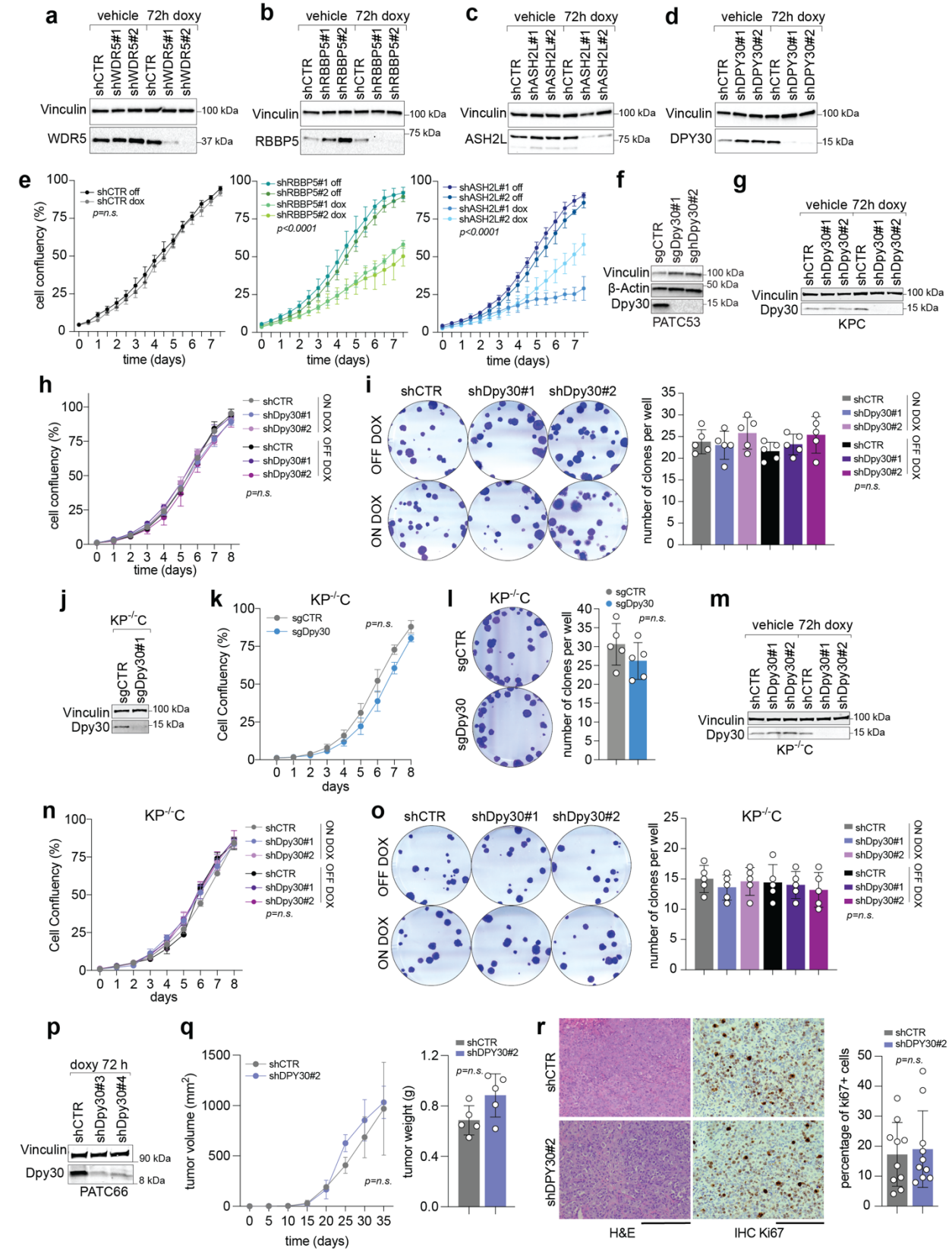

1738

1739 **Extended Data Figure 1. DPY30 is dispensable for cell proliferation.**

1740 **a-d.** Western Blot analysis of PATC53 cells harboring shRNAs against WDR5,
1741 RBBP5, ASH2L, DPY30 or control (respectively shWDR5, shRBBP5, shASH2L,
1742 shDPY30 or shCTR). **e.** Growth curve analysis of PATC53 cells described in a-d. **f.**
1743 Western Blot analysis of control (sgCTR) or DPY30-KO PATC53 cells. **g.** Western Blot
1744 analysis of KPC cells silenced for Dpy30 (shDPY30) or control (shCTR). **h.** Growth curve
1745 of KPC cells described in g. **i.** Representation (left) and quantification of a clonogenic
1746 assay of KPC cells, as described in g. **j.** Western Blot analysis of sgCTR or sgDpy30 KP^{-}
1747 $^{/-}$C cells. **k.** Growth curve of KPC cells described in j. **l.** Representation (left) and
1748 quantification of a clonogenic assay of $KP^{-/-}$C cells, as described in j. **m.** Western Blot
1749 analysis of shCTR or shDpy30 $KP^{-/-}$C cells. **n.** Growth curve of $KP^{-/-}$C cells described in
1750 m. **o.** Representation (left) and quantification (right) of a clonogenic assay of $KP^{-/-}$C cells,
1751 as described in m. **p.** Western Blot analysis of shCTR or shDPY30 PATC66 cells. **q.**
1752 Volume (left) and weight (right) of tumors from shCTR or shDPY30 PATC66 cells injected
1753 subcutaneously into the flank of NSG mice. **r.** Histopathological analysis of tumors
1754 described in (q). Hematoxylin and eosin (H&E) staining (left), Ki67 IHC staining (middle)
1755 and Ki67 quantification (right) are shown. In (a-e, g-l, m-r) cells were treated or not with
1756 doxycycline to induce shRNA expression. In western blot analyses vinculin or actin were
1757 used as loading controls. In e, h,i, k, l, n, o, q, r data are expressed as mean ±SD. Each
1758 dot represents a biological replicate. Statistical significance was calculated using one-
1759 way ANOVA followed by Tukey's multiple comparison tests (e, h, i, n, o) or using Student's
1760 t test (k, l, q, r).

Extended Data Figure 2

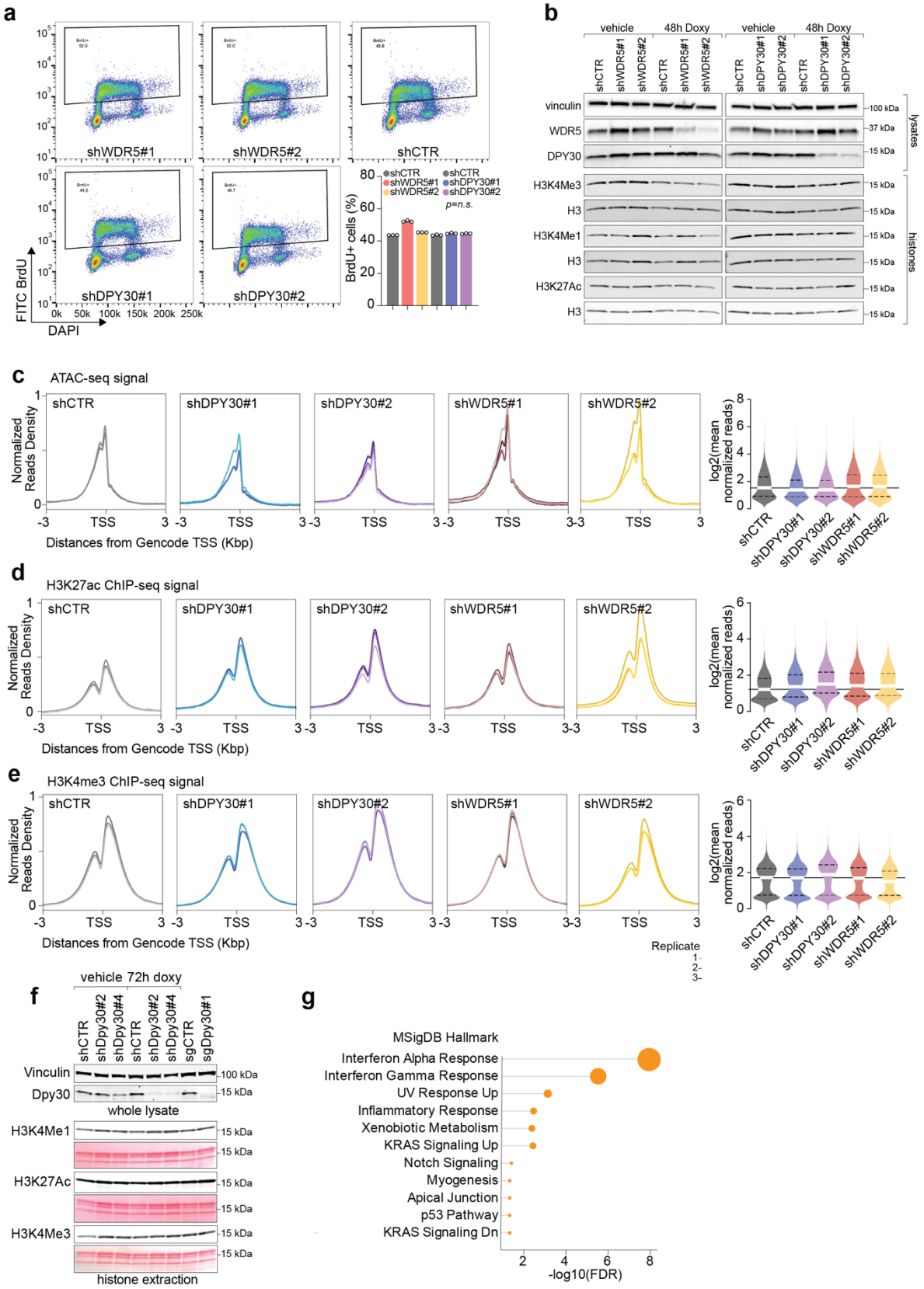

1762 **Extended Data Figure 2. WDR5 loss, but not DPY30, broadly affect H3K4**
1763 **methylation patterns.**
1764 **a.** Dot plots of BrdU incorporation assay of PATC53 cells silenced for WDR5 or
1765 DPY30 (respectively shWDR5 and shDPY30) or control (shCTR). Cells were treated with
1766 doxycycline for 48 hrs to induce shRNA expression. Data are expressed as mean ±SD,
1767 each dot represents a biological replicate. Statistical significance was calculated using
1768 one-way ANOVA. **b.** Western Blot analysis of whole lysate (upper panel) or histone
1769 lysates (lower panel) in PATC53 cells, as described in a. **c.** Plots showing normalized
1770 reads intensity (left) and the quantification (right) of ATACseq signals from three biological
1771 replicates of PATC53 cells as described in a-b. **d.** Plots showing normalized reads
1772 intensity (left) and the quantification (right) of H3K27ac signals from three biological
1773 replicates of PATC53 cells in a-b. **e.** Plots showing normalized reads intensity (left) and
1774 the quantification (right) of H3K4me3 signals from three biological replicates of PATC53
1775 cells as described in a-b. **f.** Western Blot analysis of whole lysate (upper) or histone
1776 lysates (lower) in KPC cells silenced/knock out for Dpy30 (respectively shDpy30 and
1777 sgDpy30) or control (shCTR or sgCTR). Cells were treated with doxycycline or vehicle for
1778 72 hrs to induce shRNA expression. **g.** Plot representing the top regulated pathways
1779 resulting from genes having H3K4me3 peak loss in shWDR5 PATC53 cells compared to
1780 controls (shCTR). In c-d, data in the violin plots are presented as median value.

Extended Data Figure 3

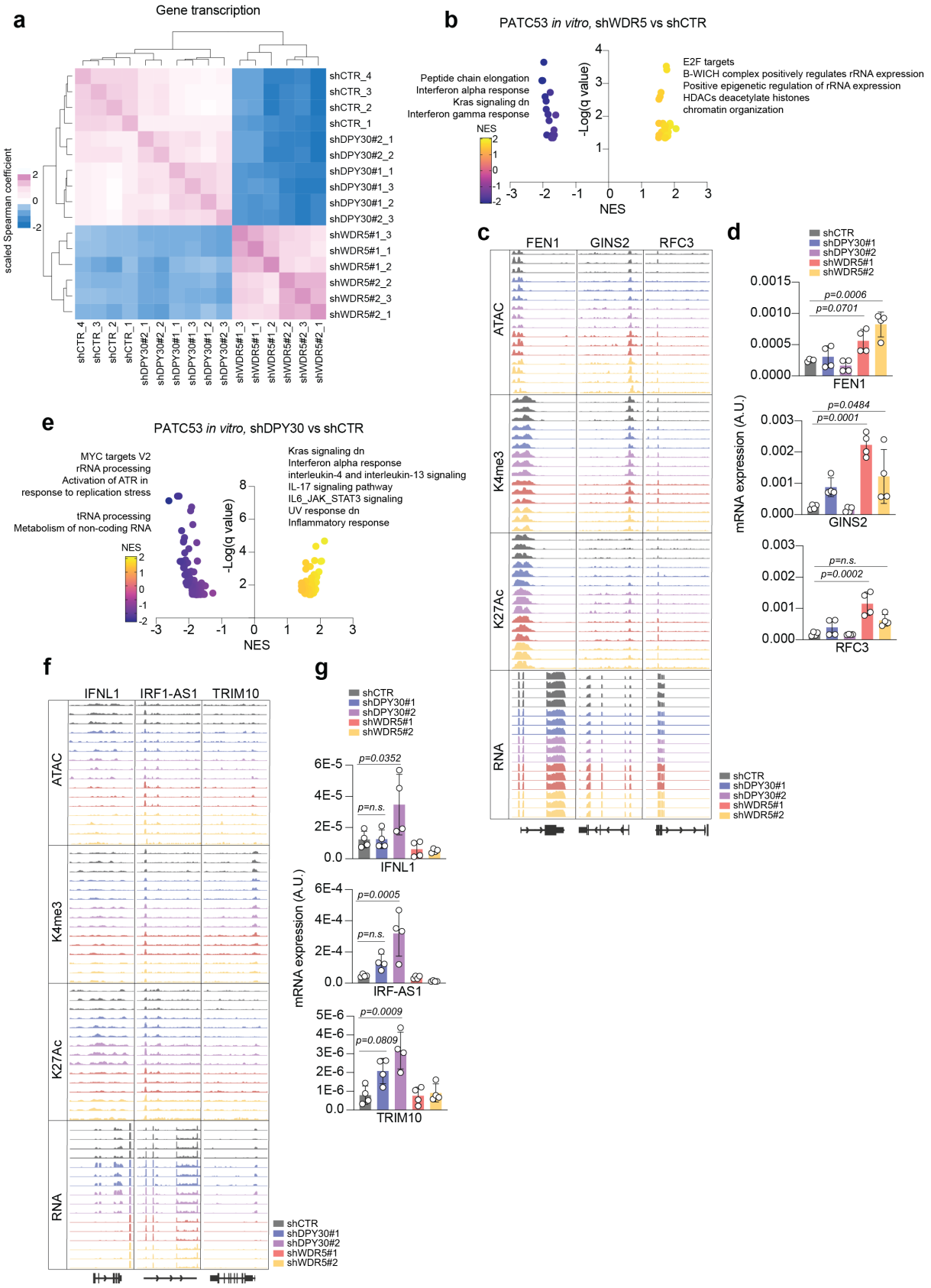

1782 **Extended Data Figure 3. DPY30 loss moderately upregulates inflammatory**
1783 **pathways.**
1784 **a.** Heatmap showing Spearman correlation between samples and biological
1785 replicates for bulk RNA sequencing (RNAseq) of PATC53 cells silenced for WDR5
1786 (shWDR5) or DPY30 (shDPY30) or control (shCTR). **b.** Volcano plot representing the
1787 GSEA results from bulk RNAseq data in PATC53 cells shWDR5 versus shCTR. **c.** Impact
1788 of shCTR, shDPY30 or shWDR5 in PATC53 cells on *FEN1*, *GINS* and *RFC3* analyzed
1789 by chromatin accessibility (ATAC), histone H3 methylation (H3K4me3), histone H3
1790 acetylation (H3K27ac) and mRNA expression (RNA). **d.** Graphs reporting the mRNA
1791 expression of *FEN1*, *GINS* and *RFC3* analyzed by quantitative PCR in shCTR, shDPY30
1792 and shWDR5 PATC53 cells. **e.** Volcano plot representing GSEA from bulk RNAseq data
1793 in PATC53 cells shDPY30 versus shCTR. **f.** Impact of shCTR, shDPY30 or shWDR5 in
1794 PATC53 cells on *IFNL1*, *IRF-AS1* and *TRIM10* analyzed by ATAC, H3K4me3, H3K27ac
1795 and RNA expression. **g.** Graphs reporting the mRNA expression of *IFNL1*, *IRF-AS1* and
1796 *TRIM10* analyzed as described in d. In b-c, top upregulated pathways are indicated. In d
1797 and g, data are expressed as mean ±SD, each dot represents a biological replicate, and
1798 statistical significance was calculated using one-way ANOVA.

Extended Data Figure 4

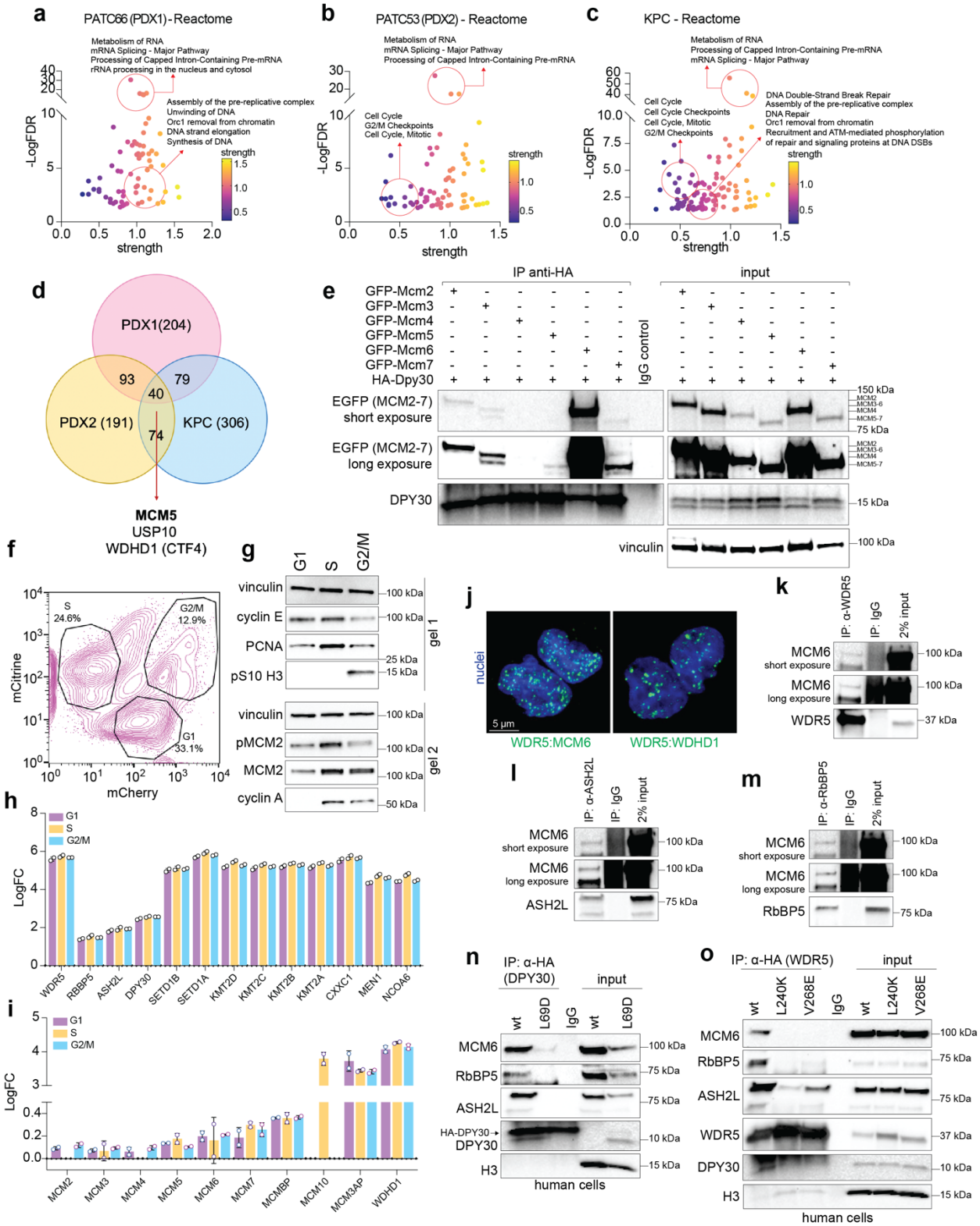

Extended Data Figure 4. The WRAD core interacts with the replisome machinery in a non-canonical manner.

1802 **a-c.** Dot plots reporting pathway enrichment analyses of DPY30 interactors in
1803 human PATC66 (a), PATC53 (b), or mouse KPC (c) cells. Pathway enrichment is
1804 calculated using STRING online tool and Reactome module. **d.** Venn diagram showing
1805 the DPY30 common interactors among PATC53 (PDX2), PATC66 (PDX1), and KPC
1806 cells. **e.** Western Blot analysis of 293T cells co-overexpressing HA-tagged mouse DPY30
1807 and EGFP-tagged mouse MCM members (MCM2-7). Control IgG and input were
1808 included. **f.** Contour plot showing the gating strategy for sorting PATC53 cells expressing
1809 FUCCI according to cell cycle phases. **g.** Western blot analysis of PATC53 cells sorted
1810 as in f. **h-i.** Bar plots showing the fold change enrichment of the epigenetic interactors (h)
1811 or replisome interactors (i) in DPY30 immunoprecipitates analyzed by mass spectrometry.
1812 Each dot represents a biological replicates and data are expressed as mean ± SD. **j.**
1813 Representative PLA staining detecting WDR5 interaction with WDHD1 and MCM6 in
1814 PATC66 cells. **k-m.** Western Blot analysis of the immunoprecipitation assay for
1815 endogenous WDR5 (k), Ash2L (l) and RbBP5 (m) in PATC53 cells. Control IgG and input
1816 were included. **n.** Western blot analysis of PATC53 cells expressing DPY30 wild type
1817 (WT) or mutant (L69D) isoforms. **o.** Western blot analysis of PATC53 cells expressing
1818 WDR5 wild type (WT) or mutant (L240K, V268E) isoforms. In (n, o), control IgG and input
1819 are shown, and H3 was used as a loading control.

Extended Data Figure 5

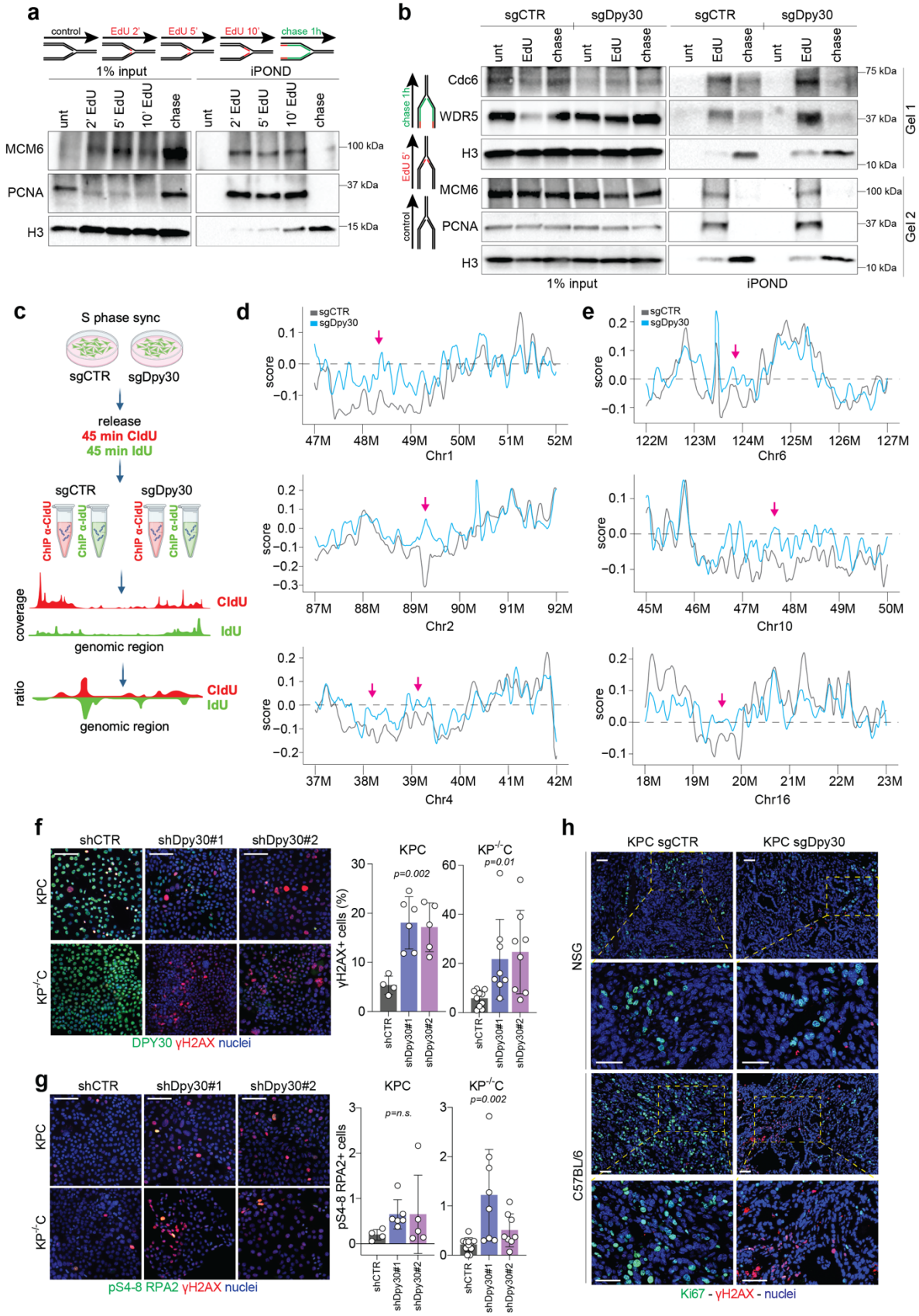

1820

1821 **Extended Data Figure 5. DPY30 loss leads to DNA replication stress and DNA**
1822 **damage.**
1823 **a.** Western blot analysis of proteins bound to nascent DNA retrieved using iPOND
1824 or input control in KPC cells. Cells were treated as follows: control (negative control, no
1825 biotin in the click reaction), EdU pulse (EdU treatment for 2, 5 or 10min), chase (EdU
1826 treatment for 10 min, followed by a 60 min thymidine chase). Histone H3 was used as a
1827 loading control. **b.** Western blot analysis of iPOND or input control in KPC cells, control
1828 (sgCTR) or *Dpy30*-KO (sgDpy30). Cells were treated as described in a. Histone H3 was
1829 used as a loading control. **c.** Schematic representation of the re-replication sequencing
1830 (re-repli-seq) in KPC sg/ctr or sgDpy30 cells. **d-e.** Plots showing the genomic regions and
1831 the ratio (score) of incorporated CldU and IdU in KPC sgCTR and sgDpy30 cells. **f.** Left,
1832 panels show immunofluorescence images of KPC and $KP^{-/-}C$ cells silenced for Dpy30
1833 (shDpy30) or control (shCTR), treated with doxycycline for 96 hrs to induce shRNA
1834 expression. In green DPY30, in red pS139 H2AX (γH2AX), in blue nuclei (DAPI). Right,
1835 graphs report the percentage of γH2AX+ in KPC cells. **g.** Left, panels show
1836 immunofluorescence staining of KPC and $KP^{-/-}C$ cells, as described in f, stained for pS4-
1837 8 RPA (green), γH2AX (red) and nuclei (blue). Right, graphs report the percentage of
1838 pS4-8 RPA+ in each cell group. **h.** Immunofluorescence staining of sgDpy30 or sgCTR
1839 KPC tumors grown in NSG (upper) or C57BL/6 (lower) mice and then stained for Ki67
1840 (green), γH2AX (red), and nuclei (blue). In (f-g), data are expressed as mean ± SD and
1841 each dot represents a different analyzed field. Statistical significance was calculated
1842 using one-way ANOVA (f, g).

Extended Data Figure 6

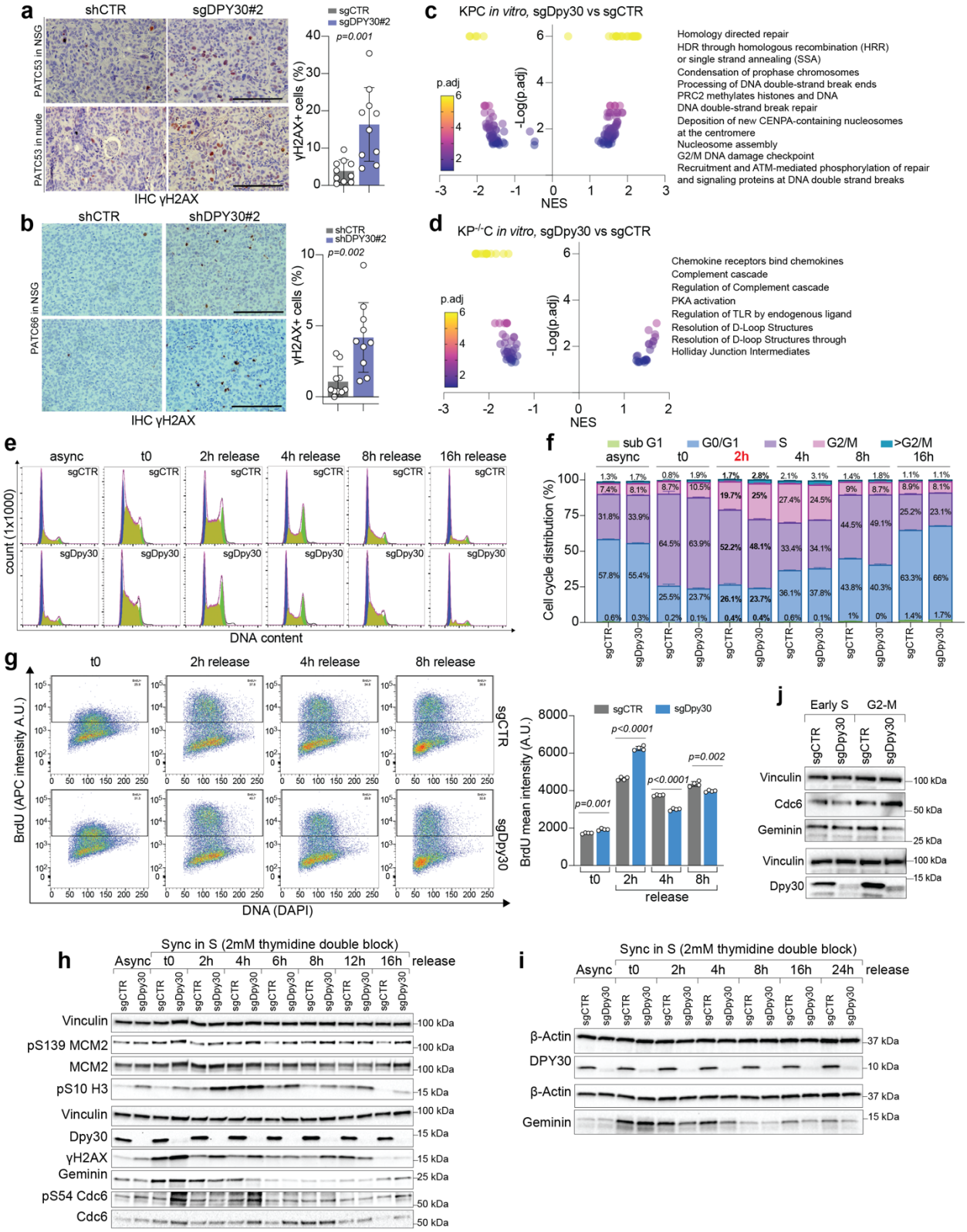

1843

1844 **Extended Data Figure 6. DPY30 loss leads to DNA damage and accelerated**
1845 **S-to-G2/M transition.**
1846 **a.** Immunohistochemical staining of γH2AX (left) and quantification (right) in control
1847 (sgCTR) or DPY30-KO (sgDPY30) PATC53 tumors grown in NSG (upper) or nude (lower)
1848 mice. **b.** Immunohistochemical staining of γH2AX (left) and quantification (right) in control
1849 (shCTR) or DPY30-silenced (shDPY30) PATC66 tumors grown in NSG mice. **c-d.**
1850 Volcano plots representing the GSEA results from bulk RNAseq data in KPC (c) or $KP^{-/-}$
1851 C (d) cells sgDpy30 versus sgCTR. **e.** Histograms showing DNA content in sgCTR or
1852 sgDpy30 KPC cells. Cells were collected in exponential growth (async) or synchronized
1853 (t0) in S phase using a double thymidine block and then released in complete medium for
1854 the indicated time. **f.** Bar graph showing cell cycle distribution in KPC cells as described
1855 in e. **g.** Dot plots (left) and quantification (right) of the BrdU incorporation assay in KPC
1856 cells described as in e. BrdU (APC) mean intensity is shown (A.U. = arbitrary unit). **h-i.**
1857 Western Blot analysis of sgCTR or sgDpy30 KPC (h) or $KP^{-/-}$C (i) cells, as described in e.
1858 Vinculin was used as loading control. **j.** Western Blot analysis of sgCTR or sgDpy30 KPC
1859 cells synchronized in S or G2/M phase. Vinculin was used as loading control. In (a, b, f,
1860 g), data are expressed as mean ±SD, each dot represents a biological replicate.
1861 Statistical significance was calculated using one-way student t test (a-b, g) or two-way
1862 ANOVA test (f).

Extended Data Figure 7

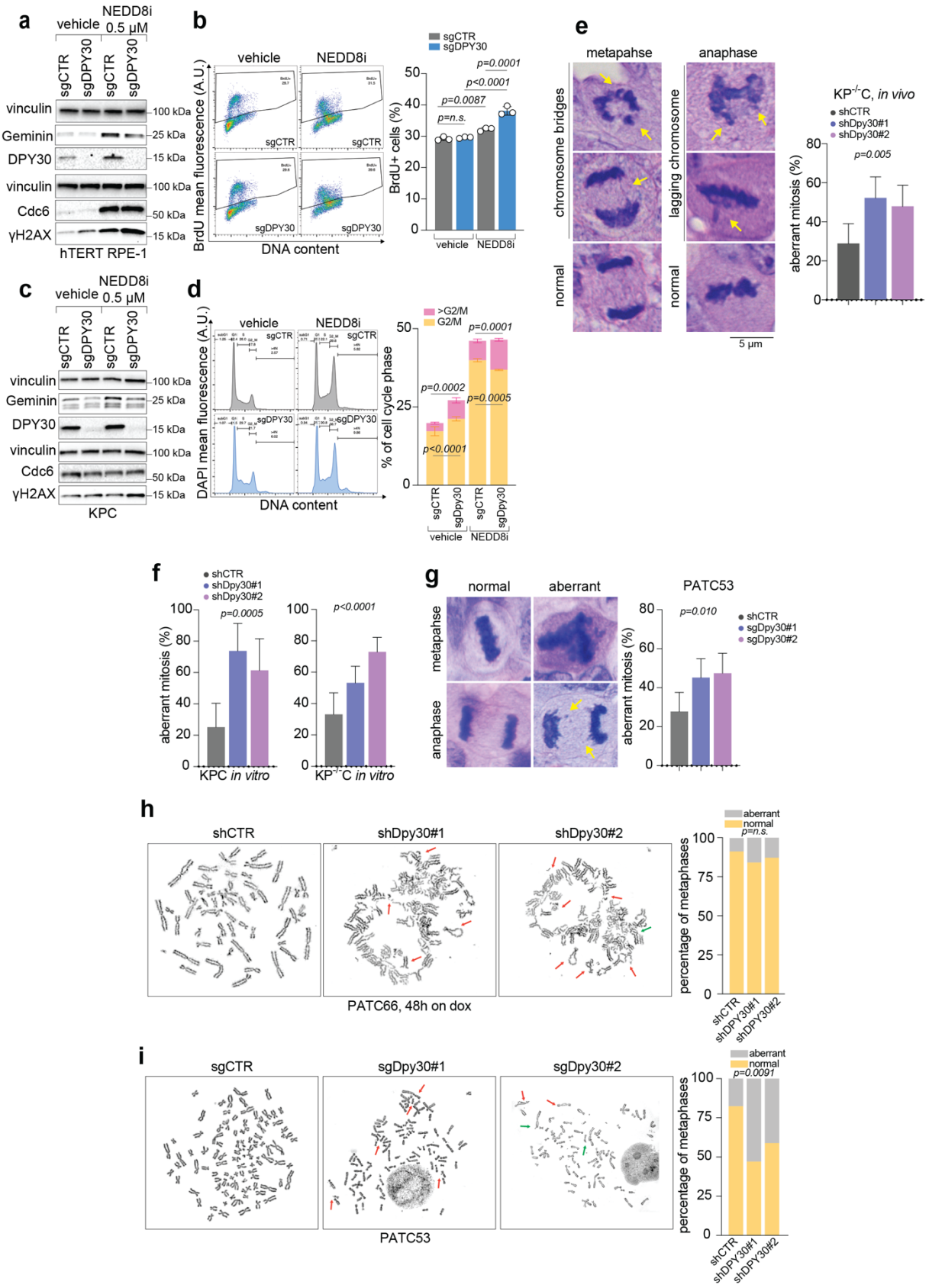

1863

1864 **Extended Data Figure 7. DPY30 loss increases chromosomal instability in**
1865 **PDAC.**
1866 **a.** Western Blot analysis of control (sgCTR) or *DPY30*-KO (sgDPY30) RPE-1 cells
1867 treated with vehicle or MLN4924 for 24 hrs. **b.** Dot plots (left) and cell percentage (right)
1868 of BrdU incorporation in RPE-1 cells as described in a. **c.** Western Blot analysis of sgCTR
1869 and sgDpy30 KPC cells treated with vehicle or MLN4924 for 24 hrs. **d.** Histograms of
1870 DNA content (left) and quantification of G2/M and aneuploid (>4N) cells (right) in KPC
1871 cells, as described in c. **e. f.** Bar graphs reporting the mean percentage of aberrant mitosis
1872 in control (shCTR) or Dpy30-silenced (shDpy30) KPC and $KP^{-/-}C$ cells *in vitro*. Cells were
1873 treated with doxycycline (dox) for 96 hrs to induce shRNA expression. **g.** Left, hematoxylin
1874 and eosin (H&E) staining of mitotic sgCTR and sgDPY30 PATC53 cells grown in NSG
1875 mice. Yellow arrows indicate chromosomal laggings. Right, bar graph reporting the
1876 percentage of aberrant mitosis in PATC53 cells. **h.** Left, images of metaphasic spread in
1877 shCTR or shDPY30 PATC66 cells treated with dox for 48 hrs to induce shRNA
1878 expression. **i.** Left, images of metaphasic spread in sgCTR and sgDPY30 PATC53 cells.
1879 Right, graph reporting the percentage of normal (yellow) or aberrant (grey) mitosis. In (a,
1880 c), vinculin was used as loading control. In (h-i), red arrows indicate chromosome fusions
1881 or breaks. In (b, d-g), data are expressed as mean ±SD, dots indicate biological replicates
1882 and statistical significance was calculated using one-way ANOVA (b, e, f, g), two-way
1883 ANOVA (d) or Chi-square test (h, i).

Extended Data Figure 8

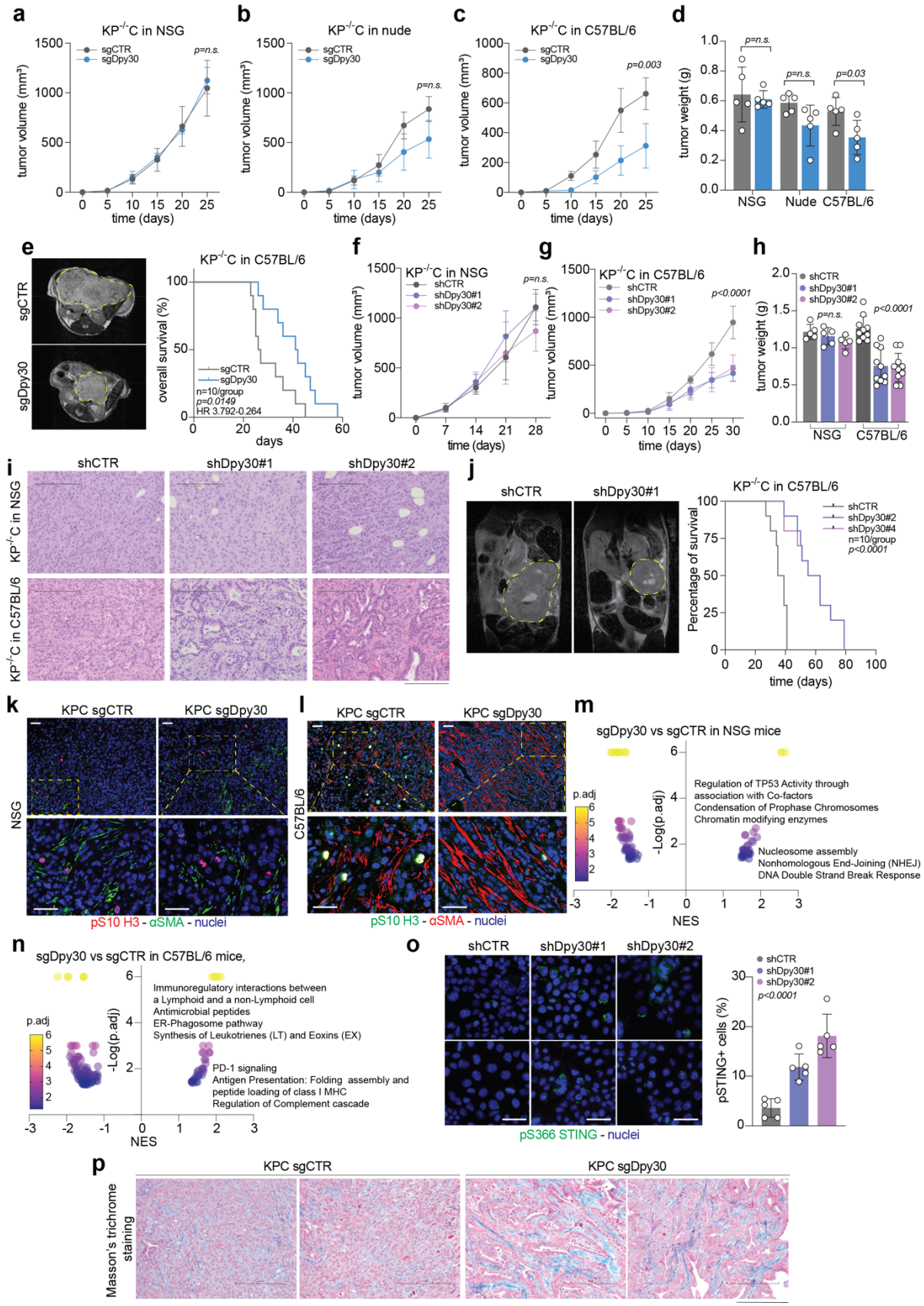

1884

1885 **Extended Data Figure 8. In pancreatic ductal carcinoma, DPY30 loss has a**
1886 **context-dependent phenotype.**
1887 **a-c.** Tumor volume of control (sgCTR) and Dpy30-KO (sgDpy30) $KP^{-/-}C$ cells
1888 injected subcutaneously into the flank of NSG (a), nude (b), or C57BL/6 (c) mice. **d.**
1889 Weight (mg) of tumors described in a-c. **e.** Left, T2 Magnetic Resonance Imaging (MRI)
1890 scans of sgCTR and sgDpy30 $KP^{-/-}C$ tumors grown orthotopically in the pancreas of
1891 C57BL/6 mice. Right, Kaplan-Meier survival curve of tumor-bearing mice. **f-h.** Tumor
1892 volume (f, g) and weight (h) of control (shCTR) or Dpy30-silenced (shDpy30) $KP^{-/-}C$ cells
1893 injected subcutaneously into the flank of NSG (f) and C57BL/6 (g) mice. **i.** Hematoxylin
1894 and eosin (H&E) staining of $KP^{-/-}C$ tumors as described in f-h. **j.** Left, T2 Magnetic
1895 Resonance Imaging (MRI) scans of shCTR or shDpy30 $KP^{-/-}C$ tumors grown
1896 orthotopically in the pancreas of C57BL/6 mice. Right, Kaplan-Meier survival curve of
1897 tumor-bearing mice. **k-l.** Immunofluorescence staining of shCTR and shDpy30 KPC
1898 tumors grown in NSG (k) or C57BL/6 (l) mice and then stained for αSMA, pS10-H3, and
1899 nuclei. **m-n.** Volcano plots representing GSEA analyses from bulk RNAseq data in
1900 sgDpy30 versus sgCTR $KP^{-/-}C$ tumors grown in NSG (k) or C57BL/6 (l) mice. **o.**
1901 Immunofluorescence staining of pS366 STING (green) and nuclei (blue) in sgCTR and
1902 sgDpy30 KPC cells, in vitro. **p.** Masson's trichrome staining of sgCTR and sgDpy30 KPC
1903 tumors grown in C57BL/6 mice. In (a-d, f-h, o), data are expressed as mean value ±SD.
1904 Dots represent biological replicates. In (e, j), statistical significance and Hazard Ratio
1905 (HR) were calculated using Log-rank test. Statistical significance was calculated using
1906 Student t test (a-d) or one-way ANOVA (f-h, o). Scale bar = 200 μm (i, p), 100 μm (k, l),
1907 50 μm (o).

Extended Data Figure 9

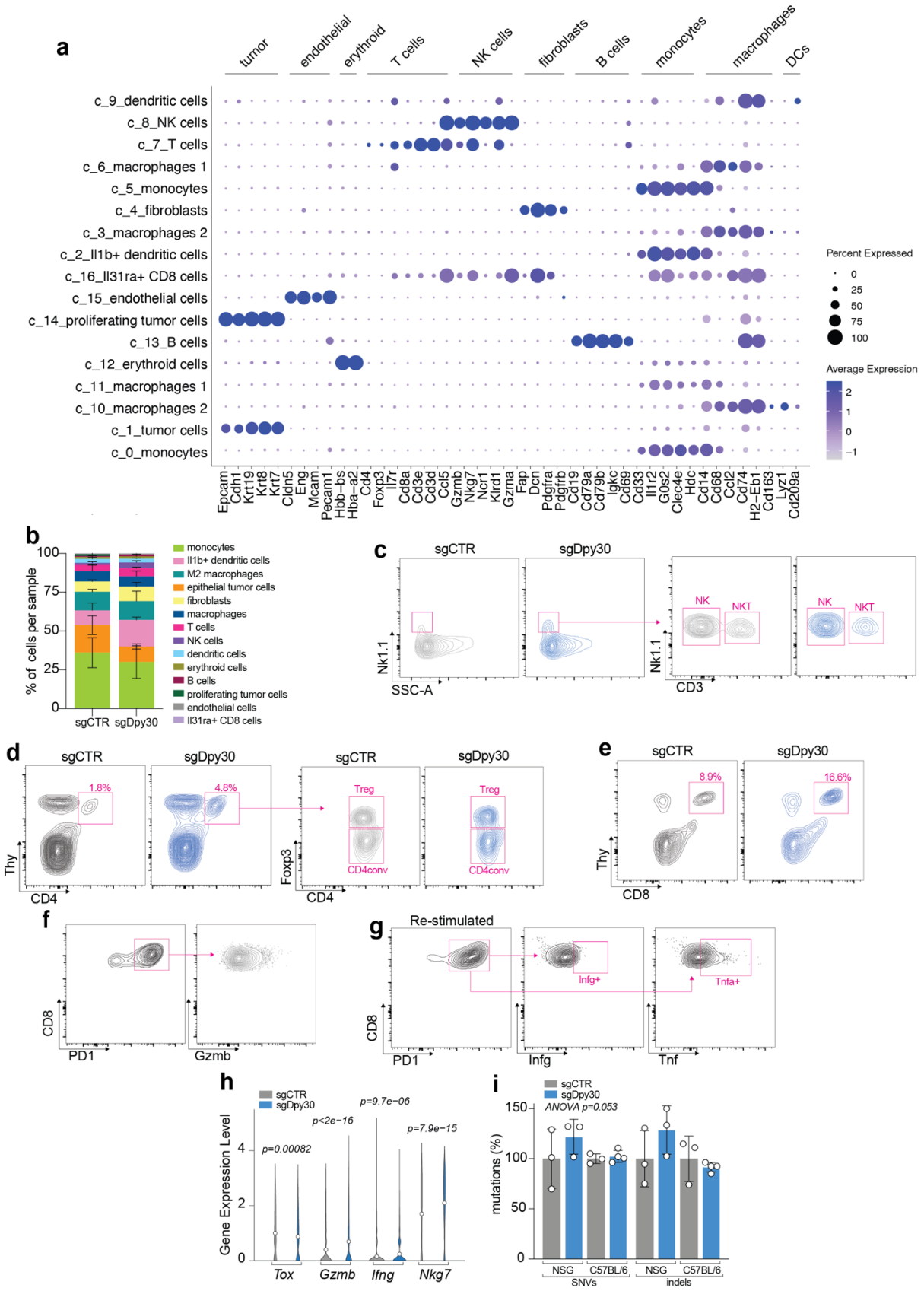

1908

1909 **Extended Data Figure 9. Dpy30 knockout tumors display higher T cell**
1910 **infiltration and activation.**

1911 **a.** Bubble plot showing expression levels of genes selected for cluster annotation
1912 in single-cell RNA sequencing data from control (sgCTR) or Dpy30-KO (sgDpy30) KPC
1913 tumors grown in C57BL/6 mice. Size of dots represents the percentage of cells
1914 expressing the gene; color scale shows the average expression level. **b.** Bar plot showing
1915 the percentage of cell distribution in the different clusters (cell type) calculated using
1916 Seurat in sgCTR or sgDpy30 KPC tumors (n=3 per condition). **c-g.** Contour plots showing
1917 the flow cytometry gating strategy for detecting the NK or CD3+ NK cells (c), CD4+
1918 conventional or Treg cells (d), CD8+ T cells (e), CD8/PD-1+ cells expressing Granzyme
1919 B (Gzmb, f), Interferon gamma (Infg, g) or Tumor Necrosis Factor (tnf, g). **h.** Violin plot
1920 showing the expression of T cell exhaustion marker (Tox) or cytotoxic markers *(Gzmb,*
1921 *Ifng, Nkg7)* in the T cell of sgCTR or sgDpy30 KPC tumors, calculated using Seurat. **i.**
1922 Bar plot showing the percentage of single nucleotide variants (SNVs) and indels in sgCTR
1923 or sgDpy30 KP-/-C tumors grown in NSG or C57BL/6 mice (n=3 or 4 tumors per group).
1924 Data are expressed as median (h) or mean value ±S.D. (i). Statistical significance was
1925 calculated using Student's t test (h) or a two-way ANOVA (i).

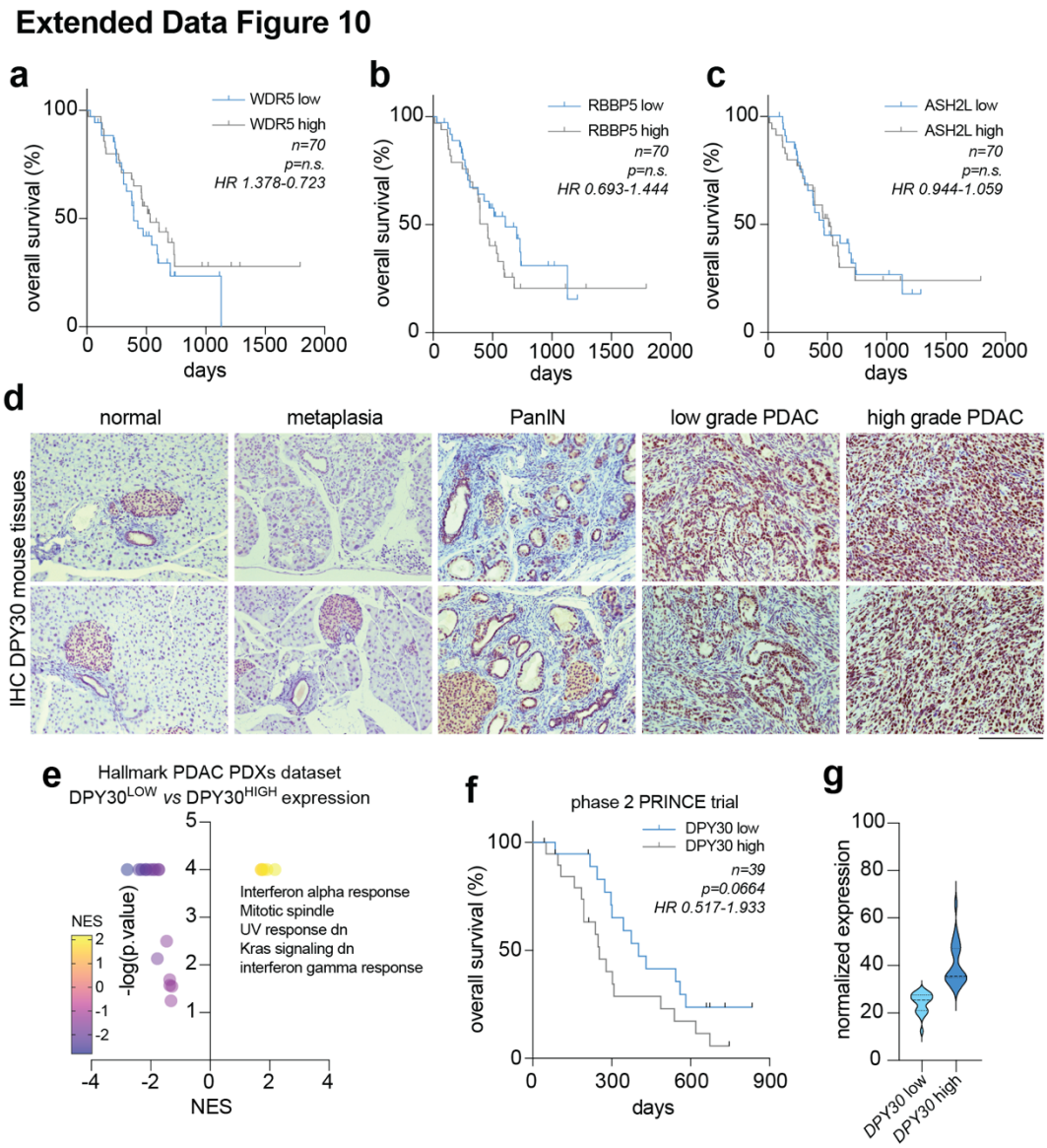

Extended Data Figure 10. DPY30 correlates with tumor stage and predicts response to ICB treatment.

a-c. Kaplan–Meier survival curves of TCGA PDAC patients divided according to low- or high-expression of *WDR5* (a), *RBBP5* (b) and *ASH2L* (c). **d.** DPY30 immunohistochemical staining in normal pancreas, pancreatic metaplasia and intraepithelial neoplasia (PanIN) and PDAC samples from KPC mouse model. **e.** Volcano plot representing GSEA in high-purity PDAC PDXs samples and represented as low versus high *DPY30* expression. **f.** Kaplan–Meier overall survival curve of patients in the PRINCE trial cohort divided according to low- or high-expression of *DPY30.* **h.** Violin plot showing the median expression of *DPY30* in the patience included in the analysis in f and

1937 Fig. 6h. In (a-c, f), statistical significance and Hazard Ratio (HR) were calculated using
1938 the Log-rank test.